1-11-2017

# Investigation on the Structural Variation of Self-Assembled Lipid Bicellar Mixtures Upon Environmental Stimuli and Addition of PEGylated Compounds

Ying Liu
*University of Connecticut*, yingliu8619@gmail.com

# Investigation on the Structural Variation of Self-Assembled Lipid Bicellar Mixtures Upon Environmental Stimuli and Addition of PEGylated Compounds

**Ying Liu, Ph.D.**

**University of Connecticut, 2017**

Bilayered mixed micelle, known as "bicelle", has been extensively used as the biological membrane models in deciphering membrane-associated proteins. The bicellar mixtures normally constitute of long-chain and short-chain phospholipids in aqueous solutions. Disc-like morphology has been assumed for such mixtures where a bilayer fragment of long-chain phospholipids is sequestered by short-chain lipids at the rim. Recently, other structures such as vesicles, elongated micelles, and lamellae have also been found in bicelles as temperature, concentration, and salinity vary.

The nano-sized bicellar discs (nanodiscs) and vesicles have great potential to be used as ingredient carriers for imaging and therapy. The research motivation is stimulated from enabling the nanodiscs and vesicles for future *in vivo* application. The objective of my research is to understand the interactions in the bicellar systems under effects of the doping negatively charged lipids, PEGylated lipids with different PEG molecular weights and molar ratios, and other types amphiphilic compounds on the morphological variation under different conditions.

The first problem is that the stability of the size and shape of bicelles is hard to be achieved by the zwitterionic components. I significantly improved the stability of bicellar assemblies by doping the negatively charged long-chain lipids, in which way the interparticle electrostatic repulsions play an important role. Furthermore, Polyethylene glycol (PEG) surface-coated nanoparticles have been confirmed to be an effective approach to prolong their *in vivo* circulation time. I further investigated the interaction between bicelles with a reverse Pluronic triblock copolymer which constitutes of two hydrophobic ends (polypropylene glycol, PPG) and a PEG hydrophilic middle block (PPG-PEG-PPG). The triblock copolymer is capable of linking bicellar nanodiscs and facilitating the formation of various structures such as vesicles and stacking. The structural characterizations were mainly investigated via small angle neutron/X-ray scattering, dynamic light scattering, and transmission electron microscopy. The assembled structures were rationalized by scattering models such as flat cylinders, core-shell spheres, ellipsoids, and lamellae.

My research outcomes allow interested researchers to further understand and utilize the bicelle templates for biomimetic and advanced material applications.

**Investigation on the Structural Variation of Self-Assembled Lipid Bicellar Mixtures Upon Environmental Stimuli and Addition of PEGylated Compounds**

Ying Liu

B.E. Shenyang University of Chemical Technology, 2008

A Dissertation

Submitted in Partial Fulfillment of the

Requirements for the Degree of

Doctor of Philosophy

At the

University of Connecticut

2017

APPROVAL PAGE

Doctor of Philosophy Dissertation

# Investigation on the Structural Variation of Self-Assembled Lipid Bicellar Mixtures Upon Environmental Stimuli and Addition of PEGylated Compounds

Presented by

Ying Liu

Major Advisor _____

Mu-Ping Nieh

Associate Advisor _____

Diane Burgess

Associate Advisor _____

Hadi Bozorgmanesh

Associate Advisor _____

Montgomery Shaw

Associate Advisor _____

Tai-Hsi Fan

University of Connecticut
2017

# *Dedication*

*I dedicate this thesis*
*to my parents, Mr. Hankui Liu and Mrs. Jinghua Ju*
*and to the memory of my grandparents Mr. Chun Liu and Mrs. Guizhi Li*
*for always being proud of me*
*and loving me unconditionally*

*to Dr. Hadi Bozorgmanesh*
*for being the most important mentor in my life*

2017

# Acknowledgements

First of all, I would like to thank my major advisor Dr. Mu-Ping Nieh for his guidance and support for my research. He gave me the chance to join his group to pursue my Ph.D. and the opportunities to present my research at academic conferences. He also encouraged and helped me at the moment I faced obstacles in my study. I cannot imagine I have conquered that much difficulties without his help. I wish to express my deepest sincere gratitude to my associate advisor, Dr. Hadi Bozorgmanesh. His untiring efforts in guidance and unconditioned encouragements have been crucial to me and helped me through the most difficult time. His dedication to professionalism, leadership, and creativity has helped me in improving the critical thinking methods, writing skills, presentation skills, as well as projects management and entrepreneurship. His invaluable support has also helped me step out of the comfort zone and bravely pursue my own dream. I am deeply indebted to my associate advisors Dr. Diane Burgess, Dr. Montgomery Shaw, Dr. Tai-His Fan for their advice and support.

I would like to thank School of Engineering Administration, Dean Kazem Kazerounian, Associate Dean Wei Mei, Associate Dean Michael Accorsi, Kathy Rocha, Noreen Wall for their great effort on establishing the programs for engineering students. I am also grateful to the help from Chemical Engineering Department, Dr. Douglas Cooper, Leah Winterberger, Susan Soucy. I would also like to thank the scientific and technical staff in Institute of Material Science, Gary Lavigne, Dr. Roger Ristau and Dr. Lichun Zhang, Rick George, Michael Chebro.

I would like to thank my collaborators, Mr. Ming Li and Dr. Yongkun Yang in the University of Connecticut, Dr. Boualem Hammouda in National Institute of Standards and Technology, Dr.

John Katsaras in the Oak Ridge National Laboratory, Dr. Anu Puri in the National Cancer Institute.

I would like to acknowledge the financial support received from National Science Foundation. I thank the University of Connecticut for supporting my graduate studies with assistantships and tuition waivers.

I am deeply grateful to the advice and love from my family members, Mrs. Xiufeng Xu, Mr. Jingtang Ju, Dr. Jingyue Ju, Dr. Jingfang Ju, Dr. Lei Ju, Dr. Wei Liu, Mrs. Jing Yu, Mrs. Yan Li, Dr. Yao Zhang, especially during my student life in the United States. The work is also in the memory of my passed grandparents Mr. Chun Liu, Mrs. Guizhi Li, Mr. Guangsen Ju.

Above all, I am deeply indebted to my parents, Mr. Hankui Liu and Mrs. Jinghua Ju for their unconditional love, blessing and support.

## TABLE OF CONTENTS

# Chapter 1 Introduction and Objectives

## 1.1 Background

Self-assembly is a ubiquitous phenomenon in nature and closely related to our life.[1] The cell plasma membrane is constituted by the self-assembled lipid bilayer with specific membrane proteins.[2] The most common membrane lipids are the glycerophospholipids, which is usually composed of a hydrophilic head group and two hydrophobic fatty acid chains. (Figure 1.1)

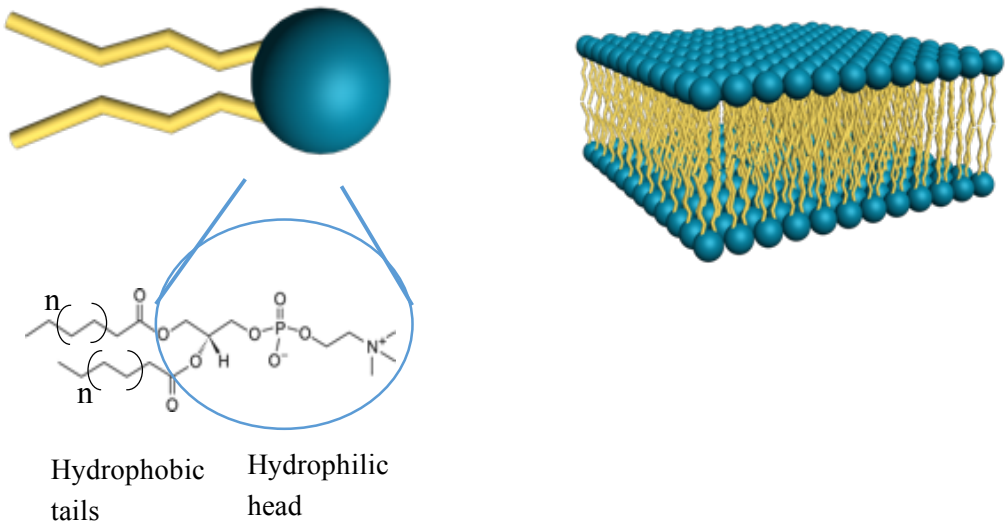


**Figure 1.1** Molecular structure and its cartoon of phospholipid molecular and the phospholipids bilayer structures when being dispersed in water

The lipid membrane supports the membrane proteins to enable the activities, such as cell metabolism and signaling. The investigation of membrane proteins' structure and functionality is still one of the greatest scientific challenges due to their structural complexity especially the hydrophobic domain. Several substrates have been designed to provide the native membrane protein environment and be analyzable in resonance spectroscopy (NMR), such as micelles[3], unilamellar vesicles[4] and mechanically oriented bilayers between glass plates[5].

"Bicelle" originated from bilayered micelles has emerged as a potent membrane protein substrate for its remarkable features of the bilayer environment and the self-alignment in the magnetic field.[6-9] Bicelle is composed of at least two different types of amphiphiles – the long-chain lipids (12-18 carbon atoms in each acyl chain) and detergents/short-chain lipids (6-8 carbon atoms in each acyl chain). The most common bicellar mixture is made of the long-chain dimyristoyl and the short-chain dihexanoyl phosphatidylcholine (di-$C_{14}$ DMPC and di-$C_6$ DHPC).[10, 11] It's worthy to be noted that the DMPC/DHPC magnetically alignable phase can only appear at the temperature above 23 ºC the phase transition temperature ($T_m$) of the long-chain DMPC. Therefore, the substrate formed by longer chain lipids with a higher $T_m$ may denature the embedded membrane protein when put in the alignable phase. For example, the dipalmitoyl phosphatidylcholine (di-$C_{16}$ DPPC) has its $T_m$ at 41 ºC,[12] which is higher than the physiological temperature 37 ºC. The chemical structures of DMPC, DHPC, and DPPC present in Table 1.1.

Initially, the magnetically aligned structure was presumed as discoidal micelles.[13, 14] The discoidal structure has been rationalized as a bilayer region made of the long-chain lipids with the highly curved rim sequestered by the short-chain lipids or detergents.[15] [Figure 1.2 (a)] Later, a serial small angle neutron scattering (SANS) studies have identified the structures of the alignable bicellar phase to be perforated lamellae,[16] which resemble the "Swiss-cheese" hypothesis.[17] [Figure 1.2(b)] The additional criteria are the molar ratio of the long- to short-chain lipids above 2.5 ($Q$-*ratio* > 2.5) and the lipid concentration ($C_{lp}$) above 50 mg/mL.[18-25]

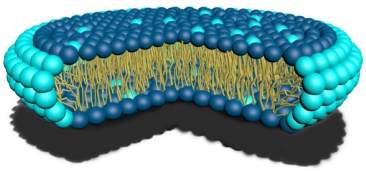

(a)

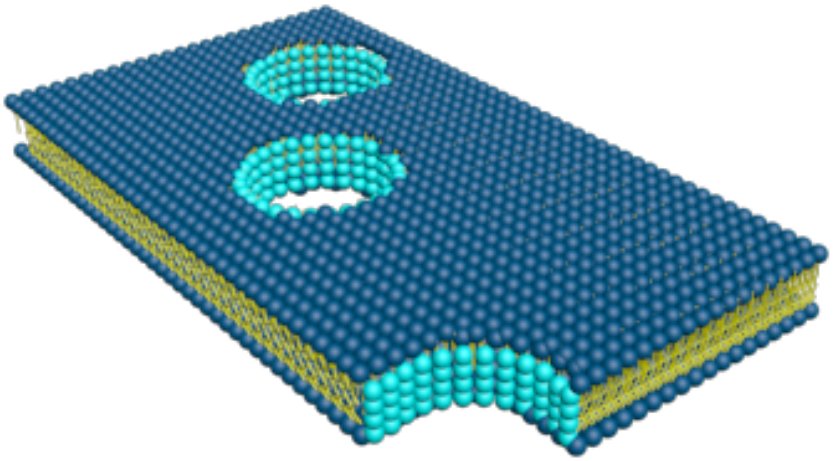

(b)

**Figure 1.2** (a) 3-D Cartoon of bicelle disc structure with corner coped. (b) Perforated lamellae. The headgroups of long-chain lipids are sketched as the dark-colored balls. The lighter-colored balls are representing the headgroups of short-chain lipids.

The broad view of the DMPC/DHPC bicelles with *Q-ratio* = 3.2 as a function of temperature and lipid concentration has been generalized in Figure 1.3 (a).[26] In the lower concentration range $C_{lp}$ < 10 mg/mL, "Onion-like" multilamellar vesicles (MLVs) coexisting with isotropic micelles have been found throughout the low- and high-temperature ranges.[27, 28] Due to the uncontrollable size of MLVs, the dilute bicelle system hadn't been studied as extensively as the concentrated ones.

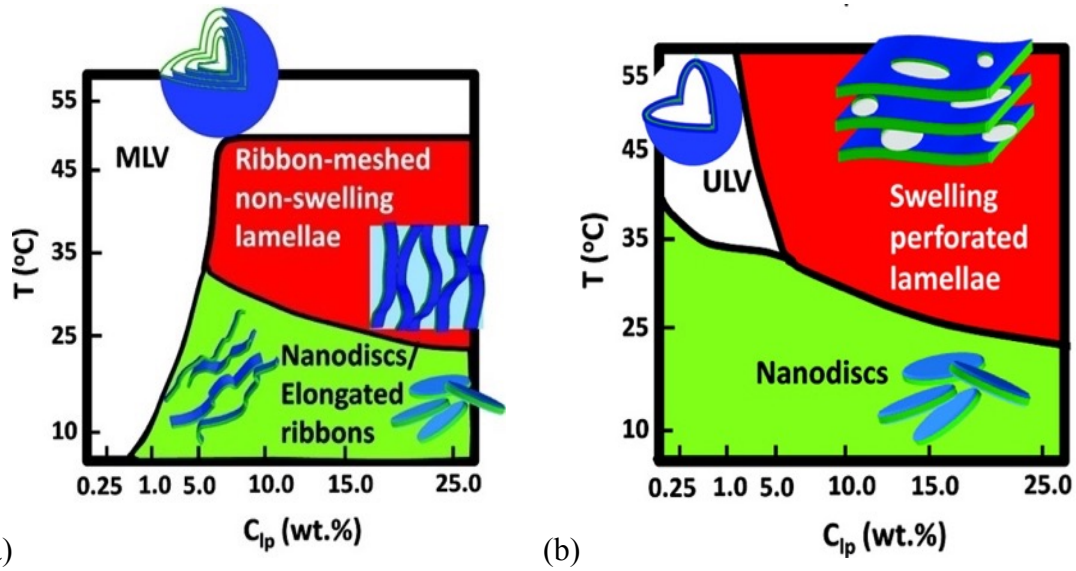


**Figure 1.3** Aggregate structures formed by (a) a zwitterionic phospholipid mixture ([DMPC]/[DHPC] = 3.2), and (b) a charged phospholipid mixture ([DMPC]/[DHPC] = 3.2 and [DMPG]/[DMPC] = 0.01) over a range of temperatures and total lipid concentrations.[26]

To prevent the formation of MLVs, the addition of charged lipids can enhance the stability of disc-shaped bicelles through the increased inter-particle Coulombic repulsion. For example, the growth of the DMPC/DHPC discs below the $T_m$ of DMPC was inhibited by doping a small amount of the negatively charged long-chain counterpart - dimyristoyl phosphatidylglycerol (DMPG).[26, 29-32] DMPG is the negatively charged di-$C_{14}$ long-chain counterpart, the molecular structure is shown in Table 1.1.

An overview of the *Q-ratio* =3.2 DMPC/DHPC with DMPG ([DMPG]/[DMPC]=3.2) as a function of $C_{lp}$ and temperature has been summarized in Figure 1-3(b).[26] A disc-to-SUV and disc-to-lamellae transitions were found as $T > T_m$ of DMPC.[33] This transition is presumably related to the increased miscibility between DMPC and DHPC, which causes more DHPC migrate to the DMPC bilayer. As a result, the exposed hydrophobic edge drives the discs to coalesce with the neighboring discs to reduce the line tension and finally fold into the SUVs at the low lipid concentration or coalescence to lamellae at the high concentration.[33] The SUVs are considered as kinetically stable structures, and they have a uniform size distribution.[26] Both the bicellar discs and the SUVs are normally monodisperse and with diameters smaller than 100 nm – an important feature for many applications.[31, 34-38] This thesis will focus on understanding the self-assembly of bicellar system and its potential applications.

## 1.2 Important Parameters in Bicelle Formation

### 1.2.1 Packing Parameters of Amphiphilies

When the phospholipid dry powder is dispersed in water, the hydrocarbon tails of lipids tend to aggregate together, and the polar heads arrange toward the aqueous phase. The primary driving force is the *hydrophobic effect* at the hydrocarbon-water interface. The other forces include van der Waals attractions and the steric, hydration, and screened electrostatic repulsions.[1] The equilibrium of bicellar solution involves the competition between the entropic cost of separating the long- and short-chain lipids and the

substantial enthalpic penalty to mixing two lipids with different chain lengths. Thus, the bicellar morphology is significantly influenced by the lipid concentration ($C_{lp}$), temperature, and ionic strength. Doping charged lipids in bilayers are assumed to introduce more electrostatic repulsive forces between the bicellar assemblies. The effect of charge on bicelles is very similar to those on the other bilayer and micellar systems, which can be explained by the classical Derjaguin-Landau-Verwey-Overbeek (DLVO) theory (Figure 1.4).[39, 40]

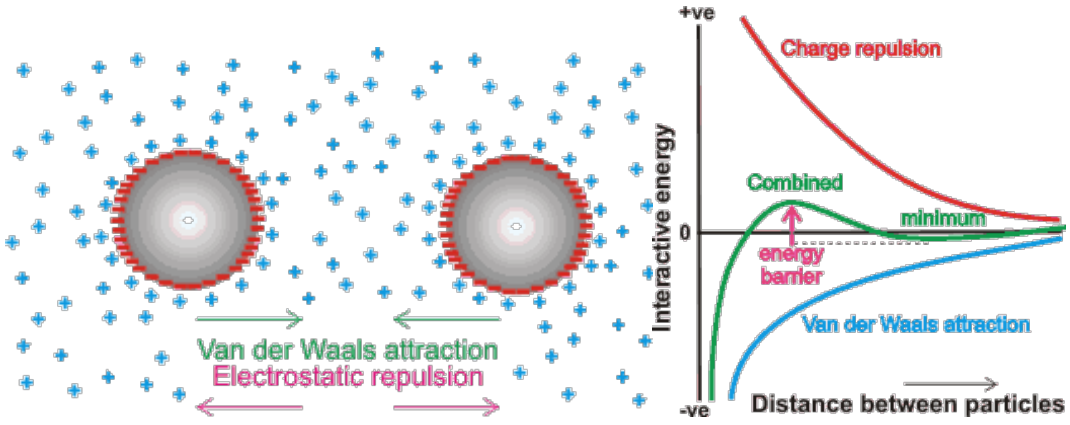


**Figure 1.4** DLVO theory assumes the particle stability depends on electrostatic double layer repulsion and long-range van der Waals attraction. For surfaces of high charge density or potential, the energy barrier will be higher thus the particles not coagulate.

The balance of the opposing forces on lipid molecules results in an optimal headgroup area with the minimum interaction energy per lipid molecule. The self-assembling morphology of a lipid system is dictated by a simple factor, i.e., *packing parameter*, *P*, which is expressed as:

$$P = \frac{v}{a_0 l_c} \qquad \text{(Eqn. 1.1)}$$

where $v$ is the chain volume, $a_0$ is the optimal interfacial area between the hydrophilic headgroup and hydrophobic tails and $l_c$ is the length of the hydrophobic tails. The molecular volume and head group areas can be determined by X-ray diffraction.[41] The formation of spherical micelles requires the large molecular optimal surface area $a_0$, the small hydrocarbon volume $v$ and the micelle radius smaller than the $l_c$. That is,

$$\frac{v}{a_0 l_c} < \frac{1}{3} \qquad \text{(Eqn. 1.2)}$$

The ranges of packing parameter for forming cylindrical micelles and bilayers are $1/3 < P < 1/2$ and $1/2 < P < 1$, respectively.

### 1.2.2 Melting Transition Temperature ($T_m$)

As mentioned in the background, $T_m$ is an important lipid property influencing the bicellar phase transition. The lipid phases and the phase transition have been extensively studied to understand physiological relevant status.[42] From the view of molecular packing, hydrocarbon chains exist in the highly ordered *all-trans* conformation *gel* phase. When temperature increases, gauche conformers are appearing in the hydrocarbon chains of lipids resulting in the relatively disordered liquid-crystalline ($L_c$) bilayers. The main phase transition happens at $T_m$ when the bilayer is in the fluid phase ($L_a$). It should be noted that $T_m$ depends significantly on the acyl chain length of the lipids, i.e., higher $T_m$

for lipids with longer tails. Differential scanning calorimetry (DSC) is the characterization tool to get the $T_m$ of different systems. The $T_m$ values of the lipids used in this thesis are listed in Table 1.1.

**Table 1.1** The structure and $T_m$ information of some commonly used phospholipids

| Name of phospholipids | Structures | $T_m$ / ºC | Reference |
|---|---|---|---|
| di-6:0 DHPC | 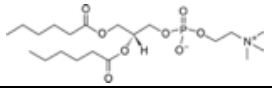 | <0 | 12 |
| di-14:0 DMPC | 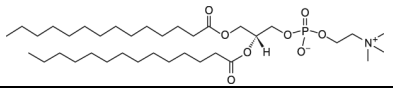 | 23 | 12 |
| di-16:0 DMPG | 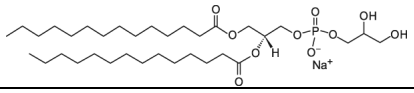 | 23 | 12 |
| di-16:0 DPPC | 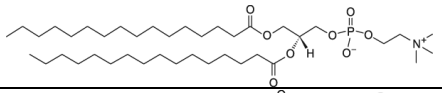 | 41 | 12 |
| di-18:0 DSPE-PEG2000 | 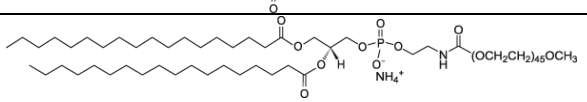 | | |

### 1.2.3 *Q-ratio* and concentration

The most important parameter in bicelle formation is the molar ratio of the long- to the short-chain lipids (*Q-ratio*). Bilayered discs or mixed micelles can exist with *Q-ratio* below 1.[6, 43-45] Early researchers assumed complete segregation of the long- and short-chain lipids referred as the "ideal bicelles".[46, 47] Thus, the *Q-ratio* was presumed to be a parameter to control the size of the "ideal bicelles" according to the amount of short-chain phospholipids which stabilizes the disc rim.

$$Q-ratio=\frac{[Long]}{[Short]}=\frac{A_{center}}{A_{rim}}=\frac{R^2}{(\pi R+2r)r} \qquad \text{(Eqn. 1.3)}$$

where the R is the center radius, r is the high-curved rim length in planar direction. (Figure 1.4)

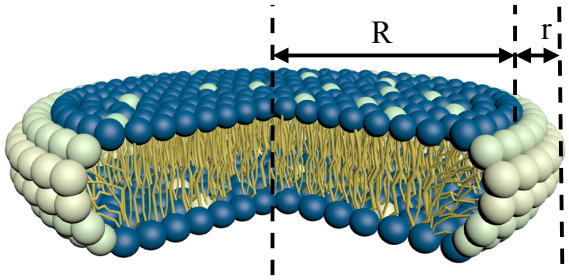


**Figure 1.4** Labelled bicelle disc structure for the refined ideal bicelle model

Experimentally, in the *Q-ratio* range 2.5 to 5, the DMPC/DHPC bicelles can orient in the magnetic field within lipid concentration ranging 30-600 mg/mL and temperatures above the $T_m$ of DMPC (30−50 °C).[18-25] However, pure DMPC (*Q-ratio* = ∞) forms multilamellar vesicles and is not magnetically alignable.[48] In the case of DMPC/DHPC mixtures, the defect pores are presumably stabilized by DHPC.[33]

Edwards *et al.* summarized the sequence of bicellar aggregates as a function of *Q-ratio* and temperature (Figure 1.5).[6] It is worthy to be noted that the bilayered discs transform into "quasi-cylindrical" micelles with increasing *Q-ratio* and temperature. The cross-section of the quasi-cylindrical micelles was ellipsoidal. They can also be referred as "ribbon-like" micelles.

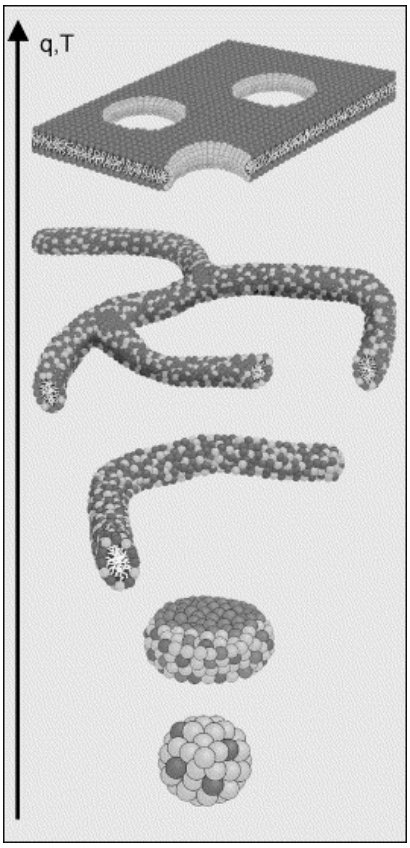


**Figure 1.5** Cartoon showing the bicellar DMPC/ DHPC aggregates as a function of either Q-ratio or temperature. From bottom to top: a mixed globular micelle; a bilayered disc with mainly DMPC in the center and DMPC and DHPC in the rim; a mixed cylindrical micelle that is slightly flattened (a quasi-cylinder); branched mixed quasi-cylindrical micelles; and a holey DMPC lamellar sheet where DHPC covers the edges of the holes. Black head groups represent DMPC, light-grey head groups represent DHPC.[6]

## 1.3 Improvement of Bicelles' Stability

Bicellar nanodiscs have great features such as the nano-size, phospholipid components, self-assembled core-shell structure, ability to transit into SUVs. In this thesis, I start with the negatively charged bicelle system, in which the formed discs have been proved to be stable in size.[49] The non-charged bicellar discs have been used in enhancing transdermal penetration.[37, 50, 51] The non-charged bicelles keep growing into

larger structures such as multilamellar vesicles. To improve the bicellar discs' stability, advanced formulation by encapsulating the discs in vesicles has been introduced for solving skin problems and trademarked as "bicosome".[52]

For *in vivo* applications, the sub-100nm particles (diameter < 100 nm) can accumulate in solid tumors through the enhanced permeability and retention (EPR) effect due to the high permeable leaky vasculature and impaired lymphatic drainage in tumor tissues.[53] Furthermore, it has been found that only particles smaller than 30 nm were able to penetrate the poorly permeable pancreatic tumors to achieve the antitumor effects.[54]

Both the bicellar discs and SUVs have the potential to be kept in the tumor tissue through EPR effect after intravenous administration. However, the foreign particles in blood circulation are quickly cleared by the mononuclear phagocytic system (MPS), also known as the reticuloendothelial system (RES).[55] To prolong the injected particles' blood circulation time, a general approach is to graft Polyethylene Glycol (PEG) on the particles' surface, thus making the particles be "invisible" to RES.[56, 57]

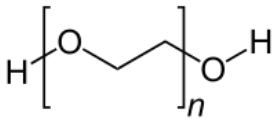


**Figure 1.6** Chemical Structure of Polyethylene Glycol (PEG)

PEGylated liposomes have been broadly developed as tumor-targeting drug delivery carriers.[58] However, the conventional SUVs manufacturing extrusion and sonication

methods are time and energy consuming. The self-assembled SUVs from bicelles are much less labor intensive and requires less processing time. The bicelle template has a great potential to be used as a major tool in industrial liposome production. The bicellar nanodiscs are in the novel category of the non-spherical nanocarriers, which may have their shape impact in future applications.

### 1.4 Interaction of Bicelles and Pluronics

The Pluronic® block copolymers of Polyethylene Glycol (PEG) and Polypropylene Glycol (PPG) constitute various of surfactants and have widespread application in different areas, especially for biomedical applications.[59-61] The chemical structure of the PEG-PPG-PEG Pluronics is shown in Figure 1.7. With the PEG subunits, Pluronics can accomplish the steric stabilization purpose and can be the substitute for PEG-lipids as components in therapeutic carriers.[62] Particular interest has been put on investigations of Pluronics with lipid assemblies, for understanding the function of Pluronics on cell membrane.[63-65]

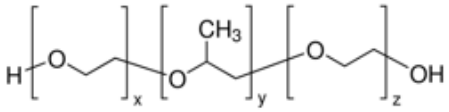


**Figure 1.7** PEG-PPG-PEG Pluronic tri-block copolymer structure. x, y, z are the numbers of repeat unites.

Only a few studies have focused on the Pluronics in the bicelle membrane model system.[35] The research on reverse Pluronics and bicelle mixture is zero. It is valuable to reveal the unexplored realm of fundamental science and applications of Pluronic and

bicelle mixtures system, such as the interaction of Pluronic and cell membrane and advanced superstructure production.

**1.5 Objectives**

The first goal of this thesis is to make the "PEGylated" bicellear discs and SUVs at the nanoscale. The commonly used PEGylated distearoyl phosphoethanolamine (DSPE-PEG) is selected to be incorporated in the bicellar mixture. (Table 1.1) The PEGylated bicelle system will be compared with the non-PEG system at the different concentration, temperature and salt conditions.

Based on the fundamental of the first goal, the second objective is to understand further the effects of DSPE-PEG on the structural and thermal stability of bicelles. The PEG corona on nanoparticles is considered to repel plasma protein adsorption by reducing the long-range attractive force.[66] The corona thickness and PEG chain conformation greatly influence the nanoparticles' stability and *in vivo* fate. The PEG chain conformation looks like an integrated "mushroom" or "brush" at different chain length and surface density greatly. The "brush" conformation is preferred for a longer time systematic circulation[67]. The optimal PEG-lipid ratio for liposome's maximum stability is 5~7 mol%.[68] How do the mushroom-brush theory work with the bicelles? The bicelles with different PEG chain length and surface density will be tested.

A reverse Pluronic PPG-PEG-PPG is expected to have its PPG ends inserted the bilayers and the middle PEG block in water when mixed with lipid bilayers. With this property, reverse Pluronic can act as a “linker” between bicellar discs. The third goal of this thesis is to “string” bicellar discs with the reverse Pluronic copolymer to understand the kinetics of “stringing” mechanism and structures of the “strung” discs.

## 1.6 References


1. J. N. Israelachvili, *Intermolecular and surface forces: revised third edition*. (Academic press, 2011).
2. D. Nath, Nature **438** (7068), 577-577 (2005).
3. A. Arora, F. Abildgaard, J. H. Bushweller and L. K. Tamm, Nat Struct Mol Biol **8** (4), 334-338 (2001).
4. G. Da Costa, S. Chevance, E. Le Rumeur and A. Bondon, Biophysical journal **90** (8), L55-L57 (2006).
5. F. M. Marassi and S. J. Opella, Protein Science **12** (3), 403-411 (2003).
6. L. Van Dam, G. Karlsson and K. Edwards, Biochimica et Biophysica Acta - Biomembranes **1664** (2), 241-256 (2004).
7. P. Ram and J. Prestegard, Biochimica et Biophysica Acta (BBA)-Biomembranes **940** (2), 289-294 (1988).
8. C. R. Sanders and G. C. Landis, Biochemistry **34** (12), 4030-4040 (1995).
9. C. R. Sanders and K. Oxenoid, Biochimica et Biophysica Acta (BBA) - Biomembranes **1508** (1–2), 129-145 (2000).
10. A. A. De Angelis and S. J. Opella, Nat. Protocols **2** (10), 2332-2338 (2007).
11. J. K. Claridge, J. Aittoniemi, D. M. Cooper and J. R. Schnell, Biochemistry **52** (47), 8420-8429 (2013).
12. R. N. Lewis, N. Mak and R. N. McElhaney, Biochemistry **26** (19), 6118-6126 (1987).
13. C. R. Sanders and J. P. Schwonek, Biochemistry **31** (37), 8898-8905 (1992).
14. R. R. Vold, R. S. Prosser and A. J. Deese, J Biomol NMR **9** (3), 329-335 (1997).
15. C. R. Sanders and R. S. Prosser, Structure **6** (10), 1227-1234 (1998).
16. M.-P. Nieh, C. J. Glinka, S. Krueger, R. S. Prosser and J. Katsaras, Langmuir **17** (9), 2629-2638 (2001).
17. R. S. Prosser, J. S. Hwang and R. R. Vold, Biophysical journal **74** (5), 2405-2418 (1998).
18. L. Czerski and C. R. Sanders, Analytical Biochemistry **284** (2), 327-333 (2000).
19. S. Faham and J. U. Bowie, Journal of Molecular Biology **316** (1), 1-6 (2002).
20. M. Caffrey, Journal of Structural Biology **142** (1), 108-132 (2003).
21. L. C. Johansson, A. B. Wöhri, G. Katona, S. Engström and R. Neutze, Current Opinion in Structural Biology **19** (4), 372-378 (2009).
22. A. C. Kimble-Hill, Frontiers in Biology **8** (3), 261-272 (2013).
23. A. Diller, C. Loudet, F. Aussenac, G. Raffard, S. Fournier, M. Laguerre, A. Grélard, S. J. Opella, F. M. Marassi and E. J. Dufourc, Biochimie **91** (6), 744-751 (2009).
24. U. H. Dürr, M. Gildenberg and A. Ramamoorthy, Chemical reviews **112** (11), 6054-6074 (2012).
25. S. Poulos, J. L. Morgan, J. Zimmer and S. Faham, Methods in enzymology **557**, 393-416 (2015).
26. M.-P. Nieh, P. Dolinar, N. Kučerka, S. R. Kline, L. M. Debeer-Schmitt, K. C. Littrell and J. Katsaras, Langmuir **27** (23), 14308-14316 (2011).

27. J. Katsaras, T. A. Harroun, J. Pencer and M.-P. Nieh, Naturwissenschaften **92** (8), 355-366 (2005).
28. M.-P. Nieh, N. Kučerka and J. Katsaras, Methods in enzymology **465**, 3-20 (2009).
29. J. Losonczi and J. Prestegard, J Biomol NMR **12** (3), 447-451 (1998).
30. A. Hu, T.-H. Fan, J. Katsaras, Y. Xia, M. Li and M.-P. Nieh, Soft Matter **10** (28), 5055-5060 (2014).
31. M. P. Nieh, C. J. Glinka, S. Krueger, R. Scott Prosser and J. Katsaras, Biophysical Journal **82** (5), 2487-2498 (2002).
32. R. Vácha and D. Frenkel, Langmuir **30** (15), 4229-4235 (2014).
33. M. P. Nieh, V. A. Raghunathan, S. R. Kline, T. A. Harroun, C. Y. Huang, J. Pencer and J. Katsaras, Langmuir **21** (15), 6656-6661 (2005).
34. M. P. Nieh, V. A. Raghunathan, C. J. Glinka, T. A. Harroun, G. Pabst and J. Katsaras, Langmuir **20** (19), 7893-7897 (2004).
35. R. Soong, M. P. Nieh, E. Nicholson, J. Katsaras and P. M. MacDonald, Langmuir **26** (4), 2630-2638 (2010).
36. M. P. Nieh, V. A. Raghunathan, G. Pabst, T. Harroun, K. Nagashima, H. Morales, J. Katsaras and P. MacDonald, Langmuir **27** (8), 4838-4847 (2011).
37. L. Barbosa-Barros, A. De La Maza, J. Estelrich, A. M. Linares, M. Feliz, P. Walther, R. Pons and O. López, Langmuir **24** (11), 5700-5706 (2008).
38. D. D. Lasic, Trends in biotechnology **16** (7), 307-321 (1998).
39. V. Degiorgio and M. Corti, *Physics of Amphiphiles--micelles, Vesicles, and Microemulsions, 1983: Varenna on Lake Como, Villa Monastero, 19-29 July 1983*. (North Holland, 1985).
40. J. A. Losonczi and J. H. Prestegard, J Biomol NMR **12** (3), 447-451 (1998).
41. J. F. Nagle and S. Tristram-Nagle, Biochimica et Biophysica Acta (BBA)-Reviews on Biomembranes **1469** (3), 159-195 (2000).
42. M. J. Janiak, D. M. Small and G. G. Shipley, Biochemistry **15** (21), 4575-4580 (1976).
43. K. J. Glover, J. A. Whiles, G. Wu, N.-j. Yu, R. Deems, J. O. Struppe, R. E. Stark, E. A. Komives and R. R. Vold, Biophysical Journal **81** (4), 2163-2171 (2001).
44. A. Andersson and L. Mäler, Langmuir **21** (17), 7702-7709 (2005).
45. W. Ye, J. Lind, J. Eriksson and L. Mäler, Langmuir **30** (19), 5488-5496 (2014).
46. R. R. Vold and R. S. Prosser, Journal of Magnetic Resonance, Series B **113** (3), 267-271 (1996).
47. D. Small, S. Penkett and D. Chapman, Biochimica et Biophysica Acta (BBA)-Lipids and Lipid Metabolism **176** (1), 178-189 (1969).
48. P. L. Yeagle, *The structure of biological membranes*. (CRC press, 2010).
49. S. Mahabir, W. Wan, J. Katsaras and M.-P. Nieh, Journal of Physical Chemistry B **114** (17), 5729-5735 (2010).
50. L. Barbosa-Barros, C. Barba, M. Cócera, L. Coderch, C. López-Iglesias, A. de la Maza and O. López, International Journal of Pharmaceutics **352** (1-2), 263-272 (2008).
51. L. Barbosa-Barros, G. Rodríguez, C. Barba, M. Cócera, L. Rubio, J. Estelrich, C. López-Iglesias, A. de la Maza and O. López, small **8** (6), 807-818 (2012).

52. E. Fernández, L. Fajarí, G. Rodríguez, C. López-Iglesias, M. Cócera, L. Barbosa-Barros, A. de la Maza and O. López, RSC Advances **4** (95), 53109-53121 (2014).
53. Y. Matsumura and H. Maeda, Cancer research **46** (12 Part 1), 6387-6392 (1986).
54. H. Cabral, Y. Matsumoto, K. Mizuno, Q. Chen, M. Murakami, M. Kimura, Y. Terada, M. Kano, K. Miyazono and M. Uesaka, Nature nanotechnology **6** (12), 815-823 (2011).
55. J. Kreuter, *Colloidal drug delivery systems*. (CRC Press, 1994).
56. A. L. Klibanov, K. Maruyama, V. P. Torchilin and L. Huang, FEBS Letters **268** (1), 235-237 (1990).
57. A. Gabizon and F. Martin, Drugs **54** (4), 15-21 (1997).
58. H. Maeda, G. Bharate and J. Daruwalla, European Journal of Pharmaceutics and Biopharmaceutics **71** (3), 409-419 (2009).
59. D. Zhao, J. Feng, Q. Huo, N. Melosh, G. H. Fredrickson, B. F. Chmelka and G. D. Stucky, science **279** (5350), 548-552 (1998).
60. C. Wu, T. Liu, B. Chu, D. K. Schneider and V. Graziano, Macromolecules **30** (16), 4574-4583 (1997).
61. A. V. Kabanov, E. V. Batrakova and V. Y. Alakhov, Journal of controlled release **82** (2), 189-212 (2002).
62. D. E. Owens Iii and N. A. Peppas, International Journal of Pharmaceutics **307** (1), 93-102 (2006).
63. S. A. Maskarinec and K. Y. C. Lee, Langmuir **19** (5), 1809-1815 (2003).
64. M. A. Firestone, A. C. Wolf and S. Seifert, Biomacromolecules **4** (6), 1539-1549 (2003).
65. T. Demina, I. Grozdova, O. Krylova, A. Zhirnov, V. Istratov, H. Frey, H. Kautz and N. Melik-Nubarov, Biochemistry **44** (10), 4042-4054 (2005).
66. A. Vonarbourg, C. Passirani, P. Saulnier and J.-P. Benoit, Biomaterials **27** (24), 4356-4373 (2006).
67. R. Gref, M. Lück, P. Quellec, M. Marchand, E. Dellacherie, S. Harnisch, T. Blunk and R. Müller, Colloids and Surfaces B: Biointerfaces **18** (3), 301-313 (2000).
68. T. Allen, C. Hansen, F. Martin, C. Redemann and A. Yau-Young, Biochimica et Biophysica Acta (BBA)-Biomembranes **1066** (1), 29-36 (1991).

# Chapter 2 Characterization Methods

## 2.1 Classical Scattering Theory

In the field of colloid system characterizations, scattering techniques such as neutron, X-ray and light scatterings are very useful for detecting the size and shape of nanoparticles and the inter-particle interactions in solutions. All the radiation resources are propagating electromagnetic waves. The featured difference among these waves is the frequency of oscillation $v$. Therefore, the wavelength $\lambda$ and velocity $c$ are related by

$$c = \lambda v \qquad \text{(Eqn. 2.1)}$$

Once a plane monochromatic wave $A_o \exp(i\boldsymbol{q_0}\mathbf{r})$ incident at a point scattering center in a non-absorbing medium, a secondary spherical wave will be generated as

$$A_o \exp(i\boldsymbol{k_o}\mathbf{r}) + (A_o b/r)\exp(i\boldsymbol{k}\mathbf{r}) \qquad \text{(Eqn. 2.2)}$$

where $A_o$ and $A_o b/r$ are the scattering amplitudes of the two waves. $\mathbf{r}$ is the vector which determines an observation point corresponding to the scattering center. $b$ is the scattering length. $\boldsymbol{k_o}$and $\boldsymbol{k}$ are the incident and scattering wave vectors with $|\boldsymbol{k_o}| = |\boldsymbol{k}| = 2\pi/\lambda$. Therefore the scattering vector $\boldsymbol{q} = \boldsymbol{k_o} - \boldsymbol{k} = (4\pi/\lambda)\sin(\theta)$, where the $2\theta$ stands for the scattering angle between $\boldsymbol{k_o}$ and $\boldsymbol{k}$. (Figure 2.1)

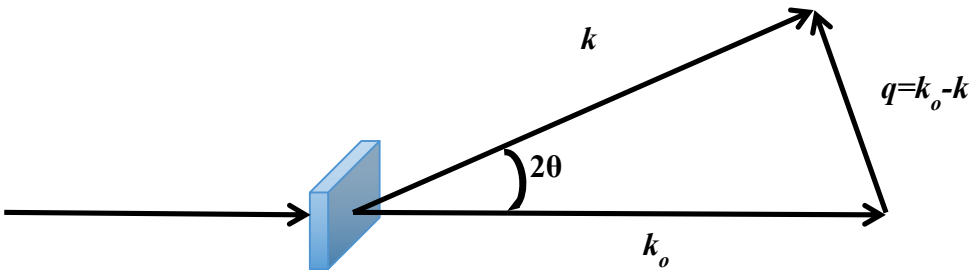


**Figure 2.1** The scattering vector ***q*** is defined by the geometry.

The scattering ability of objects usually represents as scattering density function φ(r). In the case of X-ray and light scattering, the incident beams are interacting with electrons of samples; therefore, φ(r) stands for the distribution of the electric charge density. For neutron scattering, φ(r) represents the nuclear and spin density distribution.

## 2.2 Small Angle Neutron Scattering (SANS)

### 2.2.1 Principle

The neutron was discovered by James Chadwick in 1932.[1, 2] Four years later, Halban and Preiswerk and Mitchell and Powers demonstrated the neutrons behaved as waves and can be diffracted by crystalline matter as X-rays.[3, 4] The first neutron scattering experiments were conducted in 1944 when the atomic pile in *Manhattan project* could produce high-intensity neutron beams. The theory and practice of SANS developed in the early 1970s when the position-sensitive detectors were available on the cold neutron source.

Compared to X-ray, the neutron beam is less radiation damage to biological samples. In a sample characterization experiment, the neutron beams are guided to interact with the sample and partially scattered onto a detector downstream. Deuterated water is usually used to replace protonated water to increase the contrast between the solute and the solvent for neutron scattering experiments. Therefore, SANS has been applied to a broad range of research fields

especially important in characterizing biological structures. SANS can provide the information about the size, shape and orientation of the detected samples. The $q$ range of SANS covered is about $5\times10^{-3}$ to 0.5 $Å^{-1}$, which is 10 to 1000 Å in real space scale.

The obtained SANS intensity from a particulate system, $I(q)$ is proportional to the Fourier transform square of the density fluctuation function of the detected sample. $I(q)$is proportional to the number density of particles (or concentration of the aggregates, $C$), the contrast factor ($\Delta\rho^2$, square of the difference in neutron scattering length densities, NSLDs, between the object and medium), the form factor describing the shape of the particles [i.e., $P(q)$] and the structure factor describing the inter-particle interactions [i.e., $S(q)$]. As a result, $I(q)$ can be expressed as:

$$I(q) = C\,\Delta\rho^2 P(q)\,S(q) \qquad \text{(Eqn. 2.3)}$$

Several mathematical models are used to fit the scattered intensity of experimental data.

**a) Polydisperse Radius Disc (PR-Disc) Model**

When the inter-particle interactions are negligible in solution, the structure factor effect can be cancelled out ($S(q) = 1$). The structural parameters are then obtained from fitting the proposed form factor $P(q)$ to the experimental data. The nanodiscs can be described by the polydisperse radius disc (PR-Disc) model, which assumes a flat cylinder with a radius $R$ and its polydispersity $p$, and the disc' thickness $t$ of a uniform neutron scattering length density (Figure 2.2).

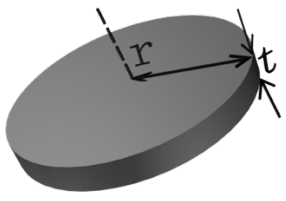


**Figure 2.2** The sketch of disc with a thickness of t (=2H) and a radius of r.

The derived mathematic size averaged form factor for PR-Disc ($q$) can be expressed as

$$\overline{P_{PRD}(q)} = \int_0^{\infty} \frac{scale}{V_{PRD}} f(r)dr \int_0^{\pi/2} A_{PRD}^2(q,\alpha)\sin\alpha\, d\alpha \qquad \text{(Eqn. 2.4)}$$

$$A_{PRD}(q,\alpha) = 2V_{PRD}(\rho_{lip} - \rho_{D_2O}) j_0(\frac{qt}{2}\cos\alpha)\frac{J_1(qr\sin\alpha)}{(qr\sin\alpha)} \qquad \text{(Eqn. 2.5)}$$

where $\alpha$ is the angle between bilayer normal and scattering vector, $q$. The thickness, average volume and scattering amplitude of the discs are $t$, $V_{PRD}$ and $A_{PRD}(q,\alpha)$, respectively. The scattering length densities of phospholipids and $D_2O$ are $\rho_{lip}$ and $\rho_{D2O}$. The functions $J_1$ (x) and $j_o$ (x) are the Bessel functions of the first kind and (sin $x$)/$x$, respectively. Eq. (4) includes the average over all possible orientations and various sizes of discs according to the Schulz distribution. It should be noted that the average volume of the discs could be approximated as

$$V_{PRD} = \pi r^2 t(\frac{z+2}{z+1}) \qquad \text{(Eqn. 2.6)}$$

which is based on the Schulz distribution $\quad f(r) = (z+1/r_{av})^{z+1} r^z \frac{\exp[-(z+1)r/r_{av}]}{\Gamma(z+1)} \qquad \text{(Eqn. 2.7)}$

$r_{av}$ is the average radius. z can be related to polydispersity, $p$.

$$z = 1/p^2 \ - 1 \qquad \text{(Eqn. 2.8)}$$

**b) Polydisperse Radius Unilamellar Vesicle (PR-ULV) model**

In regard to unilamellar vesicle, whose structure is a spherical bilayer shell with a hollow aqueous core as shown in Figure 2.3.

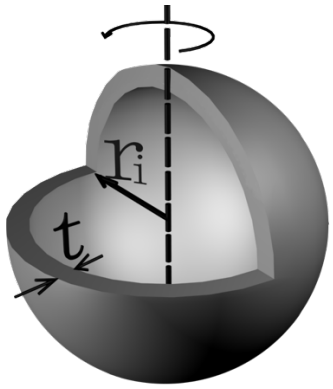


**Figure 2.3** The sketch of ULV, whose bilayer thickness is t and inner radius is r

It is known that the thickness of the bilayer shell *t,* is nearly constant at a specific temperature and that the bilayer has a reasonably uniform scattering length density across the membrane in comparison with the drastic difference between $D_2O$ and the bilayer. The shell can be approximated as a single layer with a uniform scattering length density and a constant thickness. Moreover, the radius of the ULV core is allowed to vary within a certain range of polydispersity. Overall, the form factor of ULVs $P_{\mathrm{ULV}}(q)$ can be described by the polydisperse radius unilamellar vesicle (PR-ULV) model as the following equation.

$$\overline{P_{ULV}(q)} = \frac{scale}{V_{ULV}} \int_0^{\infty} f(r) A_{ULV}^2(q,r)\, dr \qquad \text{(Eqn. 2.9)}$$

$$A_{ULV}(q,r) = \frac{4\pi(\rho_{lip} - \rho_{D_2O})}{q^3}\left[\sin[q(r+t)] - q(r+t)\cdot\cos[q(r+t)] - \sin(qr) + qr\cdot\cos(qr)\right] \qquad \text{(Eqn. 2.10)}$$

where $V_{ULV}$, $f(r)$ and $A_{ULV}(q,r)$ are the individual ULV volume, the Schulz distribution and the scattering amplitude of the ULV with an inner radius of $r$ and thickness of $t$. $\rho_{lip}$, $\rho_{D2O}$ and are the scattering length densities of the lipid bilayer and $D_2O$.

The polydispersity, $p$ of the inner radius in the Schulz distribution function is defined as the ratio of standard deviation $\sigma$ of radius, to the average of radius $r_{av}$, $p = \sigma/r_{av}$.

The Schulz distribution function can be expressed as

$$f(r) = \frac{p^{-2/p^2}}{r_{av}\Gamma(1/p^2)}\left(\frac{r}{R_1}\right)^{(1-p^2)/p^2}\exp\left(-\frac{r}{p^2 r_{av}}\right) \qquad \text{(Eqn. 2.11)}$$

where $\Gamma(x)$ is the gamma function.

**(c) Single-Shell Oblate (SS-Oblate) model**

The single-shell oblate (SS-Oblate) model (with two identical long-axes and one short-axis) was used to fit the SANS data as shown in Figure 2.4.

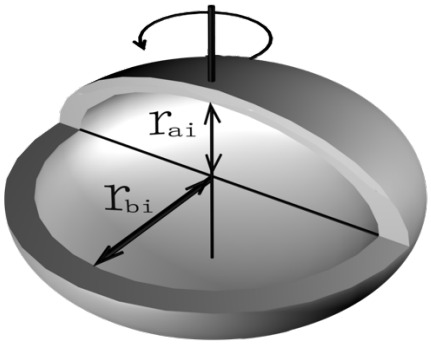


**Figure 2.4** The sketch of single-shell oblate with the inner minor radius ($r_{ai}$) and major radius ($r_{bj}$), and an outer minor radius ($r_{ao}$) and an outer major radius ($r_{bo}$)

This model contains four independent parameters to describe the dimension of the particle, namely the major ($r_{bi}$) and minor ($r_{ai}$) axes of the core and the major ($r_{bo}$) and minor ($r_{ao}$) axes of the shell. The form factor and scattering amplitude of SS-Oblate model, i.e., $P_{SS\text{-}Oblate}(q)$ and $A_{SS\text{-}Oblate}(q)$ can be expressed as

$$P_{SS-Oblate}(q) = \frac{1}{V_O}\int_0^1 \left|A_{SS-Oblate}(q, r_i, \beta)\right|^2 d\beta \qquad \text{(Eqn. 2.12)}$$

$$A_{SS-Oblate}(q, r_i, \beta) = 3(\rho_{D_2O} - \rho_{lip})\left[\frac{V_i j_1(u_i)}{u_i} - \frac{V_o j_1(u_o)}{u_o}\right] \qquad \text{(Eqn. 2.13)}$$

The core and total volumes ($V_i$ and $V_o$) can be mathematically derived as

$$V_i = (4\pi/3) r_{bi}^2 r_{ai} \qquad \text{(Eqn. 2.14)}$$

$$V_o = (4\pi/3) r_{bo}^2 r_{ao} \qquad \text{(Eqn. 2.15)}$$

$$u_i = q[r_{bi}^2(1-\beta^2) + r_{ai}^2\beta^2]^{1/2} \qquad \text{(Eqn. 2.16)}$$

$$u_o = q[r_{bo}^2(1-\beta^2) + r_{ao}^2\beta^2]^{1/2} \qquad \text{(Eqn. 2.17)}$$

$$\beta = \cos\alpha \qquad \text{(Eqn. 2.18)}$$

$$j_1(x) = (\sin x - x\cos x)/x \qquad \text{(Eqn. 2.19)}$$

It should be noted that the OSS model assumes monodisperse particles and the peak smearing in the SANS patterns is mainly due to the different lengths and shell thicknesses along the long- and short-axes.

**(d) Hayter-Penfold structure factor**

In the case of strong inter-particle interaction, the structure factor is described by Hayter-Pendfold $S(q)$ accounting for the Coulombic interaction among the ionic particles since the system is highly charged in the absence of salt.[5] $S(q)$ can be related to the approximated potential

$U(r)$, between two identical spherical macroions whose surface potentials and diameters are $\psi_o$ and d, respectively.[5] If the average center-to-center distance of the particles is $r$, $U(r)$ can be expressed as the following equation.

$$U(r) = \pi\varepsilon_0\varepsilon d^2\psi_0^2 \exp[-\kappa(r-d)]/r_0 \qquad \text{(Eqn. 2.20)}$$

where $\varepsilon_o$, $\varepsilon$ and $1/\kappa$ are the permittivity of the solution, the dielectric constant and the Debye-Hückle length. The surface potential is related to the electronic charge $z_m$ on the macroion to a good approximation by

$$\psi_0 = z_m / \pi\varepsilon_0\varepsilon\sigma(2+\kappa\sigma) \qquad \text{(Eqn. 2.21)}$$

where the final term reflects the mutual exclusion by the macroions of counterions from each other's volume.

### 2.2.2 Instruments and Experimental Conditions

The SANS data in this thesis were collected at the EQ-SANS instrument in the Spallation Neutron Source of Oak Ridge National Laboratory and the NG3 30-m instrument in National Institute of Standards and Technology (NIST) Center for Neutron Research. The sample-to-detector distance was set to 4.0 m. A 25-mm-source aperture and a 10 mm sample aperture were used to collimate the incident beam. The instrument was operated in the 30 Hz frame-skipping mode with a minimum wavelength of 2.5 Å, providing a second wavelength band starting at 9.4 Å. The combined $q$-range can cover 0.007 ~ 0.40 $Å^{-1}$ for data reduction and analysis. The useful $q$ range for the data fitting was from 0.007 to 0.25 $Å^{-1}$. Data correction followed standard procedures implemented in MantidPlot (http://www.mantidproject.org/) to correct for sample transmission, detector sensitivity, and dark background before circularly averaging the 2D data

around the beam center to produce I($q$) versus $q$. The data from the two wavelength bands were connected into a single profile through MantidPlot. The reduced SANS data were then fitted with appropriate models available at NIST (National Institute of Standards and Technology) Center for Neutron Research (NCNR) in the format of *IGOR-PRO* program.[6, 7]

## 2.3 Small Angle X-ray Scattering (SAXS)

SAXS measurements were taken using Bruker Nanostar at University of Connecticut. The sample-detector distances were 107 cm, calibrated using a powder sample of silver behenate in quartz capillary. Lipid dispersions were taken up in 1.5mm thick quartz capillaries and inserted into a temperature controlled sample stage. The scattering intensity, $I$, was collected as a function of scattering vector, $q$, defined as $q = (4\pi)/\lambda \; sin \; (\theta/2)$, where $\lambda$ and $\theta$ are the wavelength and scattering angle, respectively. In SAXS, the $\lambda$ is 1.5 Å and $q$ range is from 0.007 to 0.22 $Å^{-1}$. Background scattering originating from air was subtracted, and data sets were normalized using the transmitted intensity, which was measured by a 32-fold Aluminum foil placed in front of the beamstop. The empty cell scattering intensity was subtracted from all SAXS curves. The data fitting was done by Igor Pro software.

The fitting model for the SAXS data of disc-shaped particles is the Polydisperse Radius Core-Shell Discs (PR-CS-Disc).

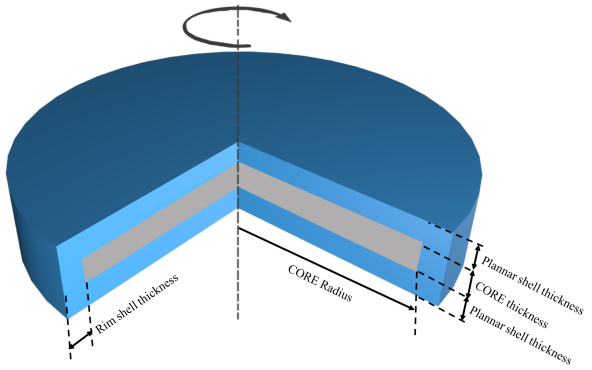


**Figure 2.5** The sketch of Polydisperse Radius Core-Shell Disc (*Poly-CS-Disc*) model for SAXS data fitting.

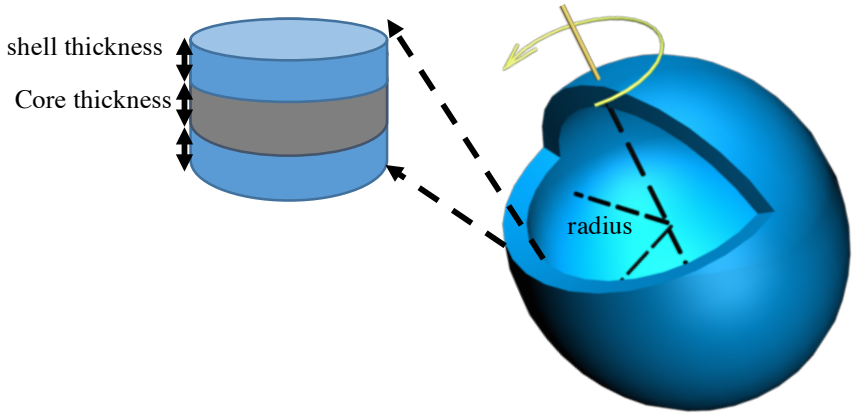


**Figure 2.6.** The sketch of three-shell vesicle model for SAXS data fitting.

The hydrophilic headgroups are the shell while the hydrophobic tails are the bilayer core. The scattering length densities are as follows:[8]

$\Delta\rho_{water} = 9.47 \times 10^{-6}$ Å$^{-2}$; $\Delta\rho_{core} = 8.6 \times 10^{-6}$ Å$^{-2}$;

$\Delta\rho_{shell\ at\ 25\ °C} = 1.15 \times 10^{-5}$ Å$^{-2}$; $\Delta\rho_{shell\ at\ 60\ °C} = 4.8 \times 10^{-6}$ Å$^{-2}$

## 2.4 Dynamic Light Scattering (DLS)

### 2.4.1 Principle

In 1871, John William Strutt, known as Lord Rayleigh, explained why the sky appeared in blue color by assuming that the size of light scattered particles was much smaller than the wavelength of light. Thirty years later, he suggested that not only the particles but also the molecules in the atmosphere were in responsible for light scattering. The light scattering from translational and rotational degrees of freedom was named *Rayleigh scattering*. The *Rayleigh scattering* theory was further developed through the efforts of Rayleigh, Mie, Smoluchowski, Einstein, Debye and so on. In 1964, Debye, Zimm and their co-workers developed the "static light scattering" (SLS) to study the molecule weights, sizes and shapes of macromolecules in solutions.

Since the development of photonic parts such as laser resource, Fabry-Perot interferometers using "optical beating" technique and digital correlation spectroscopy in 1970s, the dynamic properties of particles in solution can be identified by the "quasi-elastic light scattering", which was broadly used in studying colloid systems and named as "dynamic light scattering" (DLS) later. DLS detects the decay and increase of fluctuations in a spatial Fourier component of the refractive index of wavelength $2\pi\boldsymbol{q}^{-1}$.

Brownian motion of isolated particles is one of the major particle interactions influencing the intensity fluctuations in dynamic light scattering. The simplest information to get is the translational diffusion constant, which can be expressed by the Stokes-Einstein relation,

$$D = k_B T/6\pi\eta r \qquad \text{(Eqn. 2.22)}$$

$k_B$ — Boltzman constant

T — temperature

$\eta$ — viscosity

$r$ — hydrodynamic radius of the scattered molecule

The experimental setup of DLS includes a laser beam of coherent light shining on a sample tube in the center of a quartz crystal sample stage with an index-matching fluid such as toluene. The index-matching fluid having the similar refractive index with glass is to reduce the light reflection on the pathway. DLS is measuring the fluctuated intensity of the laser scattered from mobile particles to tell the diffusion behavior of the colloid system.

If the scattering volume contains $N$ molecules of particles and irradiates with light of angular frequency $\omega_0$, the scattered electric field at time $t$ is

$$E_s(q,t) = \sum_{j=1}^{N} A_j(t) \exp\left\{ i\left[ \omega_0 t - \vec{q} \cdot \vec{r}_j(t) \right] \right\} \qquad \text{(Eqn. 2.23)}$$

The scattering vector $\vec{q}$, is also used in SANS to describe the propagation of the incident electromagnetic wave. The time-averaged scattered intensity of molecules with smaller dimension than $\lambda$ can be expressed by

$$\langle I_S \rangle = \langle |E_s| \rangle^2 = \frac{4\pi^2 N M^2 (\sin^2 \Phi)(dn/dc)^2 I_0}{N_A^2 \lambda^4 R^2} \qquad \text{(Eqn. 2.24)}$$

N — the number of scattered molecules

*M* — molecular weight of the scattered molecule in Daltons

*dn/dc* — the rate of change of refractive index of the solution as the concentration of the solute is changed

$I_0$— the incident light intensity

$N_A$— Avogadro's number

*R* — the distance from the scattering point to the observation point

The field autocorrelation function

$$g^{(1)}(\tau) = \frac{\langle E_S^*(t) E_S(t+\tau) \rangle}{\langle I \rangle} \qquad \text{(Eqn. 2.25)}$$

The measured intensity autocorrelation function

$$g^{(2)}(\tau) = \frac{\langle E_S^*(t) E_S(t)_S E_S^*(t+\tau) E_S(t+\tau) \rangle}{\langle I \rangle^2} \qquad \text{(Eqn. 2.26)}$$

When the scattered field is Gaussian with zero mean, as will normally be the case for a solution of diffusing macromolecular scatterers, then these autocorrelation functions are connected by the Siegert relation

$$g^{(2)}(\tau) = 1 + \left| g^{(1)}(\tau) \right|^2 \qquad \text{(Eqn. 2.27)}$$

In the experimental measurements, the particle fluctuations can be carried out by a spectrum analyzer or a correlator. In the correlation techniques, the relationship of the scattered intensity and the decay time can be expressed in the time-dependent correlation function

$$G(\tau) = \lim_{T \to \infty} \frac{1}{2T} \int_{-T}^{T} I(t) J(t+\tau) d(t) \qquad \text{(Eqn. 2.28)}$$

*I(t)* and *J(t)* are signals depending upon time. *G(τ)* stands for the autocorrelation function or cross correlation function when I(t) and J(t) are the same or different signals. This correlation function can be shown to be the Fourier transform of the power spectrum

$$G(\tau) = 1 + e^{-2Dq^2\tau} \qquad \text{(Eqn. 2.29)}$$

In practical experiments, $\tau$ can be measured by the intensity–intensity time auto-correlation function $G^{(2)}(t)$, defined as $\langle I(0)I(t)\rangle / \langle I\rangle^2$. $\langle I\rangle$ is the time-average scattered intensity. $G^{(2)}(t)$ is related to the field-field correlation function $g^{(1)}(t)$ by the Siegert relation.

$$G^{(2)}(t) = A\left[1 + \beta \left| g^{(1)}(t) \right|\right] \qquad \text{(Eqn. 2.30)}$$

where $A$ is the measured baseline, $\beta$ is the correction factor that depends on the laser beam property. For monodisperse spherical particles, $|g^{(1)}(t)|$ can be theoretically represented as an exponential decay function

$$\left|g^{(1)}(t)\right| = Ge^{-\Gamma t} \qquad \text{(Eqn. 2.31)}$$

where $G$ and $\Gamma$ are the factor of proportionality and the line width $1/\tau$, respectively. For a polydisperse dynamic relaxation, Eqn. 2.31 may be generalized as

$$\left|g^{(1)}(t)\right| = \int_0^\infty G(\Gamma)e^{-t\Gamma}\, d\Gamma \qquad \text{(Eqn. 2.32)}$$

where $G(\Gamma)$ is called the line-width distribution and $G(\Gamma)\, d\Gamma$ is the statistic weight of the dynamic relaxation, which possess the line width or be related to the particle size distribution in dilute solution.

$G^{(2)}(t)$ can lead to $G(\tau)$ on the basis of Eqn. 2.30 and 2.32 by Laplace inversion. $\Gamma(1/\tau)$ is related to the translational diffusion coefficient, $D = \Gamma/q^2$, in a diffusive relaxation, so that $G(\tau)$ can be converted into a transitional diffusion coefficient distribution $G(D)$ or further a hydrodynamic radius distribution $f(R_H)$ by means of the Stokes–Einstein equation.

$$D = \frac{k_B T}{6\pi\eta_0 R_H} \qquad \text{(Eqn. 2.33)}$$

where $k_B$, $T$ and $\eta_0$ are the Boltzmann constant, the absolute temperature and the solvent viscosity, respectively.

In the charged system, the electrostatic interactions contribute to the inter-particle motions. The resulted sharp rapid fluctuation usually shows a smaller $\tau$ than the one under Brownian motion only, which can be categorized as the fast relaxation mode. However, a slow relaxation mode has also been commonly observed in all polyelectrolytes solutions. The current interpretation of the slow mode in DLS is still very controversial.[9]

### 2.4.2 Instrument and Experimental Conditions

The DLS instruments used in this thesis are ALV compact goniometer system with multi-detectors (CGS-3MD) (Germany) and the Zetasizer Nano HPPSv420 (Malvern Instruments, Ltd., Malvern, UK).

The ALV DLS instrument consists of a 22-mW UNIPHASE He–Ne laser (emitting vertically polarized light with a wavelength of 632.8 nm) and four avalanche photo diode (APD) detectors, which are equally spaced out (32°apart) on an arc of a tray driven by a goniometer. Both static and dynamic light scattering (SLS and DLS) data can be collected simultaneously. One of the four detectors have a sample and a reference output, allowing pseudo-cross correlation measurements (single detector mode) thus yielding better data quality in the range of fast decay time $\tau$. The auto- or cross-correlation function is collected by an ALV-7004 digital multiple tau real time correlator, yielding data in the range as short as 25 ns. The scattering angle θ was always set at 90°. In this experiment, the DLS data were obtained from the cross-correlation function using the single detector mode. The ALV software is able to resolve multimodal distribution functions yielding multimodal distributions of hydrodynamic radius through the CONTIN procedure.

Malvern zetasizer has a setted $\lambda$ the wavelength of the radiation (630 nm), and θ the scattering angle at 173°. It can apply $R_H$ and Zeta-potential analyses.

## 2.5 Negative Staining TEM

Transmission electron microscopy (TEM) has been used to display the atomic structure of hard materials broadly.[10] When examining the soft materials such as lipids and proteins, TEM is difficult to obtain the real structures due to the low contrast in images, the radiation damage and sample's dehydration. Negative staining is a straightforward technique to enhance the contrast between the background and the sample on the same TEM grid. The negative stained sample is a thin layer of biological material surrounded and supported by a dried amorphous or frozen-hydrated/vitreous layer of a salt with a heavy metallic element in either the anion or the cation. The negative contrast phenomenon is shown in Figure 2.6. In this way, the enhanced contrast between the specimen and the background allows a better structural identification in TEM.

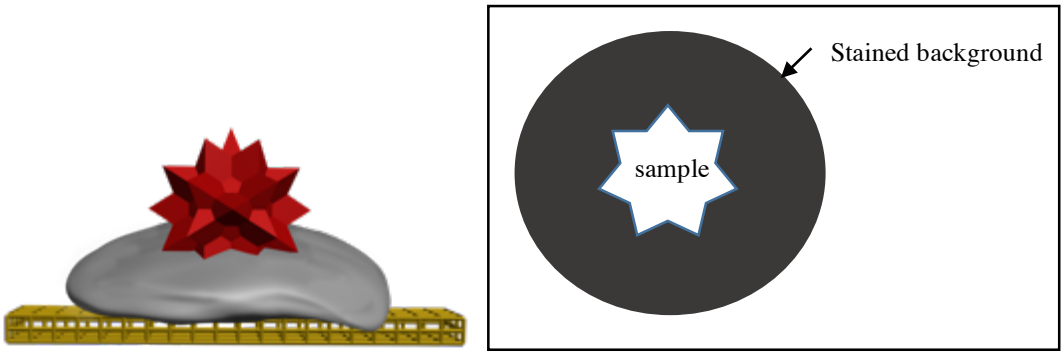


**Figure 2.6** Negative staining TEM sample on copper grid and the obtained image under electron beam

## 2.6 Differential Refractometer

The BI-DNDC differential refractometer made by Brookhaven Instruments Corporation can measure pure solvent and the solution at the same time and responds to the difference in their refractive index at a constant temperature. The wavelength used in this instrument is 620 nm. Solutions of the lipid solution with ten different concentrations were injected in the refractometer in sequence. The differences of refractive index at each concentration to water were collected and fitted by a straight line, the slop of which is the *dn/dc* of measured solution.

## 2.7 Conclusions

This chapter introduces the characterization methods of colloid system. In the next chapters, data from these methods will be the major part as the evidence to conclusions.

## 2.8 References


1. J. Chadwick, Nature **129** (3252), 312 (1932).
2. J. Chadwick, presented at the Proceedings of the Royal Society of London A: Mathematical, Physical and Engineering Sciences, 1932 (unpublished).
3. D. P. Mitchell and P. N. Powers, Physical Review **50** (5), 486 (1936).
4. H. v. H. Jnr and P. Preiswerk, CR Acad. Sci. Paris **203**, 73-75 (1936).
5. J. Hayter and J. Penfold, Colloid and Polymer Science **261** (12), 1022-1030 (1983).
6. S. R. Kline, Journal of applied crystallography **39** (6), 895-900 (2006).
7. L. Feigin, D. I. Svergun and G. W. Taylor, *Structure analysis by small-angle X-ray and neutron scattering*. (Springer, 1987).
8. L. Arleth, B. Ashok, H. Onyuksel, P. Thiyagarajan, J. Jacob and R. P. Hjelm, Langmuir **21** (8), 3279-3290 (2005).
9. J. Li, T. Ngai and C. Wu, Polymer journal **42** (8), 609-625 (2010).
10. D. B. Williams and C. B. Carter, *The Transmission Electron Microscope*. (Springer, 1996).

# Chapter 3

# The effects of temperature, salinity, concentration and PEGylated lipid on the spontaneous nanostructures of bicellar mixtures

## 3.1 Introduction

Nanoparticles (NPs) with polyethylene glycol (PEG) polymers surface coating and/or slightly surface charge can improve their stability by minimizing inter-particle coalescence. Moreover, the PEG coating can reduce the protein adsorption and prevent the RES clearance of the NPs in blood circulation.[1-4] NPs in the size of 10-100 nm can be used as cancer therapeutic candidates for the "enhanced permeability and retention" (EPR) effect in lymph system of tumors.[5] Also, slightly surface charge on the NPs can enhance the tumor tissue penetration out of the circulatory system.[6, 7]

Phospholipid nanodiscs and small unilamellar vesicles (SUVs) form in the charged bicellar system are usually monodisperse and with the diameter under 100 nm. Furthermore, the formation of the bicellar discs and vesicles is a self-assembly process, which is easy to be scaled-up. Phospholipids are biocompatible and the core-shell structures of discs and vesicles are also preferable for better entrapment. These great features make bicellar NPs very promising nanocarriers. However, PEGylated bicellar NPs have not been systematic studied. Therefore, the studies in this chapter is to understand morphological variation of the self-assemblies.

The stability of NPs at physiological temperature (37 °C), dilute conditions, and the relevant salinity is essential for further step applications. In the structurally stable nanodiscs, the long-chain component needs to have the $T_m$ higher than the physiological temperature 37 °C. A suitable candidate is di-$C_{16}$ dipalmitoyl phosphatidylcholine (DPPC), whose $T_m$ is 41 °C. The study of the DPPC/DHPC bicelles, though is not as extensively as of the DMPC/DHPC systems, has already been reported in the literature and increasingly received attention from researchers.[8-19] In this study, a negatively charged di-$C_{16}$ dipalmitoyl phosphatidylglycerol (DPPG) with the same $T_m$ as DPPC was added to the DPPC/DHPC mixture at a constant ratio and expected to stabilize the bicellar nanodiscs at T < $T_m$ by the enhanced electrostatic repulsion.

To achieve PEGylated bicelles, one common type of the PEG-conjugated distearoyl phosphoethanolamine (DSPE-PEG2000) was incorporated in the DPPC/DHPC/DPPG mixtures. The chemical structure of DSPE-PEG2000 is shown in Figure 3.1. The effects of the additional DSPE-PEG on the assembled morphologies at different temperatures, lipid concentrations ($C_{lp}$) and solvent salinities were investigated.

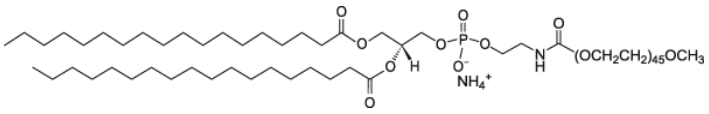


**Figure 3.1** Chemical structure of DSPE-PEG2000

Several goals have been achieved in this study. First, the applicability of the self-assembly principle for the DMPC/DHPC bicellar mixtures has been examined for the DPPC/DHPC mixtures, including the formation of uniform bicellar nanodiscs and SUVs at T < $T_m$ and T > $T_m$, respectively. The reversibility of the disc-to-lamella transition and disc-to-SUVs has been tested following the temperature cycling from T < $T_m$ to T > $T_m$, then back to T < $T_m$. Furthermore, the effects of $C_{lp}$ and salinity (in the presence of Phosphate Buffered Saline, PBS) on the structures have been studied to understand the stability of the bicellar assemblies. Finally, the effect of additional PEGylated lipids on the spontaneous structure in bicellar mixtures has been evaluated. All the detailed morphologies were identified through Small Angle Neutron Scattering (SANS) while the kinetic stability of the bicellar nanodiscs has been examined using dynamic light scattering (DLS).

## 3.2 Materials and Methods

DPPC, DHPC, DPPG and DSPE-PEG2000 were purchased from Avanti Polar Lipids (Alabaster, AL, USA) and used without further purification. Powder of phosphate buffered saline (PBS) was purchased from Sigma-Aldrich (St. Louis, MO). Deuterium oxide (99.9% purity) was purchased from Cambridge Isotope Co. The PBS solution was prepared by dissolving 9.38 gram PBS powder into 1 L $D_2O$ to form a final composition of 137 mM NaCl, 2.7 mM KCl, and 10 mM $Na_2HPO_4$. Two series of samples with identical concentrations were prepared individually in $D_2O$ or PBS solutions. Hydrogenated water ($H_2O$) was used in DLS and Deuterated water

($D_2O$) was in SANS measurements respectively. The compositions of all the samples have been shown in Table 3.1. The mole percentage listed in Table 3.1, corresponding to the DMPC/DHPC/DMPG system in the absence of the DSPE-PEG2000 studied previously. [20-22] Three constant molar ratios are used:

*Q-ratio* = ([DPPC]+[DPPG]+[DSPE-PEG2000])/[DHPC] = 3

*R* = [DPPG]/([DPPC]+[DPPG]+[DSPE-PEG2000]) =0.05

*PEG* = [DSPE-PEG2000]/[Total lipids]

*[lipid] stands for the molar concentration of different components

**Table 3.1** Composition of individual lipids in aqueous solutions (in molar percentage)

| **Lipids** | **NON-PEG Sample** | **Sample with DSPE-PEG2000** |
|---|---|---|
| DPPC | 71.25 | 66.25 |
| DHPC | 25.00 | 25.00 |
| DPPG | 3.75 | 3.75 |
| DSPE-PEG2000 | 0 | 5.00 |

The lipid powders were first weighted and then dispersed into filtered D.I. water (or $D_2O$ for SANS) or PBS solutions (or PBS/$D_2O$ for SANS) to form stock solutions with an initial total lipid concentration of 200.0 mg/mL. After successive vortex and temperature cycling between 25 and 60 °C, the lipid stock solutions were homogenously dissolved in all cases (transparent at room temperature and below). The stock solutions were then progressively diluted at room temperature (~ 25 °C) to the final solutions with in the lipid concentrations of 100, 10 and 1 mg/mL. In this study, the 100 mg/mL is defined as the stock-high-$C_{lp}$, 10 and 1 mg/mL as the high-$C_{lp}$ and low-$C_{lp}$.

## 3.3 Results

In the low-$C_{lp}$ DMPC/DHPC/DMPG without PEGylated lipids, the disc-to-SUV transition usually takes place along with temperature elevation above the $T_m$ of DMPC.[23] To investigate whether the same transition phenomenon can happen in the DPPC/DHPC/DPPG solution and follow the same trend with temperature, SANS measurements were conducted at different temperatures and the data of the sample with a total lipid concentration, $C_{lp}$ of 1 mg/mL. The SANS data with fitting curves are shown in Figure 3.3.1.

The experimental set-up temperature follows an operation sequence: heating up from 20, 37, 50 °C and then cooling down to 10 °C. Thermal equilibrium time periods were at least 30 minutes after the SANS stage reached the targeted temperatures. The first two sets of SANS data at 20 and 37 °C have a common feature that an intensity plateau at the low-$q$ range (0.008 to 0.015 $Å^{-1}$) and a monotonic decay (0.015 to 0.1 $Å^{-1}$) at the high-$q$ range. The PR-Disc model can be used to fit this type of SANS patterns. The fit thickness of the nanodiscs is 48 Å (Table 3.3.1), which is consistent with the DPPC bilayer thickness 48.2 Å in the sub-*gel* phase (below 24.8 °C) and 47.2 Å in the *gel* phase (below 41 °C) as reported by Nagle *et al*.[24] The same SANS patterns trend indicates that the discoid morphology remains at the temperatures below the $T_m$ of DPPC regardless of the pre-transition temperature of pure DPPC bilayer around 23 °C.

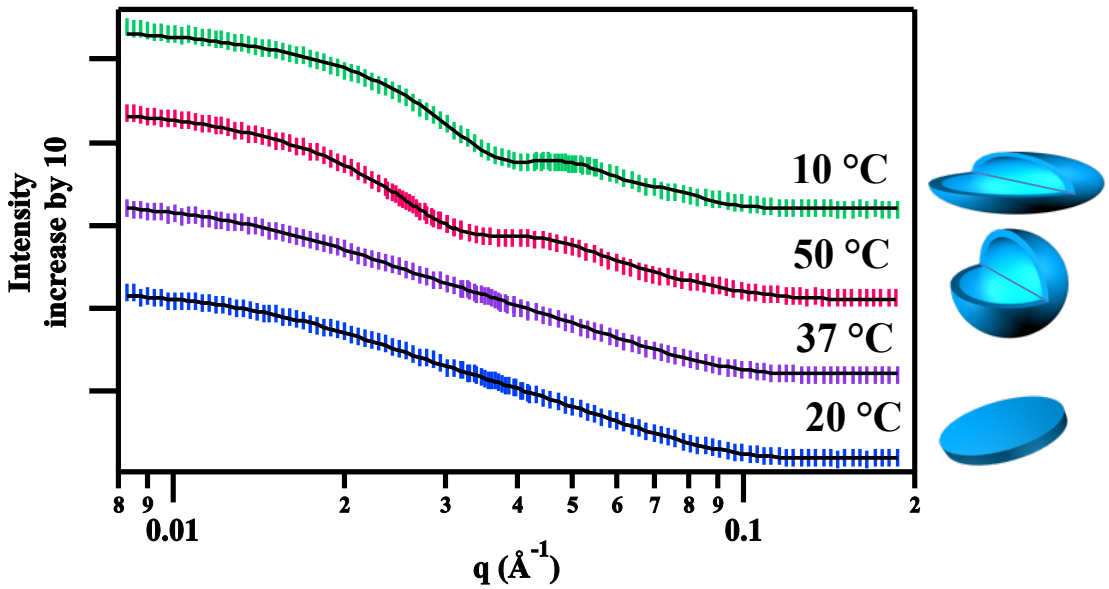


**Figure 3.3.1** The SANS data of 1 mg/mL DPPC/DHPC/DPPG solution at different temperatures following the operation sequence: from 20, 37, 50 to 10°C. The solid curves are the fit results. The used models are PR-Disc for 20 and 37 °C data, PR-ULV for 50 °C, and SS-Oblate for 10 °C. The SANS data are sequenced from bottom to top and rescaled by a factor of 10, 100 and 1000 to enhance the visual clarity.

**Table 3.3.1** Parameters of various models that fit the SANS data of 1 mg/mL DPPC/DHPC/DPPG in $D_2O$ at different temperatures

| T, °C | 20 | 37 | 50 | | 10 | |
|---|---|---|---|---|---|---|
| Fitting Models | *PR-Disc* | *PR-Disc* | *PR-ULV* | | *OSS* | |
| Radius, Å | 123.0 | 134.0 | Inner Radius, Å | 70.0 | Inner Major Axis | 64.0 |
| | | | | | Inner Minor Axis | 35.0 |
| Thickness, Å | 48.0 | 48.0 | Shell Thickness, Å | 38.0 | Outer Major Axis | 126.0 |
| | | | | | Outer Minor Axis | 70.0 |
| Polydispersity | 0.22 | 0.21 | Inner Radius Polydispersity | 0.27 | | |
| Volume, $Å^3$ | 2.3 x $10^6$ | 2.7 x $10^6$ | 3.8 x $10^6$ | | 4.0 x $10^6$ | |

The fitted average radius of the discs increased a little from 123 to 134 Å, when the temperature was increased from 20 to 37 °C. (Table 3.3.1) However, the difference cannot indicate an obvious growth of the discs, since 11 Å is the range of the radii's polydispersities. The possible reason is that the transfer of rim DHPC to DPPC domain

bilayer region happened as their miscibility increased with temperature. The continuous increase of temperature to 50 °C resulted in the expected disc-to-vesicle transition. The 50 °C SANS curve contains broad peaks around $q$ = 0.04 Å$^{-1}$ – a characteristic scattering pattern of monodisperse SUVs – and thus can be fit by the polydisperse single-shell spherical (PR-ULV) model. The best-fitted shell (bilayer) thickness of the vesicles is 38 Å, about 10 Å less than that in the low-temperature cases. The thinner bilayer thickness was presumably due to the melting of the acyl chains, consistent with the previous studies on the lipid bilayer phase transitions.[24, 25] The line tension of the exposed bilayer's hydrophobic edge drove the small bilayer fragments to curve into vesicles.[26, 27]

The formed vesicles did not revert to the disc shape as the temperature dropped to 10 °C below the $T_m$ of DPPC. Instead, the spherical structures were deformed into oblate vesicles according to the fit results with the single-shell oblate (SS-Oblate) model. A similar irreversible process also happened in the DMPC/DHPC/DMPG solution at the low-$C_{lp}$ condition.[28, 29] The fit bilayer shell thickness along the minor axis was 35 Å, less than the spherical shell thickness at 50 °C. While the fit shell thickness along the major axis was greater (> 60 Å), since the DPPC bilayer was supposed to be in the gel phase at 10 °C. The fit results implied that lipid segregation possibly happened in the case of oblate vesicles where DHPC and DPPC preferred to be located the quadrants around the minor and major axes, respectively. The reason for segregations could be the long- and short-chain lipids mismatch, and the packing stress inside the bilayer. Phases segregations or even perforations in bilayers can be found as proposed in the literature.[30]

When the $C_{lp}$ is 10 mg/mL, the structural transition behaved differently from what has been observed in the low-$C_{lp}$ sample as shown in Figure 3.3.2. The sample underwent the same operation sequence, i.e., 20, 37, 50 and 10 °C. All of the SANS curves have a broad peak between the $q$ range from 0.007 to 0.02 $Å^{-1}$, indicating a structure factor caused by the Coulombic interaction, followed by a monotonic decay at the higher $q$ range. Therefore, a discoid model combined with Hayter-Penfold structure factor was applied to fit the SANS data. No evident disc-to-vesicle transition occurred upon the elevation of temperature above the $T_m$ of DPPC. This phenomenon was consistent with a highly charged DMPC/DMPG/DHPC mixture in the former report,[20] presumably due to the strong Coulombic repulsions between discs, and sufficient DHPC stabilizing the rims. The only apparent change in SANS patterns with temperature increasing was the shift of the broad peak toward the lower $q$ range. The possible reason is that the disc coalescence caused a larger spacing between the nanodiscs at 50 °C. The discs' radii also increased from 88 Å to 124 Å as the sample being heated up from 20 to 50 °C (Table 3.3.2). Furthermore, a decrease in thickness (from 47 to 39 Å) followed the gel-to-$L_\alpha$ phase transition of the DPPC bilayer. It should be noted that the disc volume increased from 1,140 to 1,880 $nm^3$ from 20 to 50 °C and then remained practically unchanged from 50 to 10 °C (with a difference less than 10%), indicative of the irreversibility of the nanodisc formation. Nevertheless, the observed disc thickness at 10 °C was consistent with the gel phase DPPC bilayer thickness.

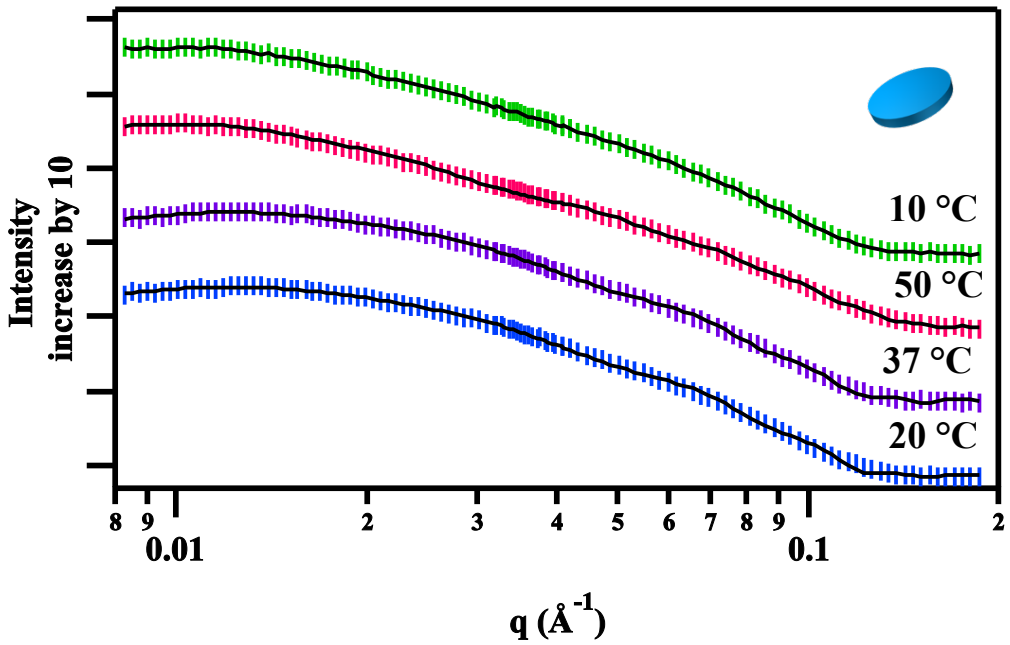


**Figure 3.3.2** The SANS data of 10 mg/mL DPPC/DHPC/DPPG solution at different temperatures following the operation sequence: from 20, 37, 50 to 10 °C. The solid curves are the fitting curves. The intensities in each curve are rescaled by the factors of 1, 10, 100 and 1000 to enhance the visual clarity.

**Table 3.3.2** Parameters of the PR-Disc with Hayter-Penfold structure factor model that fits the SANS data of 10 mg/mL DPPC/DHPC/DPPG in $D_2O$ at different temperatures

| T, °C | 20 | 37 | 50 | 10 |
|---|---|---|---|---|
| Model | *PR-Disc + Hayter-Penfold Structure Factor* | | | |
| Radius, Å | 87.0 | 89.0 | 124.0 | 118.0 |
| Thickness, Å | 47.0 | 46.0 | 39.0 | 46.0 |
| Charge number | 15.1 | 18.2 | 23.0 | 25.0 |
| Volume, $Å^3$ | $1.1 \times 10^6$ | $1.1 \times 10^6$ | $1.9 \times 10^6$ | $2.0 \times 10^6$ |

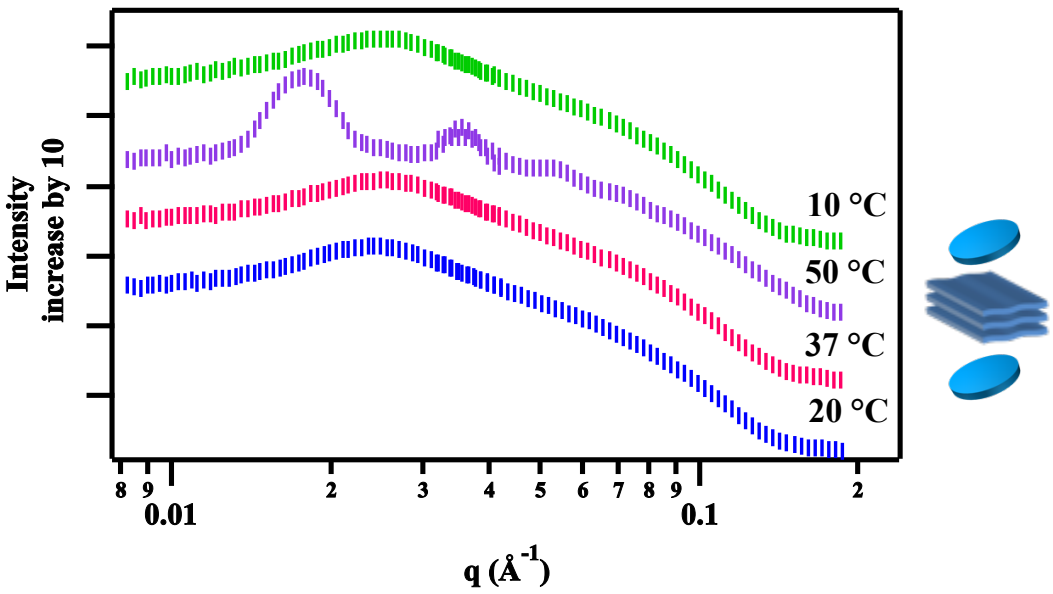


**Figure 3.3.3** The SANS data of 100 mg/mL DPPC/DHPC/DPPG solution at different temperatures following the thermal sequence: from 20, 37, 50 to 10°C. The intensities of each curve are rescaled by the factors 1, 10, 100 and 1000 to enhance the visual clarity.

SANS data of the stock-high-$C_{lp}$ 100 mg/mL solution (Figure 3.3.3) exhibited the similar temperature-dependent morphology transition as the reported DMPC/DMPG/DHPC system.[20] The model of PR-Disc with structure factor was able to fit the scattering patterns at low temperatures (20 and 37 °C), indicative of no temperature-induced disc-growth. The scattering pattern transformed into many high-order quasi-Bragg reflections with more than three peaks at 50 °C ($q$ = 0.018, 0.037 and 0.055 Å$^{-1}$) at 50 °C, representing a lamellar structure with a regular $d$-spacing of 330-350 Å. Unlike the 1.0 and 10 mg/mL samples, the scattering pattern of the 100mg/mL sample fully recovered as the low-T ones after being cooled to 10 °C. The reversibility of the discs validates the temperature cycling in the sample preparation procedures. That is to

say, the concentration of stock solution for further dilution can start from 100 mg/mL DPPC/DHPC/DPPG solutions.

The salinity effect on the self-assemblies was examined through SANS measurements on the 1.0 mg/mL DPPC/DHPC/DPPG samples prepared in PBS/$D_2O$ undergoing the similar thermal path in the sequence from 20, 37, 50 to 10 °C [Figure 3.3.4 (a)]. A significant change in the scattering patterns caused by the additional PBS was found in comparison to those in Figure 3.3.1. The absence of intensity plateau at low-$q$ range indicated the existence of larger particles. Negative staining TEM micrograph of the sample was taken at room temperature (~25 °C) [Figure 3.3.4 (b)] showing polydisperse discs and possibly disrupted vesicles caused by water evaporation. The appearance of large particles was consistent with the upturn SANS intensities at low $q$. The PR-Disc model was used to describe the SANS data of the sample at 20 and 37 °C. As expected, the fit radii can be any value above 300 Å while the fit bilayer thicknesses (between 45 and 48 Å) remained valid.

At 50 °C, a quasi-Bragg peak at $q$ = 0.0085 $Å^{-1}$ appeared, which was corresponding to a $d$-spacing of 73.9 Å. This spacing is typically found in the case of non-swellable lamellar domains, consistent with the multi-lamellar vesicles (MLVs) formation of a previous study on the low-charge or high-salinity DMPC/DHPC/DMPG solutions at high temperatures.[31] The formation of MLVs can be rationalized by the enhanced coalescence between nanodiscs as the PBS salt significantly screens the Columbic repulsion interactions on the bilayer surfaces. When temperature decreased from 50 to 10 °C, the

MLV peak disappears. The 10 °C SANS data can be fit with the PR-Disc model. The best-fit radii are also outside the probing range of the SANS setup, indicating large discoid or/and vesicular morphology). All the best fitting parameters are listed in Table 3.3.3.

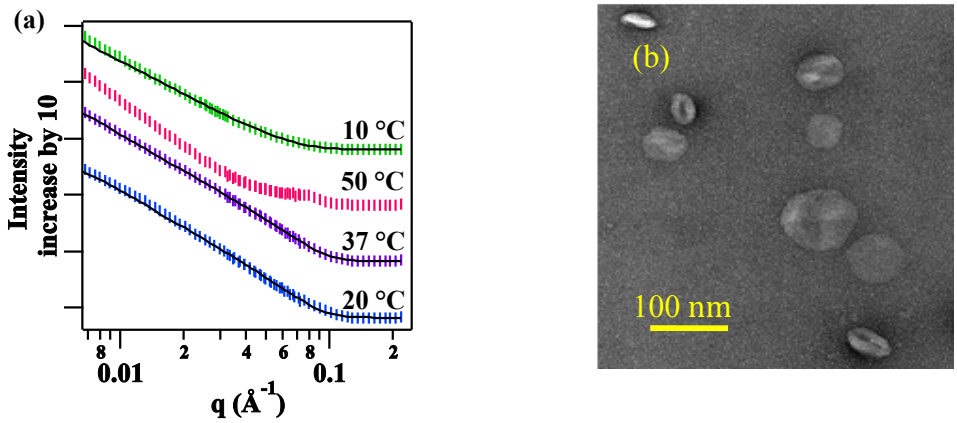


**Figure 3.3.4** (a) The SANS data of 1.0 mg/mL DPPC/DHPC/DPPG in PBS solution at different temperatures following the sequence: from 20, 37, 50 to 10 °C. The solid curves are the fitting curves. The SANS intensities are rescaled by factors of 1, 10, 100 and 1000 to enhance the visual clarity. (b) The TEM micrograph samples at room temperature, where large discs (both top and side views) and possibly ruptured vesicles are observed.

**Table 3.3.3** Parameters of the PR-Disc model that fit the SANS data of 1 mg/mL DPPC/DHPC/DPPG in PBS buffer at different temperatures

| T, °C | 20 | 37 | 50 | 10 |
|---|---|---|---|---|
| Models | *PR-Disc* | *PR-Disc* | *MLV* | *PR-Disc* |
| Radius, Å | > 300 | > 300 | - | > 300 |
| Thickness,Å | 47.2 | 45.2 | - | 47.5 |
| Polydispersity | 0.12 | 0.13 | | 0.10 |

The same experimental procedure was applied to the 10 mg/mL sample in PBS as shown in Figure 3.3.5. The PR-Disc model was used to fit the SANS data at 20 and 37° for their plateau appearances at the low-*q* ranges. The best fitting radii were 95 at 20 °C and 112 Å at 37°C (Table 3.3.4), slightly larger than those in the absence of PBS (Table 3.3.2). At 50 °C, instead of MLVs observed at the 1 mg/mL sample in PBS, a characteristic pattern of ULVs was observed and best fit by the PR-ULV model with an average inner radius of 253 Å and a bilayer thickness of 36.5 Å. The best fitting radius of the 50 °C 10 mg/mL ULV in the presence of PBS was three times larger than that of the ULV formed in the 1 mg/mL sample in the absence of PBS (Table 3.3.1). After the 10 mg/mL sample in PBS was cooled back to 10 °C, the SANS result shows a disk-like curve and the best fit of PR-Disc model yielded > 410 Å and 44 Å for radius and thickness, respectively. The thickness is consistent with the gel phase DPPC bilayer. However, it was difficult to accurately determine the radius of the structures in the solution at 10 °C in the lacking of a low-*q* plateau. A mixture of vesicles and discs may also exist in the 10 °C cool-down sample, indicating by the upturn at the low-*q* range in the SANS curve. At least, the result suggested that the higher $C_{lp}$ would enhance the stability of the discs. It has also observed that the 10 mg/mL discs did not form vesicles even at high temperature in the system in the absence of PBS. (Figure 3.3.2).

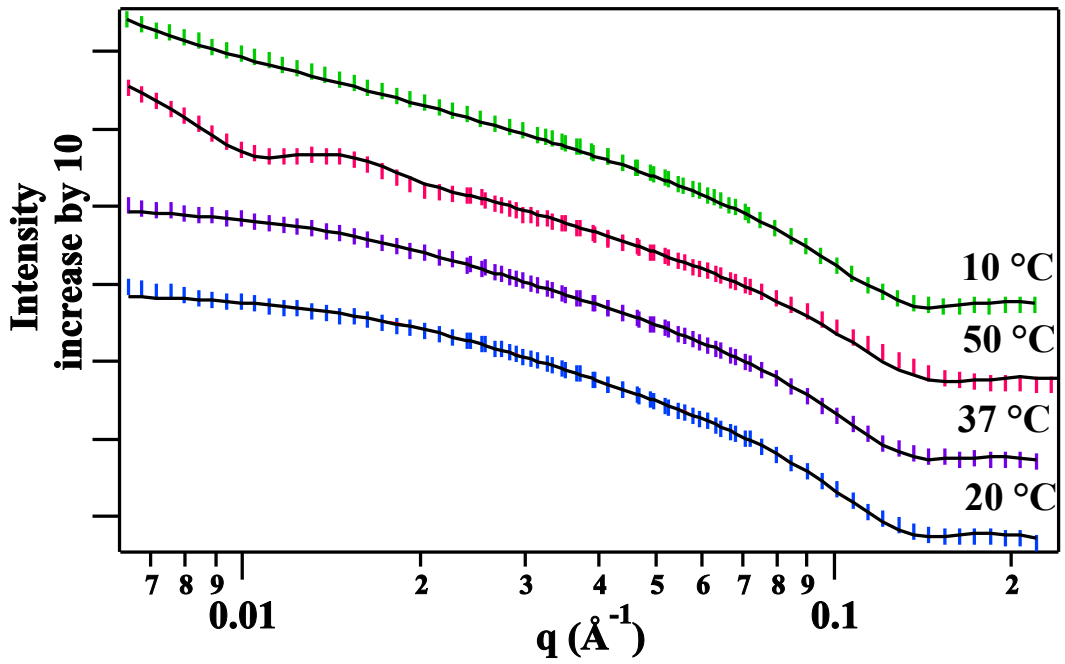


**Figure 3.3.5** The SANS data of 10 mg/mL DPPC/DHPC/DPPG in the PBS solution at different temperatures following the operation sequence: from 20, 37, 50 to 10 °C. The solid curves are the fitting curves. The SANS data are rescaled by the factors of 1, 10, 100 and 1000 to enhance the visual clarity.

**Table 3.3.4** Parameters of the models that fit the SANS data of 10 mg/mL DPPC/DHPC/DPPG sample in PBS buffer at different temperatures

| T, °C | 20 | 37 | 50 | | 10 | |
|---|---|---|---|---|---|---|
| Models | *PR-Disc* | | *PR-ULV* | | *PR-Disc* | |
| Radius, Å | 95 | 112 | Inner Radius, Å | 253 | Radius, Å | 410 |
| Thickness, Å | 46 | 46 | Shell Thickness, Å | 36 | Thickness, Å | 44 |
| Polydispersity | 0.34 | 0.33 | 0.25 | | 0.30 | |
| Volume, Å$^3$ | 1.3 x10$^6$ | 1.8 x10$^6$ | 3.4 x10$^7$ | | 2.3 x10$^7$ | |

It has been reported that PEGylation can effectively reduce the *in vivo* RES uptake of NPs due to the steric effects of the PEG chains thus prolonging the NPs' blood circulation half-life.[32, 33] In this study, 5.0 mole% of DSPE-PEG2000 was incorporated with the

DPPC/DHPC/DPPG mixture. Figure 3.3.6 (a) shows the SANS patterns of a 1.0 mg/mL solution of DPPC/DPPG/DHPC/DSPE-PEG2000 in $D_2O$ experiencing temperature elevation from 10, 37 to 67 °C. All of the SANS patterns showed that the DSPE-PEG2000 containing sample remained the discoid morphology throughout the studied temperatures. The PR-Disc model was the chosen fitting model. The absence of disc-to-vesicle transition with temperature increasing indicated high structural stability of the nanodiscs. A negatively stained TEM image of the 0.01 mg/mL sample taken at 25 °C (Figure 3.3.6 (b)) further confirmed the discoid morphology. The radii of discs from SANS best fitting increased slightly from 76 to 92 Å as temperature increases from 10 to 67 °C (Table 3.3.5). It should be noted that this set of SANS data was collected at a different instrument, CG3-BioSANS (at High Flux Isotope Reactor), which had a different instrument resolution that might affect the fitting results. The instrumentation difference could partially explain the apparent increase in disc thickness (70 Å) at the low-T range compared to that in the absence of DSPE-PEG2000 (48 Å in Table 3.1). However, it was also possible that the PEG chains of DSPE-PEG2000 in the bilayer planar region extended toward the water phase and increased the bilayer thickness accordingly. A coarse-grain molecular dynamic simulation suggested that PEGylated lipids preferred to locate at the disc rim in a similar system in the absence of DHPC due to the high curvature attributed to the large PEG headgroups.[16] In this study, the immiscibility between DHPC in the $L_\alpha$ phase and DPPC in the gel phase should be the major reason for the formation of DHPC-coated discs. As the temperature increased to 67

°C, the disc thickness decreased to 60 Å (Table 3.3.5), possibly due to the combinational effects of the gel-to-$L_\alpha$ phase transition and the collapse of the PEG chains at a high temperature caused by the disruption of hydrogen bonds.[34]

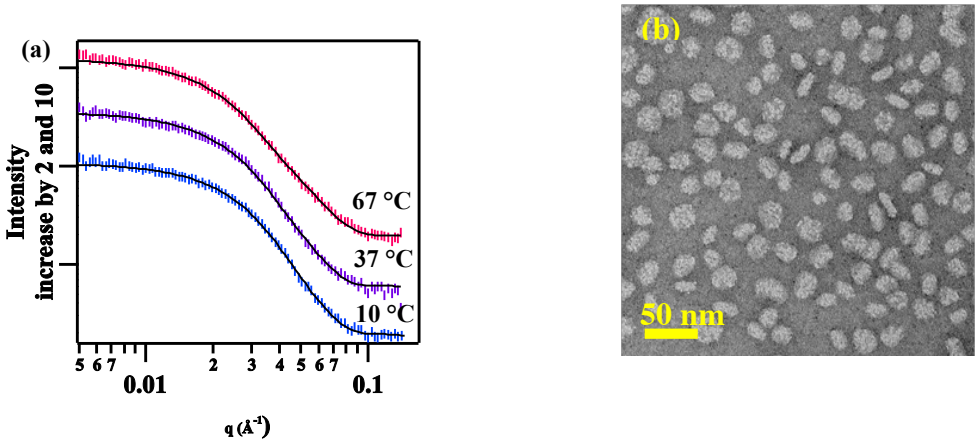


**Figure 3.3.6** (a) The SANS data of 1 mg/mL DPPC/DHPC/DPPG/DSPE-PEG2000 in $D_2O$ at different temperatures following the operation sequence: from 10, 37 to 67°C, the solid curves are the PR-Disc fitting curves. The SANS data are rescaled by factors of 1, 2 and 10 to enhance the visual clarity. (b) The negative staining TEM micrograph is obtained from the sample of a concentration of 0.01 mg/mL

**Table 3.3.5** Parameters of the PR-Disc model that fits the SANS data of 1 mg/ml DPPC/DHPC/DPPG/DSPE-PEG2000in $D_2O$ at different temperatures

| T, °C | 10 | 37 | 67 |
|---|---|---|---|
| Model | | *PR-Disc* | |
| Radius, Å | 76.0 | 83.0 | 92.0 |
| Thickness, Å | 70.0 | 70.0 | 60.0 |
| Polydispersity | 0.2 | 0.2 | 0.2 |
| Volume, $Å^3$ | $1.3x10^6$ | $1.5x10^6$ | $1.6x10^6$ |

To investigate the $C_{lp}$ effect on the assembled morphology in the presence of DSPE-PEG2000, the SANS data of 10 mg/ml mixture containing DSPE-PEG2000 in $D_2O$ undergoing a thermal sequence from 10, 37 to 67 °C were conducted (Figure 3.3.7). All of the SANS curves have the characteristic feature described by the PR-Disc with Hayter-Penfold structure factor model, consistent with 10 mg/mL sample in the absence of DSPE-PEG2000 in Figure 3.3.2. As the DPPC underwent the phase transition from gel (10 °C) to $L_\alpha$ phase (67 °C), the best fitting radii of the discs slightly increased from 75 to 90 Å and the thicknesses of the discs decreased from 50 to 39 Å (Table 3.3.6). However, the volume of the discs remained practically the same or slightly increased (within 10%) in contrast to the 70-80% volume increase upon the elevation of temperature for the mixtures in the absence of DSPE-PEG2000 (Table 3.3.4). The discs can keep their morphology at different temperatures could be explained by the fact that the addition of DSPE-PEG2000 effectively inhibited the coalescence between discs. The radii of the nanodiscs were found to be smaller than those at the corresponding temperature in the absence of DSPE-PEG2000 (Table 3.3.4).

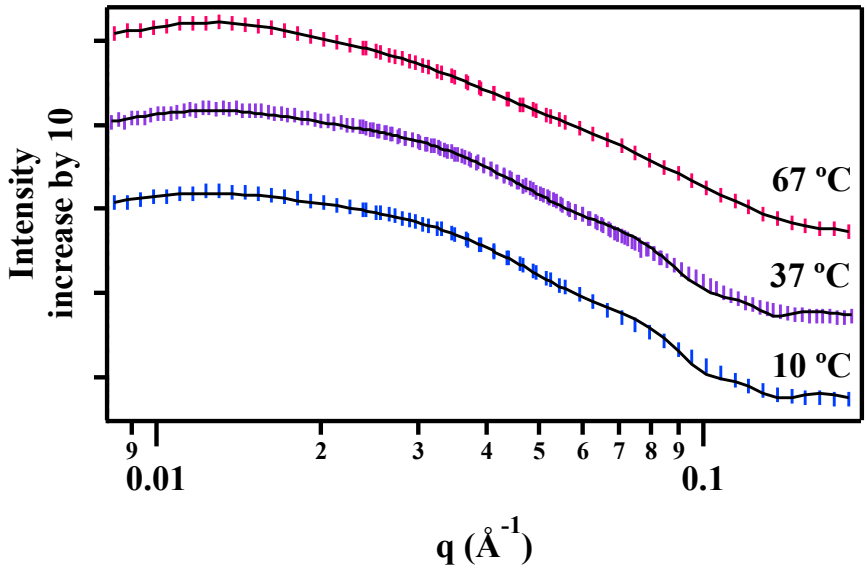


**Figure 3.3.7** The SANS data of 10 mg/mL DPPC/DHPC/DPPG/DSPE-PEG2000 in $D_2O$ at different temperatures following the operation sequence: from 10, 37 to 67°C. The solid curves are the fitting curves. The SANS data are rescaled by a factor (from 1 to 100) to enhance the visual clarity.

**Table 3.3.6** Parameters of the PR-Disc model combined with the Hayter-Penfold structure factor that fits the SANS data of 10 mg/ml DPPC/DHPC/DPPG/DSPE-PEG2000 in $D_2O$ at different temperatures

| T, °C | 10 | 37 | 67 |
|---|---|---|---|
| Models | PR-Disc + Hayter-Penfold Structure Factor | | |
| Radius, Å | 75.0 | 76.0 | 90.0 |
| Thickness, Å | 50.0 | 50.0 | 39.0 |
| Volume, $Å^3$ | $8.8x10^5$ | $9.1x10^5$ | $9.9x10^5$ |

The stability of the nanodiscs in the presence of DSPE-PEG2000 was also investigated in the presence of PBS. The 1.0 mg/mL DPPC/DHPC/DPPG/DSPE-PEG2000 in PBS underwent the thermal path in the sequence of 20, 37, 50 and 10 °C. The SANS data at 20 and 37 °C (Figure 3.3.8) are similar to each other and can be fit with the PR-Disc model (Table 3.3.7). The radii of

the nanodiscs were larger than of those in water (Table 3.3.6) at the corresponding temperatures, indicating that PBS effectively promoted the coalescence among discs by screening the inter-particle Coulombic repulsion interactions. Nevertheless, the DSPE-PEG2000 showed a significant enhancement in the stability of the nanodiscs, when compared with the counterpart in the absence of DSPE-PEG2000at the corresponding temperatures (Figure 3.3.4), where the mixture of large discs and vesicles were observed. Several oscillations are found in the 50 °C scattering pattern, which can be fit by the single-shell oblate (SS-Oblate) model. Oblate vesicles with a smaller radius and a similar shell volume still existed as the temperature dropped to 10 °C, indicating little change in the assembled morphologies and the aggregation number in the solution. Oblate vesicles were also found in a previous low-$C_{lp}$ DMPC/DHPC/DMPG system.[29]

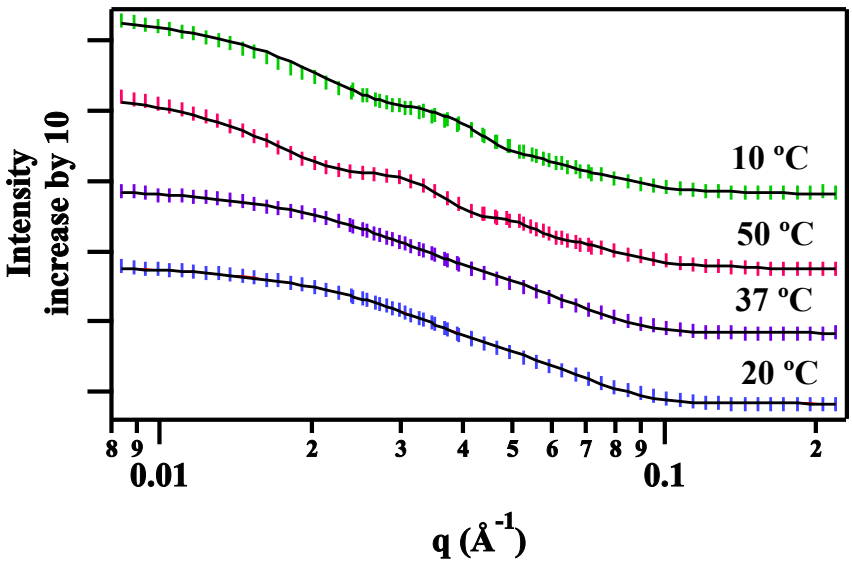


**Figure 3.3.8**. The SANS data of 1.0 mg/mL DPPC/DHPC/DPPG/DSPE-PEG2000in the PBS buffer at different temperatures following the following operation sequence: from 20, 37, 50 and back to 10 °C. The solid curves are the fitting curves. The SANS data are rescaled by factors of 1, 10, 100 and 1000 for a better visual clarity.

**Table 3.3.7** Parameters of PR-Disc and SS-Oblate models that fit the SANS data of 1 mg/mL DPPC/DHPC/DPPG/DSPE-PEG2000 in PBS at different temperatures.

| T, °C | 20 | 37 | | 50 | 10 |
|---|---|---|---|---|---|
| Models | PR-Disc | | SS-Oblate | | |
| Radius, Å | 96 | 105 | Major core semi-axis, Å | 123 | 90 |
| | | | Minor core semi-axis, Å | 46 | 37 |
| Thickness, Å | 54 | 54 | Major shell semi-axis, Å | 192 | 171 |
| | | | Minor shell semi-axis, Å | 60 | 59 |
| Polydispersity | 0.15 | 0.16 | | - | - |
| Volume, $Å^3$ | $1.56x10^6$ | $1.9x10^6$ | | $6.3x10^6$ | $6.0x10^6$ |

Quantitative analysis of the best fitting parameters obtained provided further insight into the system. First, the temperature-induced increase in disc radius is similar to all the aforementioned studies. In regard to the oblate vesicles at 50 °C, a substantially thinner shell thickness along the minor than the major axis was observed (14 Å versus 69 Å). The non-uniform thickness suggests that the long-chain DPPC and DSPE-PEG2000 might not locate themselves on the quadrants along the minor axis. It is even possible that holes, whose edge was stabilized by DHPC, might form along the minor axis as described in the literature.[35] The oblate vesicles from 50 to 10 °C yield a thicker bilayer along both the minor (22 Å) and the major axes (81 Å), possibly due to the gel phase bilayer and the extension of the PEG chains in the low-temperature range.

Regarding the sample at $C_{lp}$ = 10 mg/mL in the presence of DSPE-PEG2000 and PBS, nanodiscs were found at low temperatures (10 and 37 °C) as anticipated (Figure 3.3.9). The radii and thicknesses from the PR-Disc model are similar to those in the low-

$C_{lp}$ samples at the corresponding temperature. At 67 °C, the PR-ULV model was used to fit the SANS data yielding a good agreement, indicative of the formation of spherical vesicles. The spherical structure in the 10 mg/mL sample suggests a more homogeneous distribution of the species on the bilayer shell. Two possibilities are likely attributed to the homogeneity: (1) the temperature of the 10 mg/mL sample (67 °C) was higher than that of the 1 mg/mL low-$C_{lp}$ sample (50 °C), (2) more DHPC associated with bilayer based on the assumption of a constant DHPC concentration in solution enhancing the homogeneity. The best fitting parameters of all the models used are illustrated in Table 3.3.8.

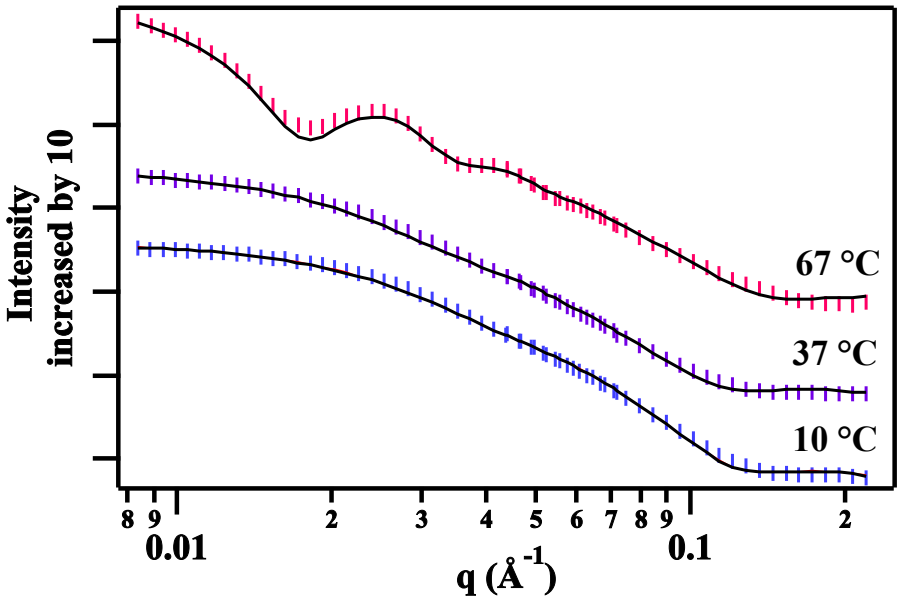


**Figure 3.3.9** The SANS data of 10 mg/mL DPPC/DHPC/DPPG/DSPE-PEG2000 in PBS buffer at different temperatures following the operation sequence: from 10, 37 to 67 °C. The solid curves are the fitting curves. The SANS data are rescaled by a factor (from 1 to 100) for better visual clarity.

| **Table 3.3.8** Parameters of PR-Disc and PR-ULV models that fit the SANS data of 10 mg/mL DPPC/DHPC/DPPG/DSPE-PEG2000 in PBS buffer at different temperatures | | | | |
|---|---|---|---|---|
| T, °C | 10 | 37 | 67 | |
| **Models** | PR-Disc | | PR-ULV | |
| **Radius, Å** | 93.6 | 115.7 | Inner Radius, Å | 149.8 |
| **Thickness, Å** | 48.5 | 49.8 | Thickness, Å | 38.9 |
| **Polydispersity** | 0.17 | 0.15 | Polydispersity | 0.17 |
| **Volume, Å$^3$** | 1.3 x $10^6$ | 2.1 x $10^6$ | Volume, Å$^3$ | 1.4 x $10^7$ |

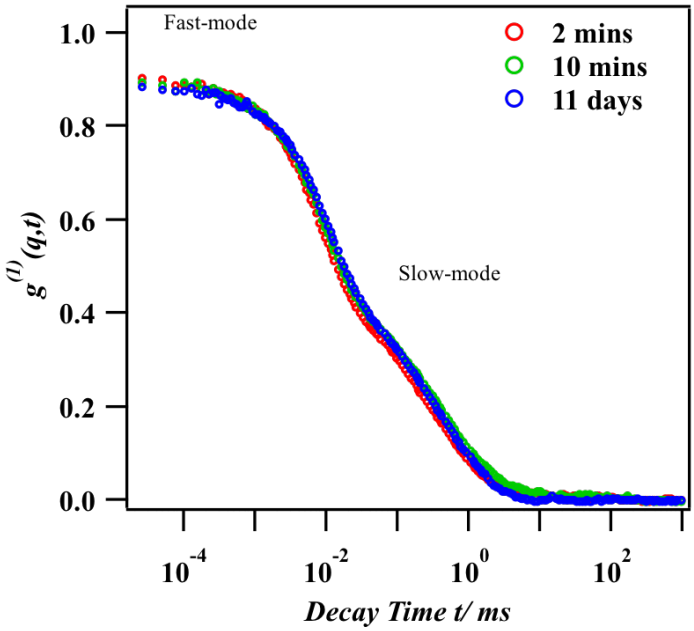


**Figure 3.3.10** The auto correlation functions of 10 mg/mL DPPC/DHPC/DPPG in D.I. water at T = 25 °C and the recording time at 2 minutes (red), 10 minutes (green) and 11 days (blue) after dilution from 200 mg/mL concentrated solution.

The stability of nanodiscs was investigated by time-dependent DLS. Figure 3.3.10 shows the autocorrelation function curves of the 10.0 mg/mL DPPC/DHPC/DPPG in $H_2O$ at different time periods after its dilution from 200 mg/mL. Since the electrostatic interactions among the charged particles are overwhelming, the hydrodynamic radius $R_H$ values did not reflect the actual sizes of nanoparticles in this case. The fast- and slow-relaxation modes coexist at all of the three curves

at 2 and 10 minutes and 11 days after the initial dilution. Little shifts in decay time were observed in these curves, indicating the size of the objectives and the inter-particle interactions remain mostly invariant over the measured time.

The kinetics of 1 mg/mL DPPC/DPPG/DHPC mixture in PBS buffers in the presence and absence of 5 mole% DSPE-PEG2000were tested by DLS (Figure 3.3.11). In the presence of DSPE-PEG2000 system, both of the auto correlation functions at 5 minutes and 5 days after dilution were identical [Figure 3.3.11 (a)]. While the auto correlation functions of the solution in the absence of DSPE-PEG2000 varied even within the first 75 minutes after dilution [Figure 3.3.11(b)]. The $R_H$ distributions shown in Figure 3.3.11(c) are corresponding to the auto correlation functions in Figure 3.3.11(a). In 5 minutes after dilution from 200 to 1 mg/mL in PBS, the $R_H$ distribution of DPPC/DHPC/DPPG/DSPE-PEG2000 system showed a peak around 10 nm. The $R_H$ value is correlated to the SANS data of the same system at 10 and 37 °C (Table 3.3.8). After 5 days, the majority of the $R_H$ value was still around 10 nm, while only a small population in hundreds nanometer scale appeared in the $R_H$, possibly caused by the coalescence between discs. The $R_H$ distributions in Figure 3.3.4 (d) are corresponding to the auto correlation functions in Figure 3.3.4(b) of the 1 mg/mL DPPC/DHPC/DPPG in PBS. The major $R_H$ distribution peak still locates around 10 nm at 5 minutes after dilution. Large particles quickly developed after dilution in 70 minutes, which was consistent with the TEM micrograph [Figure 3.3.4 (b)]. The DLS, SANS and TEM results indicate 5 mole% of DSPE-PEG2000 can stabilize the nanodisc system in the presence of PBS buffer.

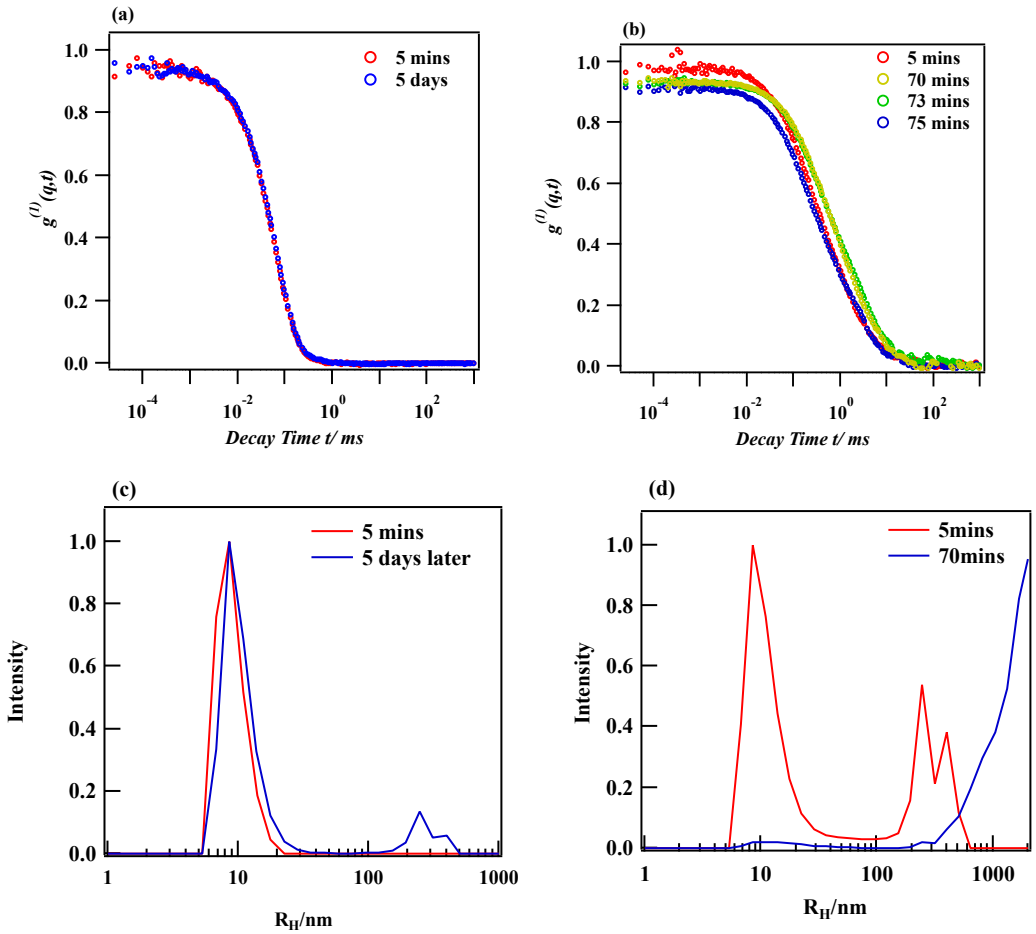


**Figure 3.3.11** The auto correlation functions of (a) 1 mg/mL DPPC/DHPC/DPPG/DSPE-PEG2000 in PBS and (b) 1 mg/mL DPPC/DHPC/DPPG in PBS at 25 °C at different time periods after dilution from 200 mg/mL concentrated solutions. Hydrodynamic radii distributions measured by DLS: (c) DPPC/DHPC/DPPG/DSPE-PEG2000in PBS and (d) DPPC/DHPC/DPPG in PBS solutions. The labeled times are how long the samples have been diluted from 200 mg/mL to 1mg/mL:5 minutes and 5 days in (c);5 and 70 minutes in (d).

## 3.4 Discussion

### 3.4.1 The Effect of Temperature

The spontaneously formed structures of DPPC/DHPC/DPPG mixture in aqueous solutions as a function of temperature and lipid concentration behaved similarly to those of the DMPC/DHPC/DMPG in literature,[27] where the disc-to-vesicle transition temperature was found closely correlating with the $T_m$ of the long-chain lipids. Phase segregation existed in the

DPPC/DHPC/DPPG solution below 41 °C the $T_m$ of DPPC, since the long-chain DPPC, DPPG were in the gel phase while the short-chain DHPC was in the $L_\alpha$ phase. The immiscibility led to the formation of the planar bilayer and the rim of the discs, respectively. As the temperature increased above the $T_m$, DPPC melted into the $L_\alpha$ phase and became more miscible with DHPC, promoting the migration of rim DHPC to the planar region, consequently resulting in the exposure of hydrophobic chains at the rim part. The lack of rim DHPC prompted the bilayer fragments' coalescence and close-up into small unilamellar vesicles (SUVs).[27] The disc-to-vesicle transition is depicted in figure 3.3.11 (a), (b) and (d) in all the low-$C_{lp}$ and some high-$C_{lp}$ samples. The transition has also been reported in DMPC-containing systems in the literature.[36, 37] An early study on a melittin/DPPC system using DLS and TEM characterizations also showed a disc-to-vesicle transition as temperature went across the $T_m$ of DPPC, suggesting that melittin may play a similar role as the short-chain lipid.[38] The current system confirmed the universality of such transformation with different lipids or peptides.

### 3.4.2 The Effect of Lipid Concentration

In regards to samples at different lipid concentrations $C_{lp}$ (i.e., comparing 1.0 mg/mL with 10 mg/mL samples), three significant observations on the effects of high $C_{lp}$ (10 mg/mL) are also summarized in Figure 3.4.1. First, the high-$C_{lp}$ 10 mg/mL samples remained stable discoid structures at the high temperature (50 °C) as shown in Figure 3.3.1 and 3.3.2 [also Figure 3.4.1(a)] at the molar ratios of Q=3 R=0.05. PBS has less effect on the MLV formation for higher $C_{lp}$ samples [Figure 3.3.4, 3.3.5 and 3.3.11(b)]. (3) The high-$C_{lp}$ promoted the formation of

spherical vesicles instead of oblate vesicles in the presence of PBS and DSPE-PEG2000 as shown in Figure 3.3.8, 3.3.9 and 3.3.11(d).

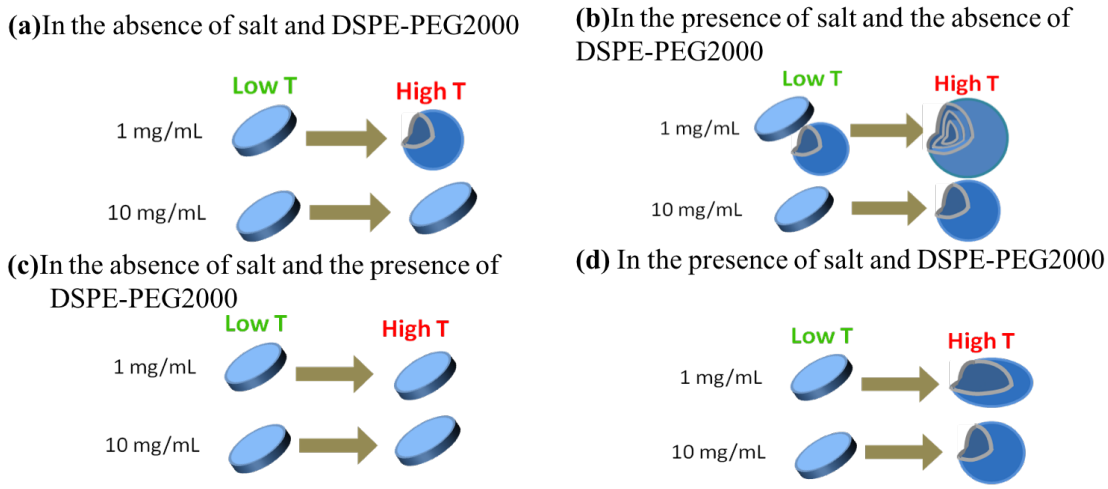


**Figure 3.4.1** Temperature-triggered structural transformation in the cases of $C_{lp}$ = 1 mg/mL and 10 mg/mL: (a) in the absence of PBS salt and DSPE-PEG2000, (b) in the presence of PBS salt but in the absence of DSPE-PEG2000, (c) in the absence of PBS salt but in the presence of DSPE-PEG2000 and (d) in the presence of PBS salt and DSPE-PEG2000

The amount of free DHPC molecules in solutions can rationalize partial of the above-mentioned observations. Since the compositions of the lipids remained the same in the samples of the two different lipid concentrations in the series, the sample dilution should have exerted no effect on the composition change but only increased the inter-particle spacing. Nevertheless, it should be noted that the critical micelle concentration (CMC) of pure DHPC is 15 mM, which is about $3x10^7$ times higher than that of DPPC (i.e., 0.46 nM).[39] Dilution effectively reduced the concentrations of the free lipids in solution and consequently perturbed their pseudo-equilibrium between the assembled lipids and the free

ones. The mismatched solubility of different lipids resulted in different degrees of perturbation in the pseudo-equilibrium states. As a result, the highly soluble lipids (DHPC in this case) would be "pulled" out of the assemblies upon dilution, leading to a significant variation in the lipid compositions of the NPs. Since DHPC adapted to a high-curvature environment, serving as the "edge stabilizer" for the nanodiscs, the insufficiency of DHPC molecules, therefore, promoted the coalescence between nanodiscs and the disc-to-vesicle transition, consistent with the first observation.

The same reason can be used on the structural variation of the samples at low temperature in the presence of PBS. Since the total edge surface area of the larger discoid structures is less than the smaller ones in the condition of the same volumes, the low-$C_{lp}$ large discs should require less DHPC to be stable than the high-$C_{lp}$ small ones. At the high temperature, the rate of the structural transition (nanodisc-to-vesicle) is also slower if sufficient DHPC can associate with the assemblies in the high-$C_{lp}$ samples. It has also been reported that slower structural transition favored ULVs over MLVs formation.[31] This explains why the high-$C_{lp}$ ULVs and low-$C_{lp}$ MLVs were found in Figure 3.4.1(b). Finally, the increase amount of DHPC softened the bilayer, leading to more flexible and homogenously distributed membranes, which preferred to adopt a spherical vesicle than an oblate shape to minimize the surface tension. This was also consistent with the observation in Figure 3.4.1(d).

### 3.4.3 The Effect of Salt

The effect of salt on the morphology of the lipid mixtures has been reported elsewhere.[26] The influence mainly came from the screening of the Coulombic interactions between particles. In fact, the coalescence could be described by the Smoluchowski population model combined with the DLVO theory.[40] The current study showed that the presence of PBS effectively induced the formation of large discs, unilamellar and multilamellar vesicles [Figure 3.3.4, 3.4.1(b)], possibly because of the fast coalescence consistent the previous report.[31]

### 3.4.4 The Effect of DSPE-PEG2000

One of the major themes in this report is to understand the effect of DSPE-PEG2000 on the lipid-assembled structures, thus a better control of the nanodiscs or vesicles can be achievable. The result showed that the addition of 5 mole% of DSPE-PEG2000 did not disrupt the formation of bicellar nanodiscs. Instead, the addition of DSPE-PEG2000 further stabilized the nanodiscs in all the studied cases, consistent with the report in the literature.[41] Figure 3.3.1 and 3.3.6 provided the insights into the effects of DSPE-PEG2000 on improving the stability of nanodiscs [also in Figure 3.4.1(c)]. The results showed that nanodiscs were stable with DSPE-PEG2000 even at temperatures above the $T_m$ of DPPC, i.e., DPPC in the $L_\alpha$ phase. It should be noted that all the samples had been equilibrating at the temperature for more than 30 minutes before the SANS measurements. Nevertheless, it does not imply that if the structures obtained from the SANS data are thermodynamically stable. Figure 3.3.11 showed the DLS data of the DPPC/DPPG/DHPC and

DPPC/DPPG/DHPC/DSPE-PEG2000 mixtures in PBS buffer at room temperature, small NPs (presumably nanodiscs) were initially found in both solutions. After 70 minutes large particles overwhelmed in the DPPC/DPPG/DHPC mixtures consistent with the TEM micrograph [Figure 3.3.4 (b)], while the NPs remained stable for 5 days in the DPPC/DPPG/DHPC/DSPE-PEG2000 solution with only small amount of larger aggregates. It should be noted that since the distribution functions obtained in DLS are mass-weighted, the small number of large aggregates in Figure 3.3.11 (d) should not affect the fitting results to the SANS data.

Another noteworthy effect of the additional DSPE-PEG2000 on the bicelle system is that it counteracts with the effect of PBS. The comparison between Figure 3.3.4 and 3.3.8 indicates that the addition of DSPE-PEG2000 effectively inhibited the formation of MLVs. As mentioned previously, this was possibly due to the steric interaction of the PEG chains that slow the coalescence and folding up processes of the nanodiscs, leading to the SUV structure.

## 3.5 Conclusion

Uniform bicellar nanodiscs can be obtained in aqueous solutions of DPPC/DPPG/DHPC and of DPPC/DPPG/DHPC/DSPE-PEG2000 through self-assembly. These bicellar nanodiscs can serve as the precursors for uniform small unilamellar vesicles. SANS, DLS and TEM were applied to probe the sizes and morphologies of the assemblies in the mixtures as functions of $C_{lp}$, temperature, in the presence and absence of PBS and DSPE-PEG2000. It is clearly shown that the DPPC/DHPC/DPPG discs and SUVs can self-assemble at low-T and high-T (temperatures below and above the $T_m$ of DPPC), respectively, similar as previously reported DMPC/DHPC/DMPG system.[20] The high-$C_{lp}$ samples allow more DHPC to associate with the assemblies and consequently stabilize the nanodisc rim. PBS screens the electrostatic interactions between particles and thus promotes the coalescence of the nanodiscs, leading to the formation of polydisperse large discs, vesicles and the mixture of the two. The DPPC/DHPC/DPPG nanodiscs are reasonably stable in water at low temperature. In PBS, the nanodiscs exhibit low stability as forming large discs and vesicles. The DSPE-PEG2000 is able to stabilize the nanodiscs and inhibit the formation of MLVs at high temperature. This is possibly attributed to the steric effect caused by the PEG chains, inhibiting or slowing down the coalescence kinetics. To the best of our knowledge, this study presents one of the first attempts to understand the effect of DSPE-PEG2000 on the self-assembled bicellar nanodiscs. This knowledge can provide the strategy of developing low RES-uptake PEGylated stealth nanodiscs.

## 3.6 References


1. J. Kreuter, *Colloidal drug delivery systems*. (CRC Press, 1994).
2. A. L. Klibanov, K. Maruyama, V. P. Torchilin and L. Huang, FEBS Letters **268** (1), 235-237 (1990).
3. R. Gref, M. Lück, P. Quellec, M. Marchand, E. Dellacherie, S. Harnisch, T. Blunk and R. Müller, Colloids and Surfaces B: Biointerfaces **18** (3), 301-313 (2000).
4. J. N. Israelachvili, *Intermolecular and surface forces: revised third edition*. (Academic press, 2011).
5. Y. Matsumura and H. Maeda, Cancer research **46** (12 Part 1), 6387-6392 (1986).
6. T. Nomura, N. Koreeda, F. Yamashita, Y. Takakura and M. Hashida, Pharmaceutical Research **15** (1), 128-132.
7. S. Hu-Lieskovan, J. D. Heidel, D. W. Bartlett, M. E. Davis and T. J. Triche, Cancer research **65** (19), 8984-8992 (2005).
8. L. Barbosa-Barros, A. De La Maza, J. Estelrich, A. M. Linares, M. Feliz, P. Walther, R. Pons and O. López, Langmuir **24** (11), 5700-5706 (2008).
9. L. Barbosa-Barros, G. Rodríguez, C. Barba, M. Cócera, L. Rubio, J. Estelrich, C. López-Iglesias, A. De La Maza and O. López, Small **8** (6), 807-818 (2012).
10. J. A. Whiles, K. J. Glover, R. R. Vold and E. A. Komives, Journal of Magnetic Resonance **158** (1-2), 149-156 (2002).
11. J. Lind, J. Nordin and L. Mäler, Biochimica et Biophysica Acta - Biomembranes **1778** (11), 2526-2534 (2008).
12. P. W. Yang, T. L. Lin, Y. Hu and U. S. Jeng, Chinese Journal of Physics **50** (2), 349-356 (2012).
13. L. Rubio, C. Alonso, G. Rodríguez, M. Cócera, L. Barbosa-Barros, L. Coderch, A. de la Maza, J. Parra and O. López, European Journal of Pharmaceutics and Biopharmaceutics **86** (2), 212-218 (2014).
14. J. K. Claridge, J. Aittoniemi, D. M. Cooper and J. R. Schnell, Biochemistry **52** (47), 8420-8429 (2013).
15. W. Shinoda, R. Devane and M. L. Klein, Journal of Physical Chemistry B **114** (20), 6836-6849 (2010).
16. H. Lee and R. W. Pastor, Journal of Physical Chemistry B **115** (24), 7830-7837 (2011).
17. S. Wang and R. G. Larson, Soft Matter **9** (2), 480-486 (2013).
18. R. Vácha and D. Frenkel, Langmuir **30** (15), 4229-4235 (2014).
19. Y. Jiang, H. Wang and J. T. Kindt, Biophysical Journal **98** (12), 2895-2903 (2010).
20. M. P. Nieh, C. J. Glinka, S. Krueger, R. Scott Prosser and J. Katsaras, Biophysical Journal **82** (5), 2487-2498 (2002).
21. R. Soong, M. P. Nieh, E. Nicholson, J. Katsaras and P. M. MacDonald, Langmuir **26** (4), 2630-2638 (2010).
22. M. P. Nieh, V. A. Raghunathan, G. Pabst, T. Harroun, K. Nagashima, H. Morales, J. Katsaras and P. MacDonald, Langmuir **27** (8), 4838-4847 (2011).

23. C. R. Sanders and G. C. Landis, Biochemistry **34** (12), 4030-4040 (1995).
24. J. F. Nagle and M. C. Wiener, Biochimica et Biophysica Acta (BBA) - Biomembranes **942** (1), 1-10 (1988).
25. N. Kučerka, M.-P. Nieh and J. Katsaras, Biochimica et Biophysica Acta (BBA) - Biomembranes **1808** (11), 2761-2771 (2011).
26. S. Mahabir, D. Small, M. Li, W. Wan, N. Kučerka, K. Littrell, J. Katsaras and M. P. Nieh, Biochimica et Biophysica Acta - Biomembranes **1828** (3), 1025-1035 (2013).
27. M.-P. Nieh, N. Kučerka and J. Katsaras, Methods in enzymology **465**, 3-20 (2009).
28. M.-P. Nieh, T. Harroun, V. Raghunathan, C. Glinka and J. Katsaras, Physical review letters **91** (15), 158105 (2003).
29. M. P. Nieh, V. A. Raghunathan, S. R. Kline, T. A. Harroun, C. Y. Huang, J. Pencer and J. Katsaras, Langmuir **21** (15), 6656-6661 (2005).
30. Y. Sakuma, N. Urakami, T. Taniguchi and M. Imai, Journal of Physics: Condensed Matter **23** (28), 284104 (2011).
31. M.-P. Nieh, P. Dolinar, N. Kučerka, S. R. Kline, L. M. Debeer-Schmitt, K. C. Littrell and J. Katsaras, Langmuir **27** (23), 14308-14316 (2011).
32. S. Zalipsky, Advanced Drug Delivery Reviews **16** (2), 157-182 (1995).
33. A. Gabizon and F. Martin, Drugs **54** (4), 15-21 (1997).
34. O. Garbuzenko, Y. Barenholz and A. Priev, Chemistry and physics of lipids **135** (2), 117-129 (2005).
35. N. L. Yamada, Langmuir **28** (50), 17381-17388 (2012).
36. P. Lesieur, M. Kiselev, L. Barsukov and D. Lombardo, Journal of applied crystallography **33** (3), 623-627 (2000).
37. J. Leng, S. U. Egelhaaf and M. E. Cates, Biophysical journal **85** (3), 1624-1646 (2003).
38. E. J. Dufourc, J.-F. Faucon, G. Fourche, J. Dufourcq, T. Gulik-Krzywicki and M. le Maire, FEBS letters **201** (2), 205-209 (1986).
39. R. J. M. Tausk, J. Karmiggelt, C. Oudshoorn and J. T. G. Overbeek, Biophysical chemistry **1** (3), 175-183 (1974).
40. A. Hu, T.-H. Fan, J. Katsaras, Y. Xia, M. Li and M.-P. Nieh, Soft Matter **10** (28), 5055-5060 (2014).
41. M. M. Zetterberg, K. Reijmar, M. Pränting, Å. Engström, D. I. Andersson and K. Edwards, Journal of Controlled Release **156** (3), 323-328 (2011).

# Chapter 4

## The Effect of DSPE-PEG on Bicellar Structure and Thermal Stability

### 4.1 Introduction

The development of "Stealth" liposomes has been attracting the fundamental understanding of the function of the Polyethylene Glycol-conjugated (PEGylated) phospholipids in the bilayer phase and structures[1-3] and the prevention of protein adsorption[4-6]. Besides the PEGylated liposomes, PEGylated lipids and phospholipids mixed micelles have also been studied and used as drug delivery carriers mainly for poorly soluble drugs.[7] The PEG chains on the surface of these assemblies exhibit "mushroom" or "brush" configurations, which are strongly dependent on the PEG molecular weight (MW) and the PEG percentage on the attached surface.[8] The density and thickness of the PEG corona on nanoparticles' surface have been modified to minimize the *in vivo* plasma protein adsorption thus prolong the nanoparticles' blood circulation time.[9]

Theoretical and experimental works have shown variety structures of the PEGylated lipids mixed micelles, such as rod-like, spherical, disc-like micelles and lamellae.[10] Edwards *et al.* found the disc-shaped PEGylated lipid/phospholipid micelles in a certain ratio could be used as the surface-modified model membranes.[11, 12] Researchers have also been developing this type of discs as carriers for Doxorubicin.[13] However, the formation

of the discoidal micelles with usually coexist with other vesicular or rod-like structures.[2] It is important to develop the one-step self-assembly method to provide uniform PEGylated nanodiscs for further applications. di-$C_{18}$ DSPE-PEG2000 have been added to the di-$C_{16}$ DPPC/di-$C_6$ DHPC/di-$C_{16}$ DPPG bicelle system in a ratio of 5 mol% and successfully achieved the goal of manufacturing uniform nanodiscs.[14] It hasn't been fully understood what's the PEGylated lipids function in the bicellar phases.

Based on the critical packing parameter theory[15], PEGylated phospholipids have a large intrinsic curvature (packing parameter ~ 1/3), which should form spherical or nearly spherical micelles in aqueous solution. However, the packing parameter of the phospholipid part under the PEG chain is close to 1 and tend to form the bilayer. So, in the bicelle, PEGylated lipids can work as the bilayer rim stabilizer similar as the short-chain lipids or align with the long-chain lipids forming the bilayer.

In this chapter, the effects of DSPE-PEG on DPPC based bicelle systems will be discussed. DSPE-PEG with different PEG chains lengths and molecular weight have been added to the DPPC/DHPC mixture in the presence or absence of DPPG.

## 4.2 Materials and Methods

### 4.2.1. Materials and sample preparation

Zwitterionic DPPC and DHPC, negatively charged DPPG and three different types of DSPE-PEG with average PEG molecular weights of 750, 2000 and 5000 Da were purchased from Avanti Polar Lipids (Alabaster, AL) and used without further purification. The different PEG-DSPEs are subsequently referred to as DSPE-PEG750, DSPE-PEG2000, and DSPE-PEG5000, respectively. The compositions are listed below,

$$Q\text{-}ratio = \frac{[\mathrm{DPPC}]+[\mathrm{DPPG}]+[\mathrm{DSPE-PEG}]}{[\mathrm{DHPC}]} = 3$$

$$R = \frac{[\mathrm{DPPG}]}{[\mathrm{DPPC}]+[\mathrm{DPPG}]+[\mathrm{DSPE-PEG}]} = 0.01 \text{ or } 0$$

$$\text{PEG mol\%} = \frac{[\mathrm{DSPE-PEG}]}{[\text{Total Lipids}]} = 0, 0.5, 1, 3 \text{ and } 5 \text{ mol\%}$$

The lipid mixtures were weighted and then dispersed in filtered D.I. water to make stock solutions with an initial total lipid concentration in the range 100 to 200 mg/mL. After successive vortex and temperature cycling between 4 and 60 °C, the lipid mixtures were completely dissolved and formed homogenous solutions for all cases. The stock solutions were then progressively diluted at room temperature to the final solutions with total lipid concentrations to 5 mg/mL for SAXS and DLS measurement and 0.01 mg/mL for TEM sample preparation.

### 4.2.2 Methods

Methods include Small Angle X-ray Scattering (SAXS), Dynamic Light Scattering (DLS) and Zeta potential, Differential Refractometer, Negative staining Transmission Electron Microscopy (TEM). The details are introduced in Chapter 2.

## 4.3 Results

### 4.3.1 The Effect of DSPE-PEG on the Disc-Lamella Transition in Bicellar Mixture

SAXS measurements were conducted to investigate whether the DSPE-PEG can disturb the disc-to-lamella transition in high concentration bicelle system. The DPPC/DHPC/DPPG aqueous solutions in the conditions of *Q-ratio* = 3 *R* = 0.01 $C_{lp}$ = 100 mg/mL and different ratio and PEG chain length of DSPE-PEG have been tested in a thermal sequence 25-60-25 °C. The starting SAXS measurements at 25 °C are shown in Figure 4.3.1 (a). The curves from the top to bottom are representing the bicelles with NON-PEG, 0.5 mol% DSPE-PEG2000, 2 mol% DSPE-PEG5000, and 5 mol% DSPE-PEG5000. The data were rescaled by a factor of 2 for clarity. All of the SAXS data have a minimum intensity around $q$ = 0.05 $Å^{-1}$ followed by a broad peak from $q$ = 0.05 to 0.22 $Å^{-1}$. This is the typical behavior for lipid bilayer structures in aqueous dispersions: under X-ray scattering, the phospholipid bilayer has a negative excess scattering length density in the hydrocarbon core and a positive excess scattering length density in the surrounding hydrophilic shell.[16, 17] The peak positions for all the curves remain at the same position around $q$ = 0.127 $Å^{-1}$, which are consistent with the DPPC bilayer thickness 48 Å at T=25 °C.[18] The thickness is practically invariant throughout all samples regardless the presence of DSPE-PEG. The lower-q peaks in each curve presumably represent the structure factors that account for the inter-particle interactions. It has been reported that negatively charged bicellar mixtures can form uniform nano-sized discoidal micelles (nanodiscs) at

the low-T and the high lipid concentration ($C_{lp}$ > 10 mg/mL).[19, 20] In Fig. 4.3.1 (a), the lipid concentrations in all cases are identical ($C_{lp}$ = 100 mg/mL), the samples with the smaller discs presumably have the higher number densities, leading to the shorter inter-particle distances and hence higher $q$ values of the structure factor peaks. The two samples with the higher DSPE-PEG ratios (≥ 2 mol%) are presumably smaller in size, while the 0.5 mol% DSPE-PEG2000 sample seems to yield similar-sized nanodiscs as the bicelles without DSPE-PEG. Therefore, the fact that the higher composition of DSPE-PEG can reduce the size of the high-$C_{lp}$ bicellar discs, which is consistent with the previous report of the low-$C_{lp}$ bicelles.[14]

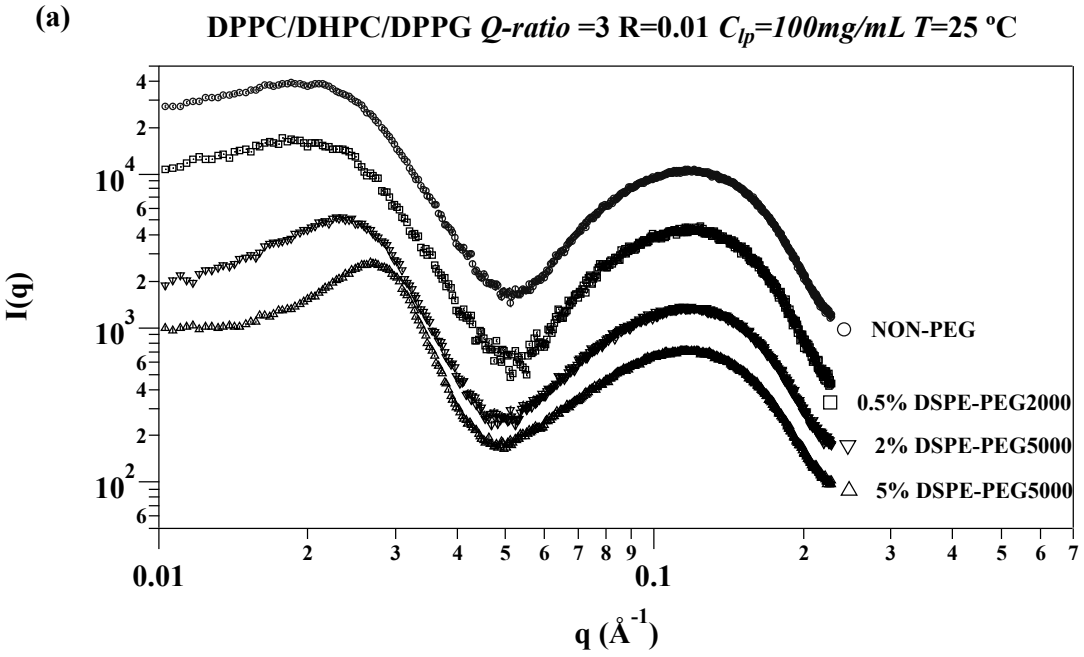

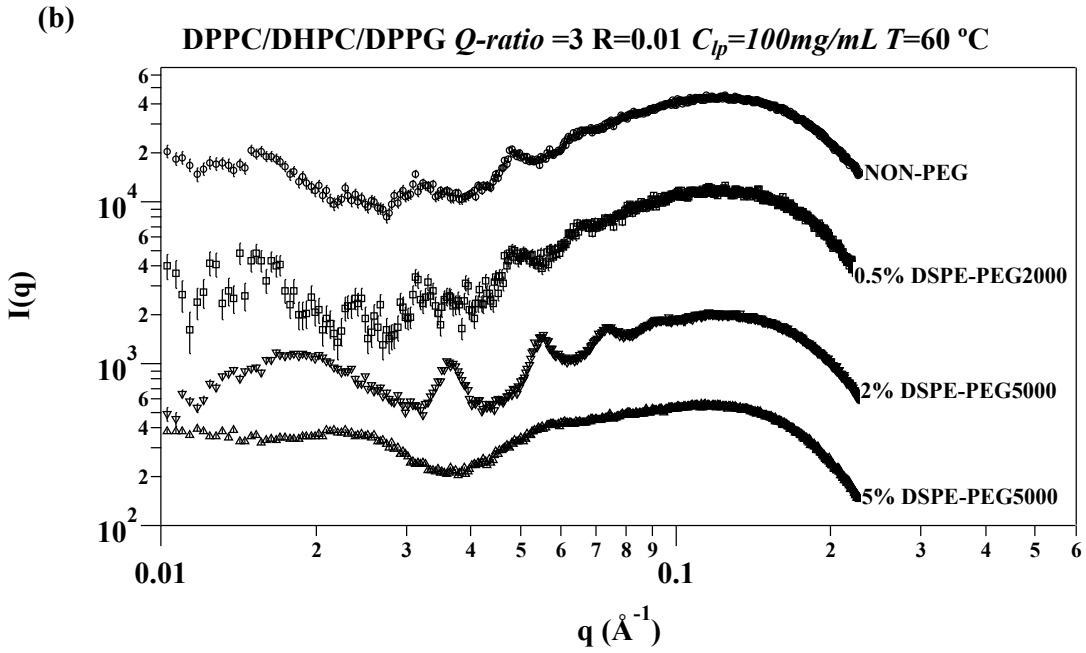


**Figure 4.3.1** SAXS profiles at (a) T=25 °C (b) T=60 °C of DPPC/DHPC/DPPG bicellar aqueous solution in the conditions of *Q-ratio* = 3 $R$ = 0.01 $C_{lp}$ = 100 mg/mL and with different DSPE-PEG ratios and concentrations. For visual clarity, the rescale factors are $2^n$ for (a) and $4^n$ for (b).

After SAXS measurements at 25 °C, the bicellar systems were heated up to 60 °C on stage and equilibrated for 30 minutes before measurement. The SAXS data of bicelles at 60 °C are listed in Fig. 4.3.1 (b) It has been reported that the DPPC/DHPC/DPPG nanodiscs coalesced to perforated lamellae at high-T.[14] The high-order quasi-Bragg peaks of the NON-PEG SAXS curve in Fig. 4.3.1(b) represent for the lamellar phases. The SAXS curves of the DPPC/DHPC/DPPG bicelles containing 0.5 mol% DSPE-PEG2000 and 2% DSPE-PEG5000 show similar lamellar peaks with d-spacings of 370 and 349 Å, respectively. The SAXS curve from the bicelles containing 5 mol% DSPE-PEG5000 exhibits a different scattering pattern with a broad peak at $q^{-1}$ 0.022 Å$^{-1}$, corresponding to a length of 285 Å. The 5 mol% DSPE-PEG5000 presumably attributed to the stronger inter-particle interactions which inhibit the disc coalescence into lamellae. This result is

consistent with a previous NMR study indicating that isotropic phase was observed in the *Q-ratio* = 4.5 DMPC/DHPC bicellar system with a 1.33 mol% DSPE-PEG5000 at 30 °C.[21] This observation suggests that the high content of DSPE-PEG effectively inhibit the coalescence of the nanodiscs into lamellae, possibly due to the strong steric interactions between PEG chains.

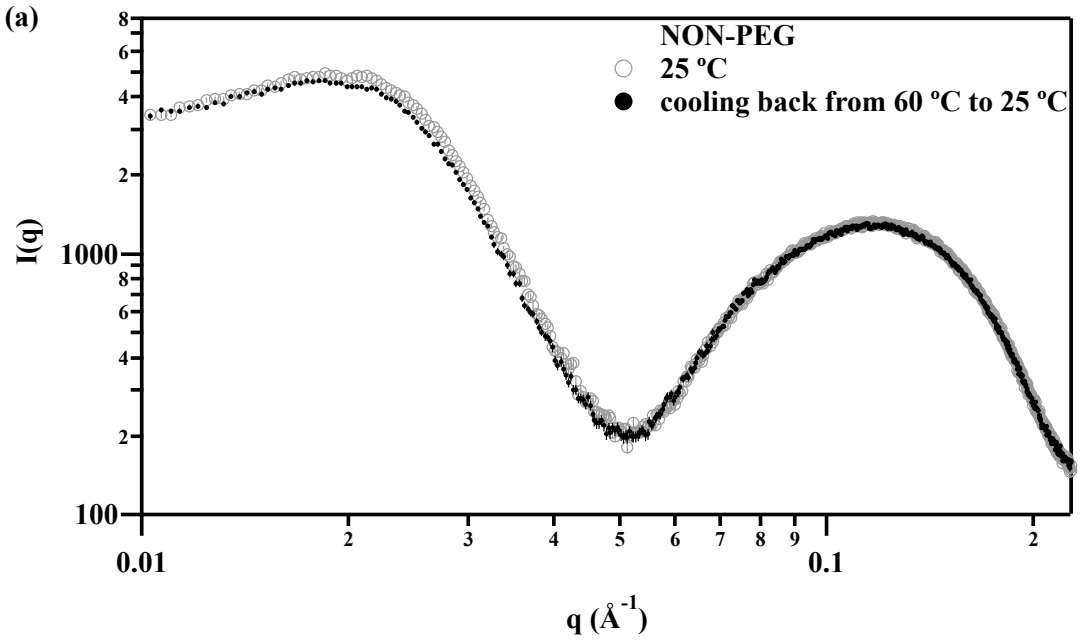

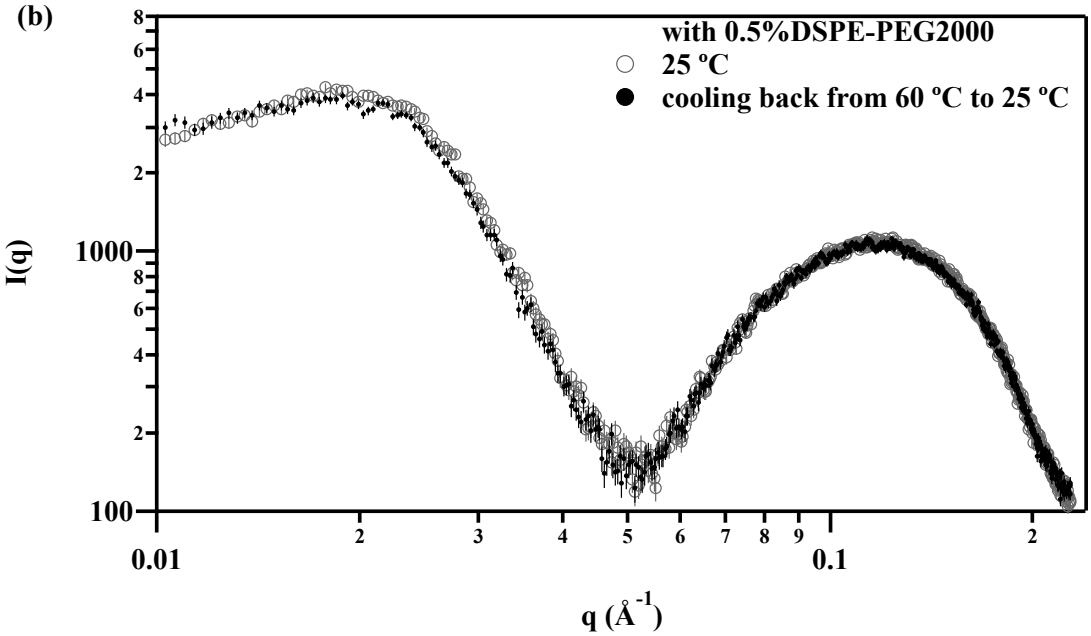
(b)
with 0.5%DSPE-PEG2000
25 ºC
cooling back from 60 ºC to 25 ºC
I(q)
q (Å-1)

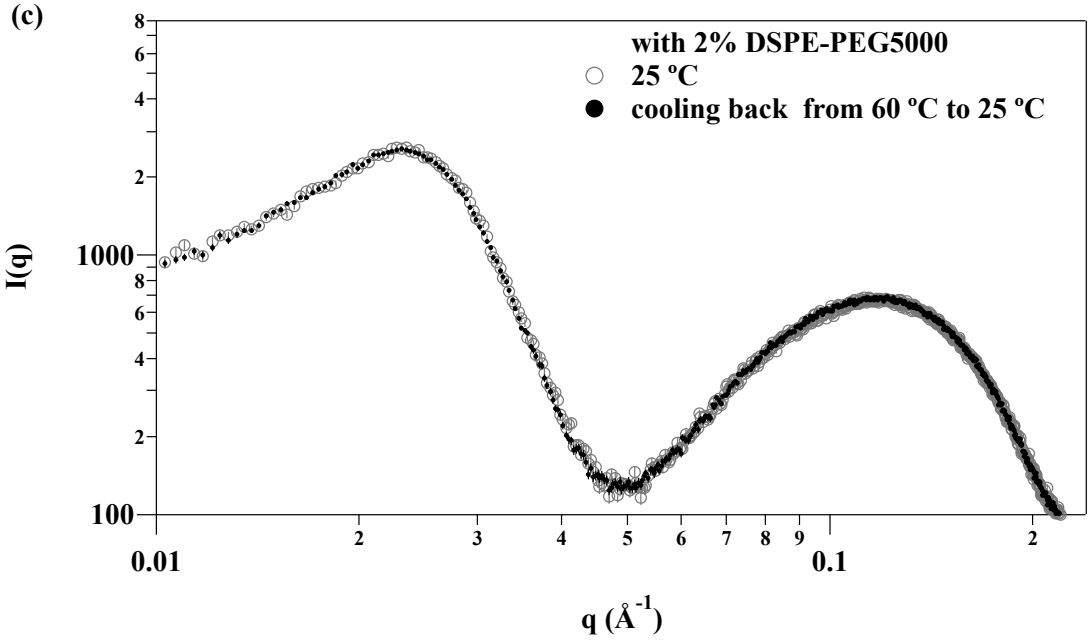
(c)
with 2% DSPE-PEG5000
25 ºC
cooling back from 60 ºC to 25 ºC
I(q)
q (Å-1)

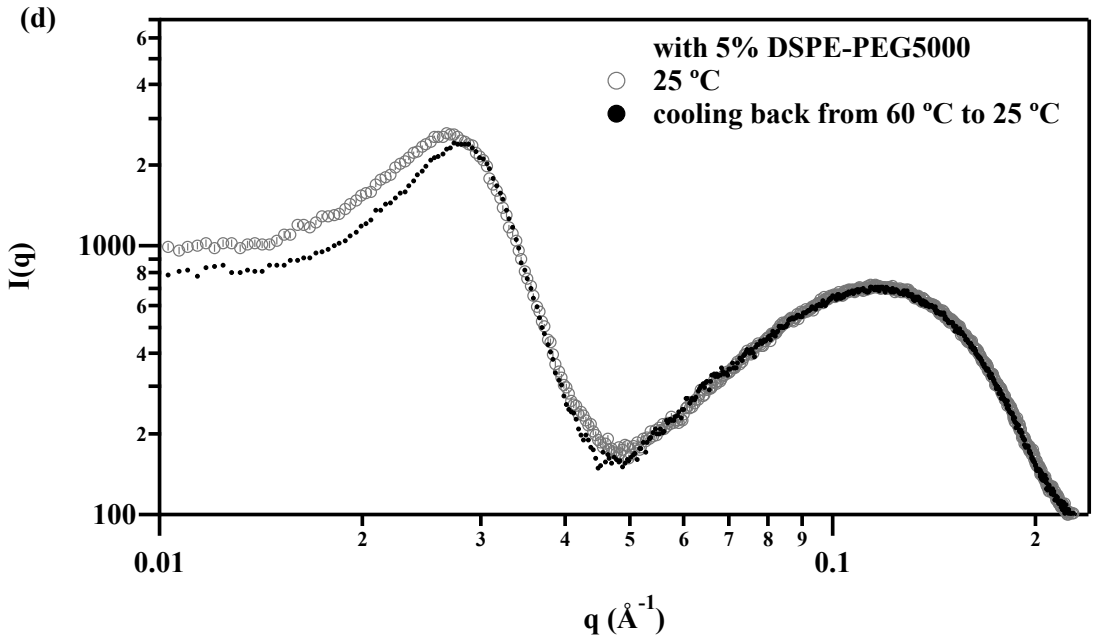


**Figure 4.3.2** SAXS profiles of comparison at T=25 °C before heating up (light circles) and after cooling down (dark spots) of each DPPC/DHPC/DPPG bicellar aqueous solution with different DSPE-PEG ratios and concentrations in the conditions of *Q-ratio* = 3 *R* = 0.01 $C_{lp}$ = 100 mg/mL. (a) NON-PEG (b) 0.5 mol% DSPE-PEG2000 (c) 2 mol% DSPE-PEG5000 (d) 5 mol% DSPE-PEG5000.

The bicellar systems have been cooling down from 60 °C to 25 °C for validating the disc-lamella reversible transition. Figure 4.3.2 shows the comparisons of each system at the states before heating up and after cooling down. Except for the bicelle with 5% DSPE-PEG5000, all the three systems can almost have the curves back to the original positions. These phenomena imply that the self-assembly method of producing the uniform bicellar discs may not work when the DSPE-PEG ratio reaches the limit in the lipid mixture. The explanation has been purposed that at higher PEG surface densities, the PEGylated lipids begin to exert an inter-bicelle steric pressure thus the self-assembly must reorganize.[21]

### 4.3.2 The Effect of DSPE-PEG on the Size and Shape of Bicellar Assemblies at Low-$C_{lp}$ and low-T

#### a) DSPE-PEG750

At the dilute condition $C_{lp}$ = 5mg/mL, the structures of DPPC/DHPC/DPPG mixtures with different ratio of DSPE-PEG750 have been studied through SAXS and negative staining TEM. Figure 4.3.3 shows the SAXS profiles of the *Q-ratio* = 3 $R$ = 0.01 $C_{lp}$ = 5 mg/mL DPPC/DHPC/DPPG with (a) NON-PEG (b) 0.5 mol% (c) 1 mol% and (d) 5 mol% DSPE-PEG750 at 25 °C with their fitting curves. The relevant negative staining TEM micrographs of the samples are also shown with the SAXS figures. All the SAXS intensities have been normalized to the one-hour measurement period, so the relative intensities are comparable. Polydisperse Radius Core-Shell Disc (*Poly-CS-Disc*) model is the SAXS fitting model. The choice of the fitting model is based on the TEM pictures and the similar DPPC/DHPC/DPPG bicellar system.[14] The fitting results are listed in Table 4.3.1. The standard deviation is incorporated in the polydispersity.

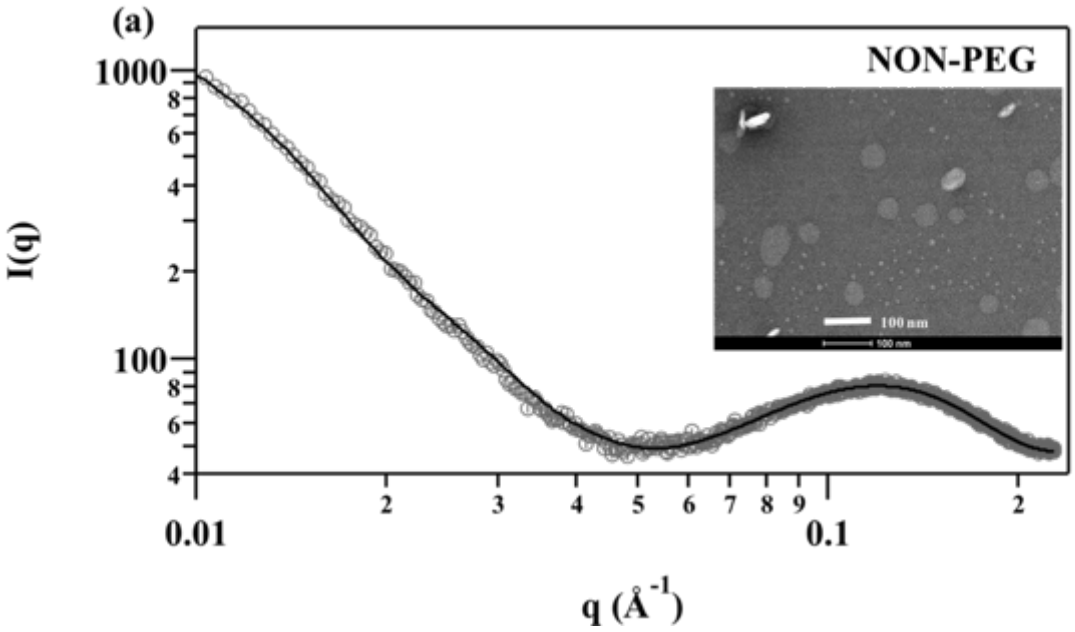
(a)
NON-PEG
1000
100
I(q)
0.01
0.1
q (Å$^{-1}$)
100 nm

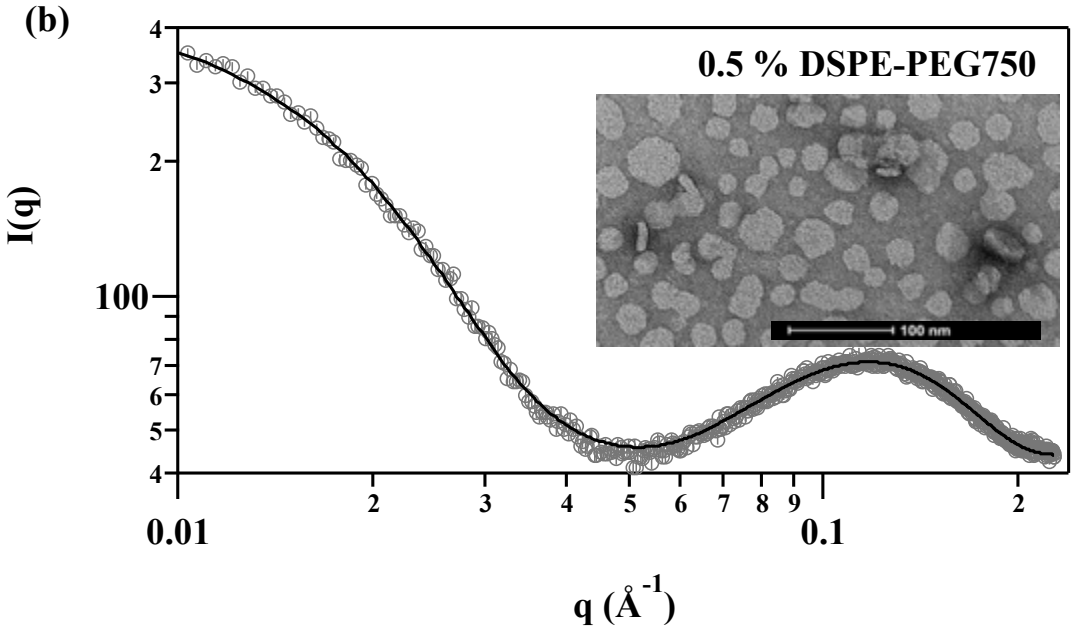
(b)
0.5 % DSPE-PEG750
100
I(q)
0.01
0.1
q (Å$^{-1}$)
100 nm

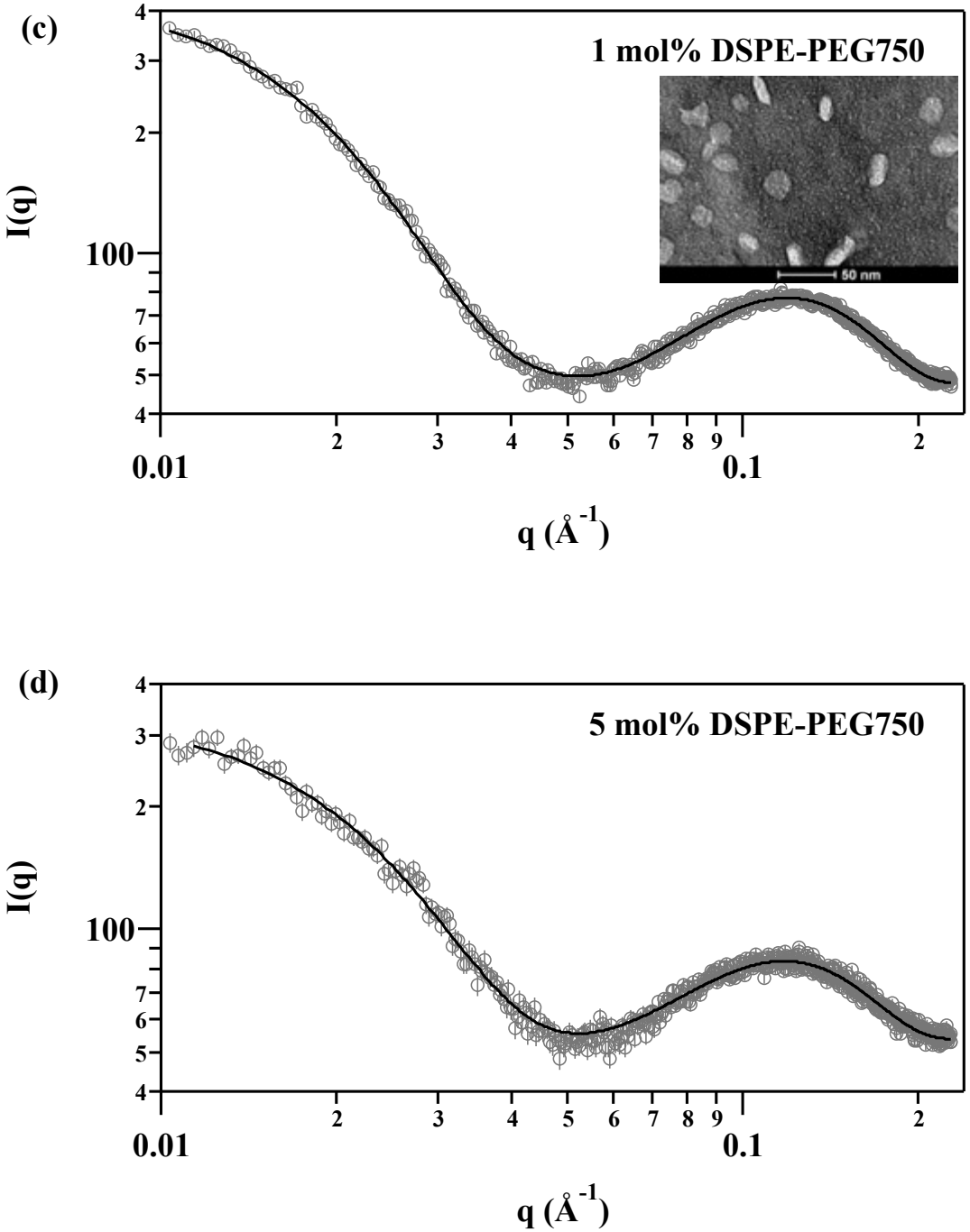


**Figure 4.3.3** SAXS profiles of *Q-ratio* = 3 *R* = 0.01 $C_{lp}$ = 5 mg/mL T=25 °C DPPC/DHPC/DPPG bicellar aqueous with DSPE-PEG750 in ratio of (a) NON-PEG (b) 0.5 mol% (c) 1 mol% (d) 5 mol%. Black curves on the light circle data are the PR-CS-disc fittings.

| **Table 4.3.1** PR-CS-Disc model fitting parameters of the SAXS data of low-T 25 °C *Q-ratio* =3 *R*= 0.01 5 mg/mL DPPC/DHPC/DPPG with different molar ratio of DSPE-PEG750 | | | | |
|---|---|---|---|---|
| Molar Percentage of DSPE-PEG750 to Total Lipids | 0 % | 0.5 % | 1 % | 5 % |
| CORE radius/Å | 300.1 | 89.1 | 83.0 | 65.8 |
| Polydispersity of Radius (sigma) | 0.3 | 0.17 | 0.18 | 0.23 |
| CORE length/Å | 29.1 | 30.0 | 31.3 | 32.2 |
| Planar shell thickness/Å | 11.3 | 9.9 | 9.7 | 9.8 |
| Rim shell thickness/Å | 3 | 3 | 3 | 3 |

All these samples are considered to be discoidal shape based on the TEM and SAXS results. There are clear round surface and narrow edges parts in the TEM pictures. All of these curves showed the slope of $q^{-2}$ from 0.02 to 0.04 $Å^{-1}$, representing the 2-D flat bilayer surfaces in the discs. The SAXS curve of Non-DSPE-PEG sample in Figure 4.3.3 (a) still follows the slope of $q^{-2}$ in the range of 0.01- 0.02 $Å^{-1}$ and presents the highest intensity in this range compared to the other three samples in Figure 4.4.3(b) (c) and (d).

The comparison of the I($q$) of each SAXS curve at the $q$ = 0.01 $Å^{-1}$ show a decreasing trend with more percentage of DSPE-PEG750 in the bicelle system. This behavior is presumably caused by the bicellar particle size decreasing with more DSPE-PEG750 in the mixture solutions. Table 4.3.1 shows the fit results for the SAXS profiles in Figure 4.3.3. The fit radii of the NON-PEG, 0.5, 1 and 5 mol% DSPE-PEG750 discs are 300.1, 89.1, 83.0 and 65.8 Å respectively, while the thickness fittings of the discs are almost the same in the range of 52-54 Å (thickness = core+2*shell). The thickness uniformity of different ratio of PEGylated lipids indicates the bilayer structures have retained in these conditions. The ideal bicelle's *Q-ratio* relationship to the discs' radii is expressed as

$$Q-ratio=\frac{[Long]}{[Short]}=\frac{A_{center}}{A_{rim}}=\frac{R^2}{(\pi R+2r)r} \qquad \text{(Eqn. 4.3.1)}$$

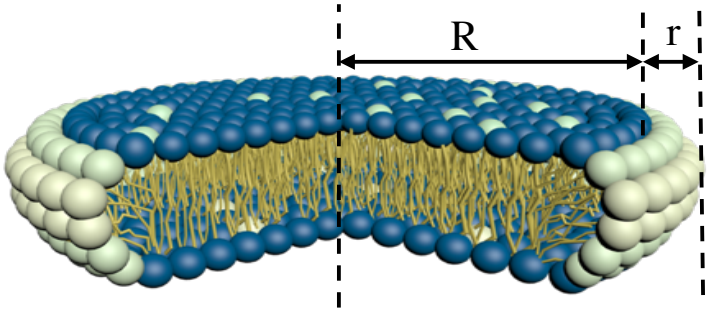


**Figure 4.3.3** Labelled bicelle disc structure for the refined ideal bicelle model

However, based on this calculation, the *Q-ratio* = 3 disc should have a radius *R* in 26 nm with a rim length *r* 2.5 nm. This theoretical value is 8.5 nm larger than the 20 nm radius we obtained in the SAXS fitting for the *Q-ratio* =3 *R*= 0.01 5 mg/mL DPPC/DHPC/DPPG discs. Thus, the ideal bicelles' *Q-ratio* and size relationship cannot be used to analyze the charge system.

Look back to the fitted SAXS data in Table 4.3.1, it is very obvious that a small 0.5 mol% of DSPE-PEG750 reduced the discs' radii from 20 nm to 10.3 nm. Even though the radii of the discs show a decreasing trend with DSPE-PEG750 ratio ascending, it's still hard to conclude the size dependence on PEG ratio in the polydispersity ranges. Presumably, the DSPE-PEG750 can anchor the DSPE part in the DPPC bilayer, or coat on the rim of disc, or in both the rim and surface regions.

**b) DSPE-PEG2000**

DSPE-PEG2000 have been incorporated in the DPPC/DHPC/DPPG bicellar system to compare with the bicelles with same ratios of DSPE-PEG750. Figure 4.3.5 presents the SAXS profiles of the *Q-ratio* = 3 *R* = 0.01 $C_{lp}$ = 5 mg/mL DPPC/DHPC/DPPG with (a) 0.5 mol% (b) 1 mol% and (c) 5 mol% DSPE-PEG2000 at 25 °C with their fitting curves. The fitting results are listed in Table 4.3.2.

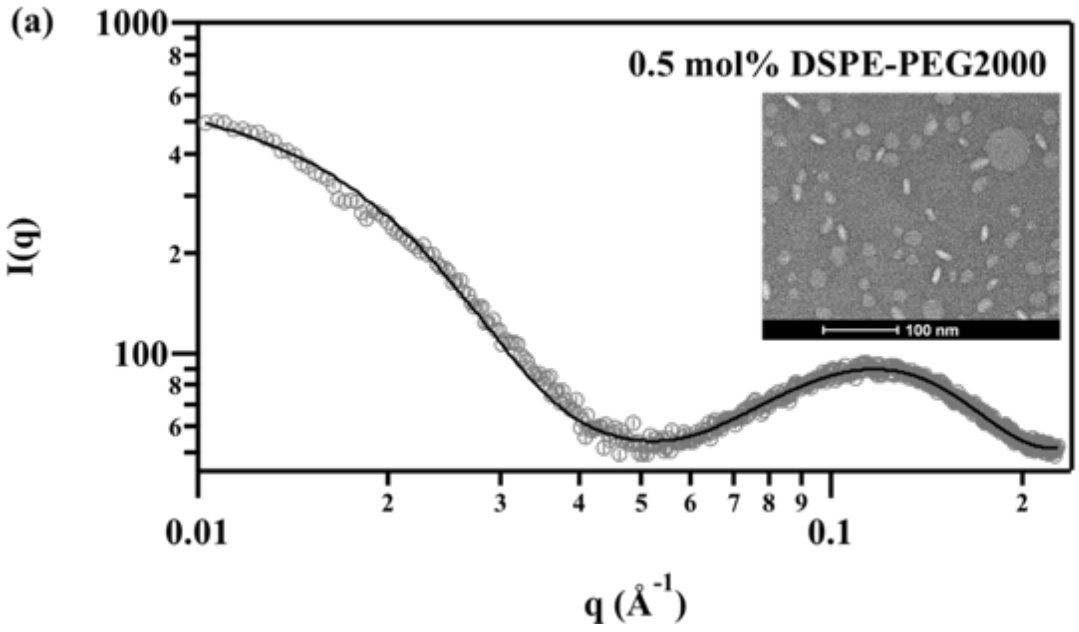

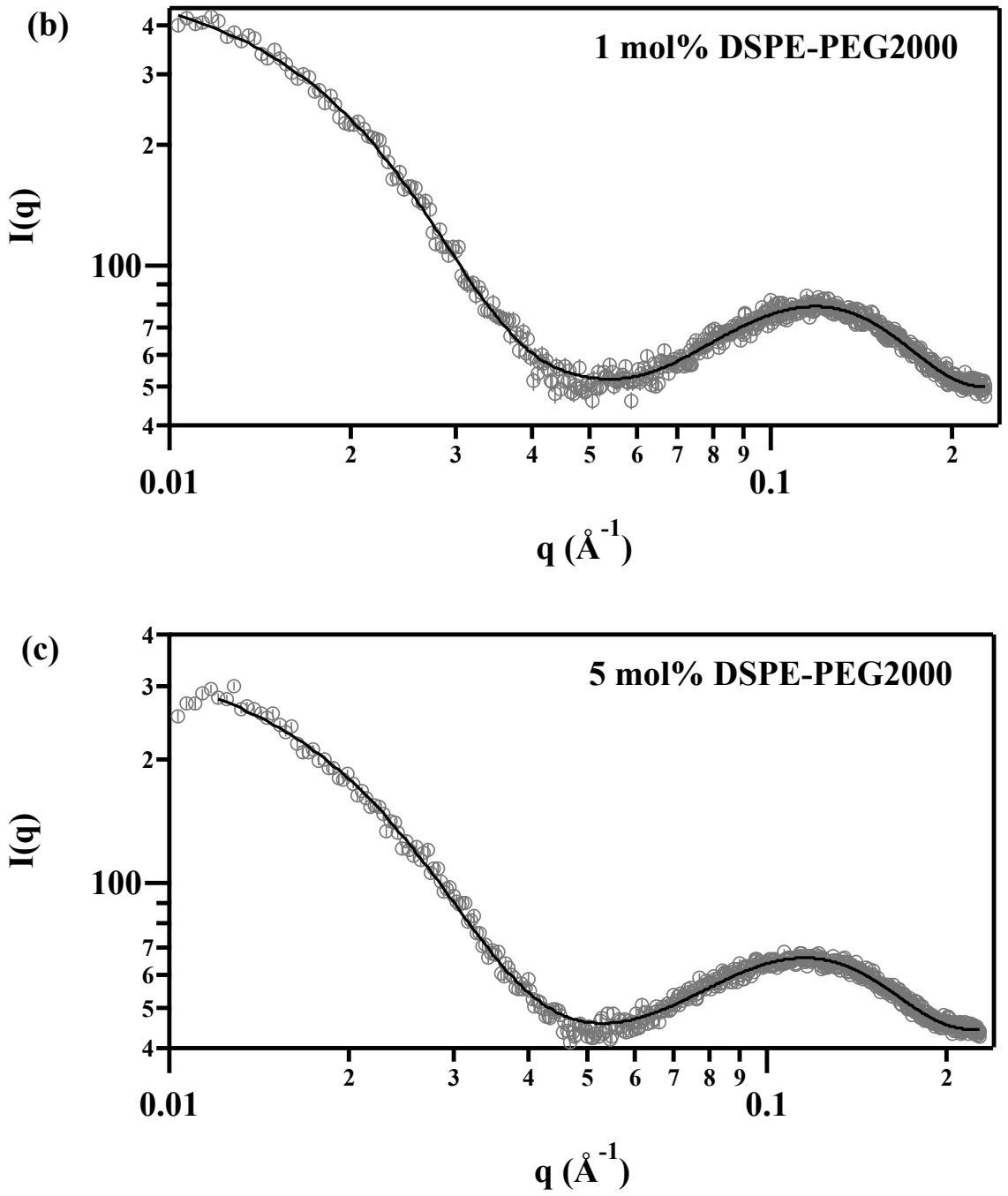


**Figure 4.3.5** SAXS profiles of *Q-ratio* = 3 *R* = 0.01 $C_{lp}$ = 5 mg/mL T=25 °C DPPC/DHPC/DPPG bicellar aqueous with DSPE-PEG2000 in ratio of (a) 0.5 mol% (b) 1 mol% and (c) 5 mol%. Black curves on the light circle data are the PR-CS-disc fittings. The relevant negative staining TEM pictures were aside the SAXS curve.

| **Table 4.3.2** PR-CS-Disc model fitting parameters of the SAXS data of low-T 25 °C Q-ratio=3 R=0.01 1 mg/mL DPPC/DHPC/DPPG with different molar ratio of DSPE-PEG2000 | | | |
|---|---|---|---|
| Molar Percentage of DSPE-PEG2000 to Total Lipids | 0.5 % | 1 % | 5 % |
| CORE radius/Å | 77.0 | 87.2 | 76.0 |
| Polydispersity of Radius (sigma) | 0.3 | 0.22 | 0.22 |
| CORE length/Å | 31.6 | 31.1 | 32.0 |
| Planar shell thickness/Å | 10.2 | 10.3 | 10.9 |
| Rim shell thickness/Å | 3 | 3 | 3 |

The DPPC/DHPC/DPPG bicelles with the different ratio of DSPE-PEG2000 are still observed as discs through TEM and SAXS. Table 4.3.2 indicates that the best fitting radii of the discs with 0.5, 1 and 5 mol% DSPE-PEG2000 are 77.0, 87.2 and 76.0 Å and the thicknesses of the discs are also in the range between 52 and 55 Å as their DSPE-PEG750 counterparts.

**c) DSPE-PEG5000**

DSPE-PEG5000 have than the DSPE-PEG2000. The influence of this bulk head lipids in the *Q-ratio* = 3 $R$ = 0.01 $C_{lp}$ = 5 mg/mL DPPC/DHPC/DPPG bicelles has been investigated through SAXS and TEM. (Figure 4.3.6) In the 0.5 mol% DSPE-PEG5000 system, the discs and ribbon-like micelles mixture have been observed in TEM. Comparing the best fitting results of DSPE-PEG5000 bicelles(Table 4.3.3) to the others, we first notice there is a significant difference in radii between the DPPC/DHPC/DPPG discs without any DSPE-PEG (300.1 Å) and with different types and ratios of DSPE-PEG (65.8-104.3 Å). In these systems, the radii of bicellar discs are practically the same in the mixtures containing PEGylated lipids of different PEG lengths (PEG750, PEG2000 and

PEG5000) at the corresponding $C_{lp}$ indicates an insignificant effect of PEG length on determining the size of discs.

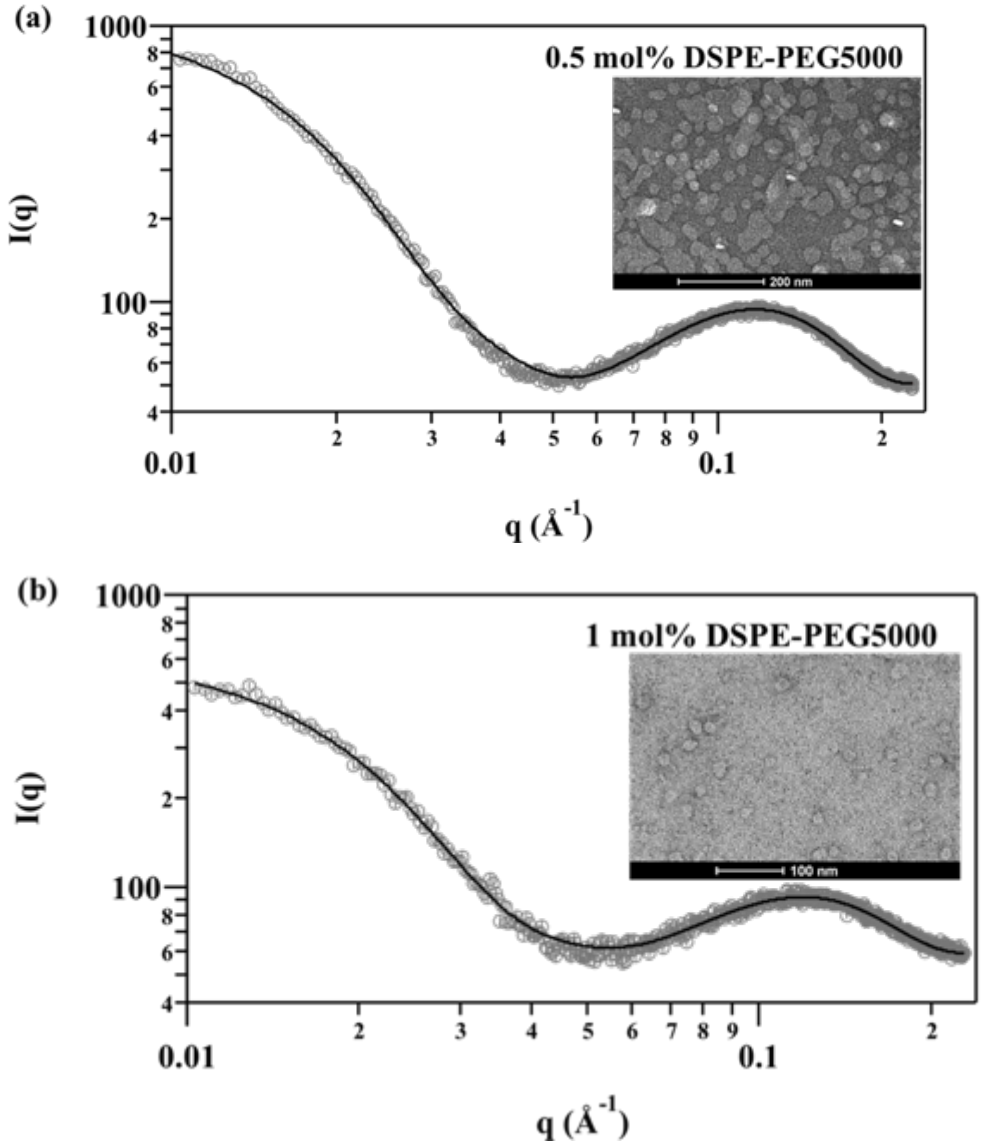


**Figure 4.3.6** SAXS profiles of *Q-ratio* = 3 $R$ = 0.01 $C_{lp}$ = 5 mg/mL T=25 °C DPPC/DHPC/DPPG bicellar aqueous with DSPE-PEG5000 in ratio of (a) 0.5 mol% and (b) 1 mol%. Black curves on the light circle data are the PR-CS-disc fittings. The relevant negative staining TEM pictures were aside the SAXS curve

| **Table 4.3.3** PR-CS-Disc model fitting parameters of the SAXS data of low-T 25 °C Q-ratio=3 R=0.01 1 mg/mL DPPC/DHPC/DPPG with different molar ratio of DSPE-PEG5000 | | |
|---|---|---|
| Molar Percentage of DSPE-PEG2000 to Total Lipids | 0.5 % | 1 % |
| CORE radius/Å | 104.3 | 89.5 |
| Polydispersity of Radius | 0.14 | 0.18 |
| CORE length/Å | 31.3 | 30.9 |
| Planar shell thickness/Å | 10.8 | 10.3 |
| Rim shell thickness/Å | 3 | 3 |

### 4.3.3 The Effect of DSPE-PEG on the Thermal Stability of Bicellar Assemblies at Low-$C_{lp}$ and high-T

The bicellar structures at the high-T were also monitored by SAXS, when the 5 mg/mL DPPC/DHPC/DPPG bicelles in the presence and absence of DSPE-PEG were heated up to 60 °C (Fig. 4.3.7). The SAXS data can be fitted with the three-layer core-shell vesicle model (Chapter 2). The best fitting results are shown in Table 4.3.4. The major differences between the high-T (Fig. 4.3.7) and the low-T SAXS data of the same systems are the broader width of the bilayer peak and the lower intensity in the low-$q$ range at 60 °C than 25 °C. The similar phenomenon was also observed in the high-$C_{lp}$ bicelles (Fig. 4.3.1). The integrated total scattering density of lipids solutes decreases with temperature. This effect is presumably due to the thermal expansion of the lipid bilayer and concomitant decrease of lipid scattering length density.[16] At 0.5 and 1 mol% DSPE-PEG, the vesicle size seems to have a PEG length dependence that smaller vesicles forming with the longer the PEG chain. However, fitting results of 5% DSPE-PEG750

vesicles are smaller in radius than the DSPE-PEG2000 ones. The bilayer thickness fitting results are similar in all the cases.

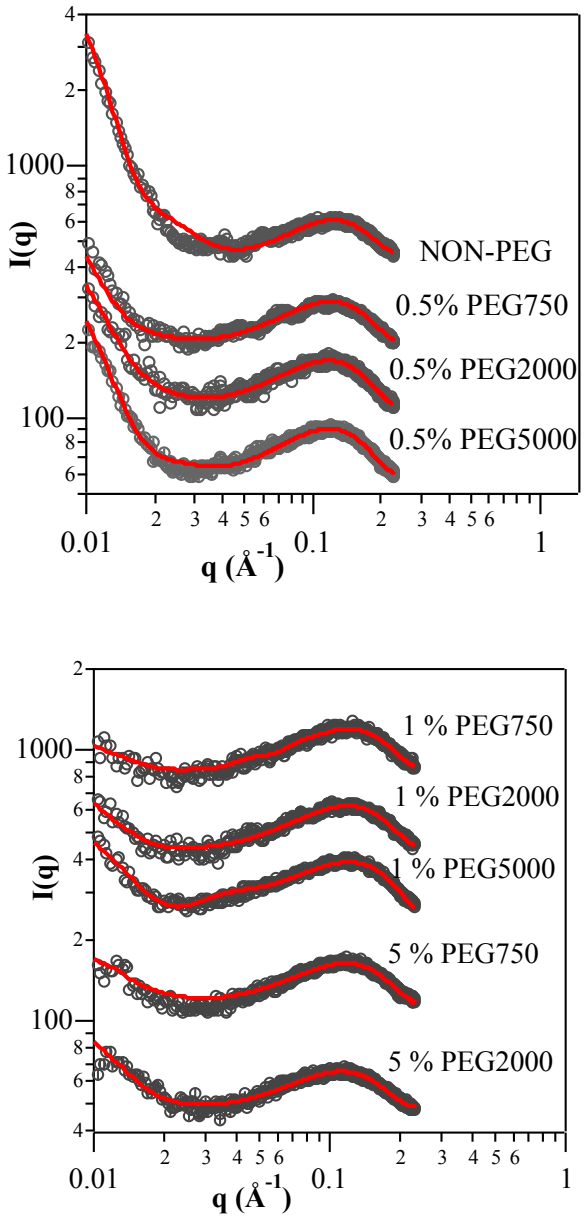


**Figure 4.3.7** SAXS profiles from the *Q-ratio* = 3, *R* = 0.01, $C_{lp}$ = 5mg/mL, DPPC/DHPC/DPPG bicelles at 60 °C with 0, 0.5 mol% and 1, 5 mol% DSPE-PEG750, DSPE-PEG2000 and DSPE-PEG5000. Red curves on the light circle data are the three-layer vesicle fittings. For better visibility, the I(q) of data sets in each plot are rescaled by 2*n* where *n* runs from 0 to 4 starting from the bottom curve.

| **Table 4.3.4** Three-layer vesicle model fitting parameters of the SAXS data of high-T 60 °C *Q-ratio* = 3 *R* = 0.01 $C_{lp}$ = 5 mg/mL DPPC/DHPC/DPPG with different molar ratio of DSPE-PEG and different PEG MW | | | | | | | | | |
|---|---|---|---|---|---|---|---|---|---|
| Samples with | Non-PEG | 0.5% DSPE-PEG | | | 1% DSPE-PEG | | | 5% DSPE-PEG | |
| MW of PEG Chain | | 750 | 2000 | 5000 | 750 | 2000 | 5000 | 750 | 2000 |
| Core radius/Å | 104.6 | 95 | 92.1 | 83.1 | 79.7 | 71.1 | 48.1 | 70.8 | 93.2 |
| Polydispersity | 0.4 | 0.5 | 0.3 | 0.5 | 0.2 | 0.5 | 0.5 | 0.3 | 0.3 |
| Inner shell thickness/Å | 7.9 | 7.0 | 9.7 | 7.1 | 7.8 | 7.7 | 5.5 | 7.3 | 9.5 |
| Hydrophobic layer thickness/Å | 28.9 | 29.0 | 29.0 | 29.2 | 28.7 | 29.0 | 27.2 | 29.6 | 30.7 |
| Outer shell thickness/Å | 8.8 | 7.3 | 5.7 | 8.1 | 5.9 | 6.3 | 6.8 | 6.5 | 6.2 |

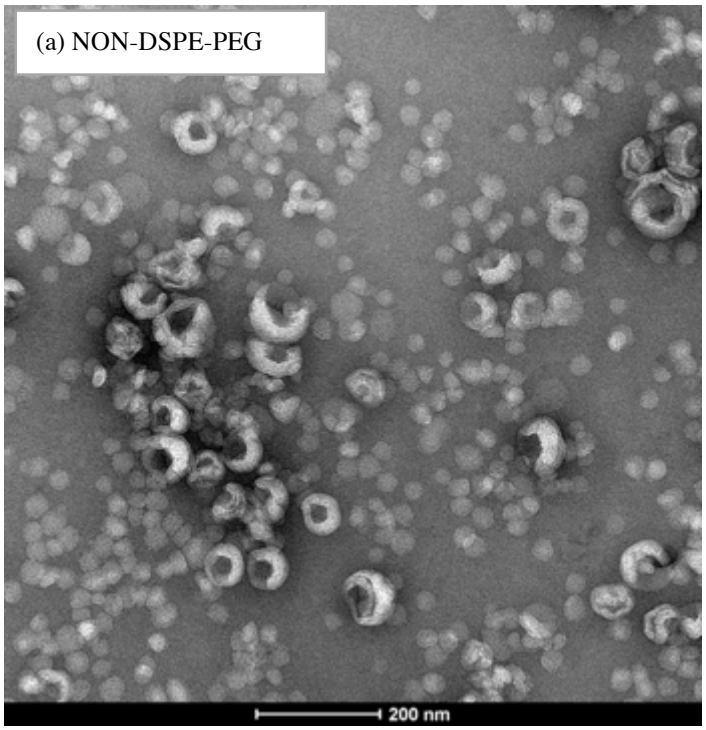

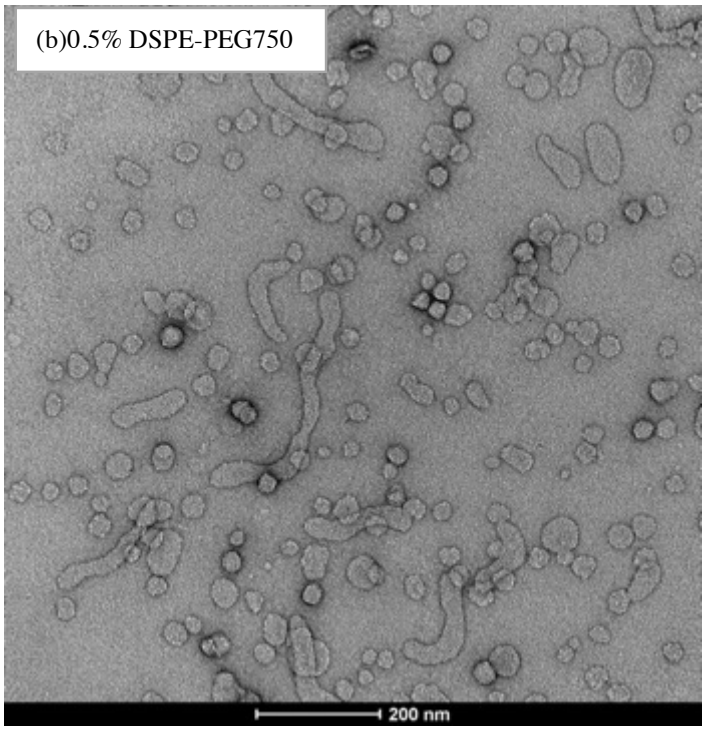
(b)0.5% DSPE-PEG750
200 nm

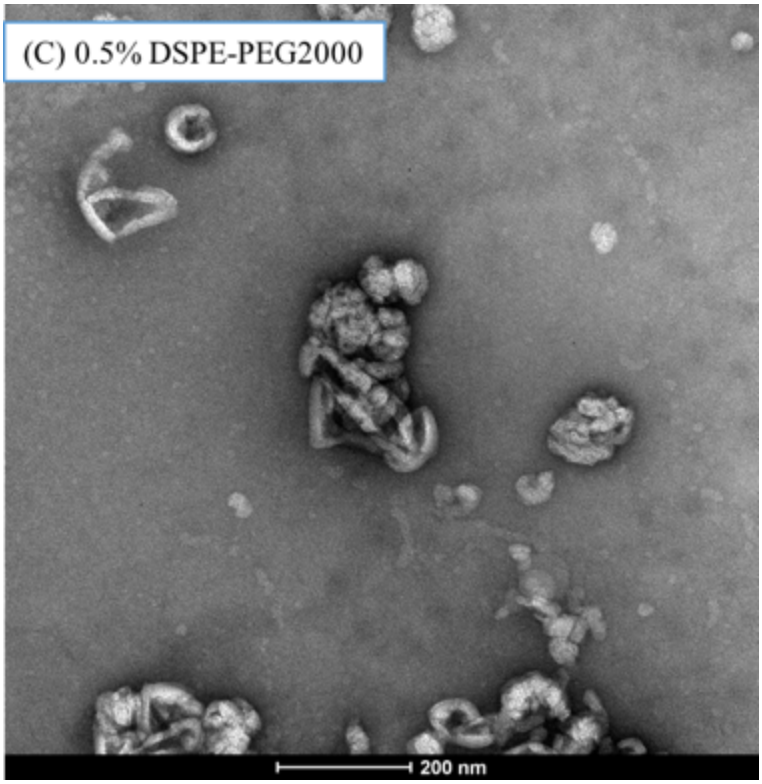
(C) 0.5% DSPE-PEG2000
200 nm

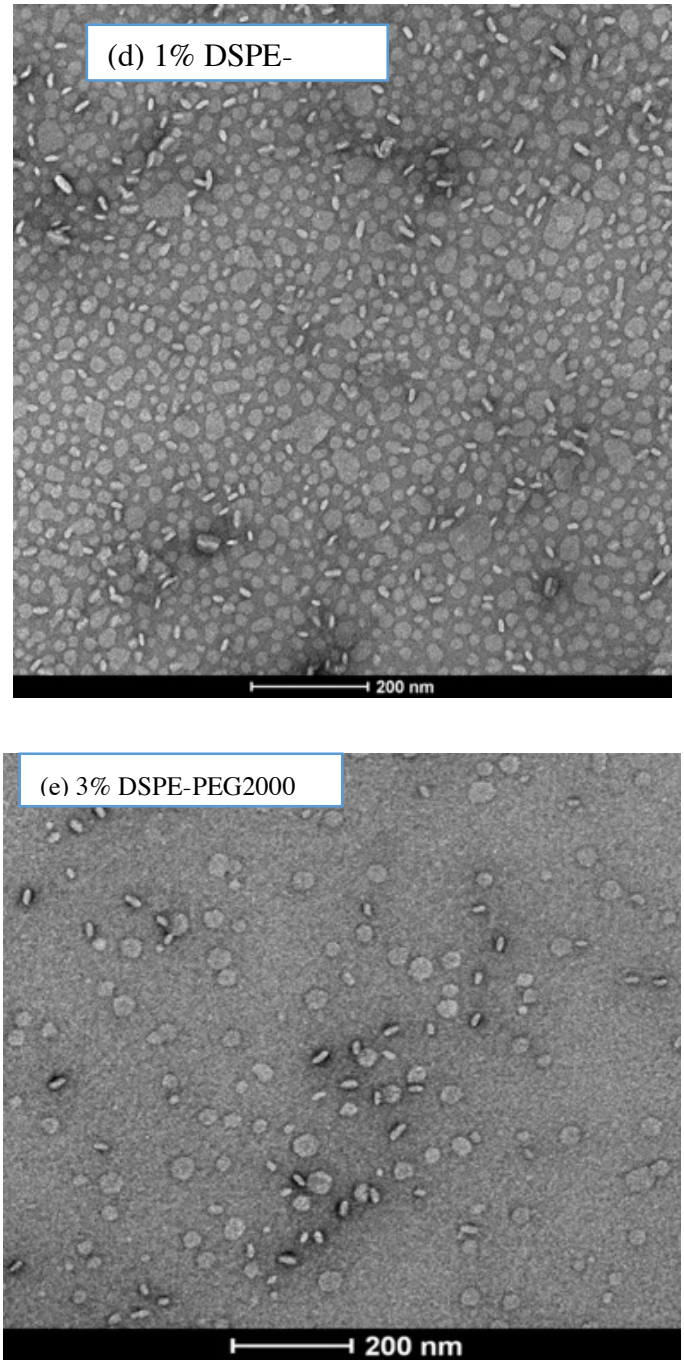


**Figure 4.3.8** TEM pictures of samples at 60 °C *Q*-ratio=3 R=0.01 $C_{lp}$ = 5 mg/mL (a) Non-PEG (b) 0.5% DSPE-PEG750 (c) 0.5% DSPE-PEG2000 (d) 1% DSPE-PEG200 (e) 3%DSPE-PEG2000

In Figure 4.3.8 (a), TEM pictures of the NON-PEG DPPC/DHPC/DPPG bicelles shows broken vesicles mixed with some small spherical shapes. This is an evidence to

show the disc-to-vesicle transition happed at 60 °C in the 5 mg/mL NON-PEG bicelles. The polydispersity of size and shape may be from the sample preparation process. This conclusion is consistent with the similar transition in the former reported *Q*-ratio=3.3 R=0.01 $C_{lp}$ = 3 mg/mL DMPC/DHPC/DMPG system.[22] In the presence of 0.5 mol% DSPE-PEG750 and DSPE-PEG2000 in bicelles heating to 60 °C, Irregular shapes such as "ribbon-like" micelles[Figure 4.3.8(b)] and vesicles[Figure 4.3.8(c)] mixed with discs have been found respectively, despite both of the systems presented as discs at 25 °C [Figure 4.3.3(b) and Figure 4.3.5(a)]. The different shaped mixture formation illustrates that the 0.5mol% of DSPE-PEG with PEG MW 750 and 2000 in the bicellar discs can slow down but not completely inhibit the inter-particle coalescence at high temperature. When the bicelles were incorporated with 1 mol% DSPE-PEG2000, the nanodisc structures have been kept at 60 °C with a small portion of larger aggregates ~ 100 nm. The TEM result of the bicelles with 3 mol% DSPE-PEG2000 at 60 °C [Figure 4.3.8 (e)] exhibits smaller and more uniform discs than the one with 1 mol% DSPE-PEG2000 ones at 60 °C. With this evidence, it can be concluded that the addition of 1-5 mol% of DSPE-PEG750 and DSPE-PEG2000 can improve the thermal stability of the DPPC/DHPC/DPPG bicelles at 60 °C. And the 5 mol% DSPE-PEG can achieve the best thermal stable discs at high temperature. The kinetics of discs change at high-T are in need to validate the hypothesis.

The SAXS measurement time is usually up to hours to obtain enough scattered information while it is not suitable to catch the instant kinetic variation in solution. DLS can be used to

monitor the nano-sized particles in the *Q*-ratio=3 R=0.01 $C_{lp}$=5 mg/mL DPPC/DHPC/DPPG with different percentage of DSPE-PEG2000. In the DLS experiments, all the samples with different percentage of DSPE-PEG2000 have the same thermal path from 25 to 60 °C. The heating-up process usually took 5-7 minutes from 25 to 60 °C and reached equilibrium. The monitored light scattered intensities v.s. time are shown in Figure 4.3.9.

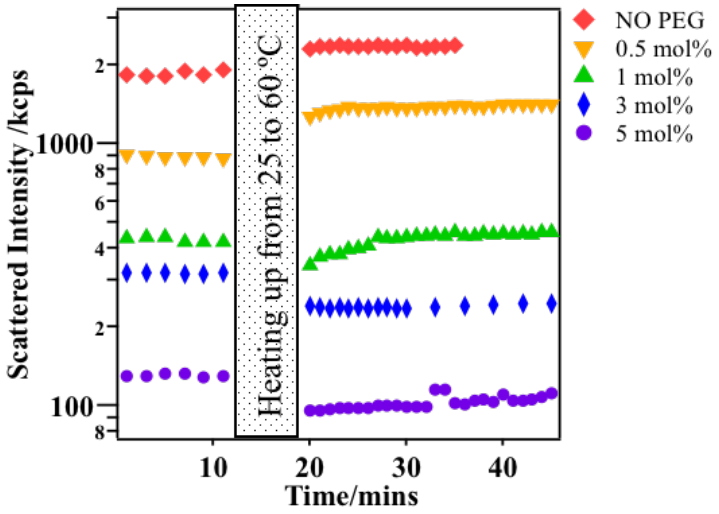


**Figure 4.3.9** Dynamic light scattering intensities v.s. time at temperature 25 → 60 °C of the *Q*-ratio=3 R=0.01 $C_{lp}$=5 mg/mL DPPC/DHPC/DPPG with different molar percentage of DSPE-PEG2000. The void part is the heating up and equilibrium periods. Intensity value is an average of 1-minute measurement.

It's first noticed that the scattered light intensities at the low-T range follow a decreasing trend with increasing DSPE-PEG2000 ratio, which is corresponding to the scattered X-ray intensities reducing with more DSPE-PEG2000 in Figure 4.3.5. The DLS intensity trend is a further evidence of the disc size reduction caused by additional DSPE-PEG amount. When the temperature reaches 60 °C, the DLS intensities of the NON-PEG and 0.5 mol% PEG2000-DSPE

bicelles jumped to their relative higher levels. The intensity of the 1 mol% DSPE-PEG2000 sample dropped initially then increased to the similar level as at 25°C. For the 3 and 5 mol% DSPE-PEG2000 bicelles, the intensities declined and remained lower than their original 25 °C levels.

How to explain these scattered intensities shifting trends to higher or lower level? The change in refractive index of solutions as a function of solute concentration (*dn/dc*, also called refractive index increment) is the essential parameter to clarify the situation. The scattered light intensity and the *dn/dc* relationship is showed in Eqn. 4.3.2. During the DLS experiment, all the apparatus parameters have been kept the same, the only variables in my conducted experiments are the molecular weight and the *dn/dc* of the solute particles.

$$\text{The scattered intensity: } I_s = \frac{4\pi^2 M^2 (\sin^2\phi)(dn/dc)^2 I_0}{N_A^2 \lambda^4 R^2} \qquad \text{(Eqn. 4.3.2)}$$

$M$ molecular weight of solute

$\phi$ the complementary angle between incident light and scattered light

$I_0$ the incident light intensity

$N_A$ Avogadro's number

$\lambda$ the wavelength of light in the solution

$R$ the distance from the scattering point to the observation point

A series of refractive index measurements have conducted to obtain the *dn/dc* of the mixture lipid dispersion, including the same composition solution with ten different concentrations from

1 to 10 mg/mL with water as the parallel solvent backgrounds. In the *Q*-ratio=3 *R*=0.05 DPPC/DHPC/DPPG with 5 mol% DSPE-PEG2000 system, the measured *dn/dc* is 0.1371 mL/g at 31°C and 0.1145 mL/g at 60 °C.

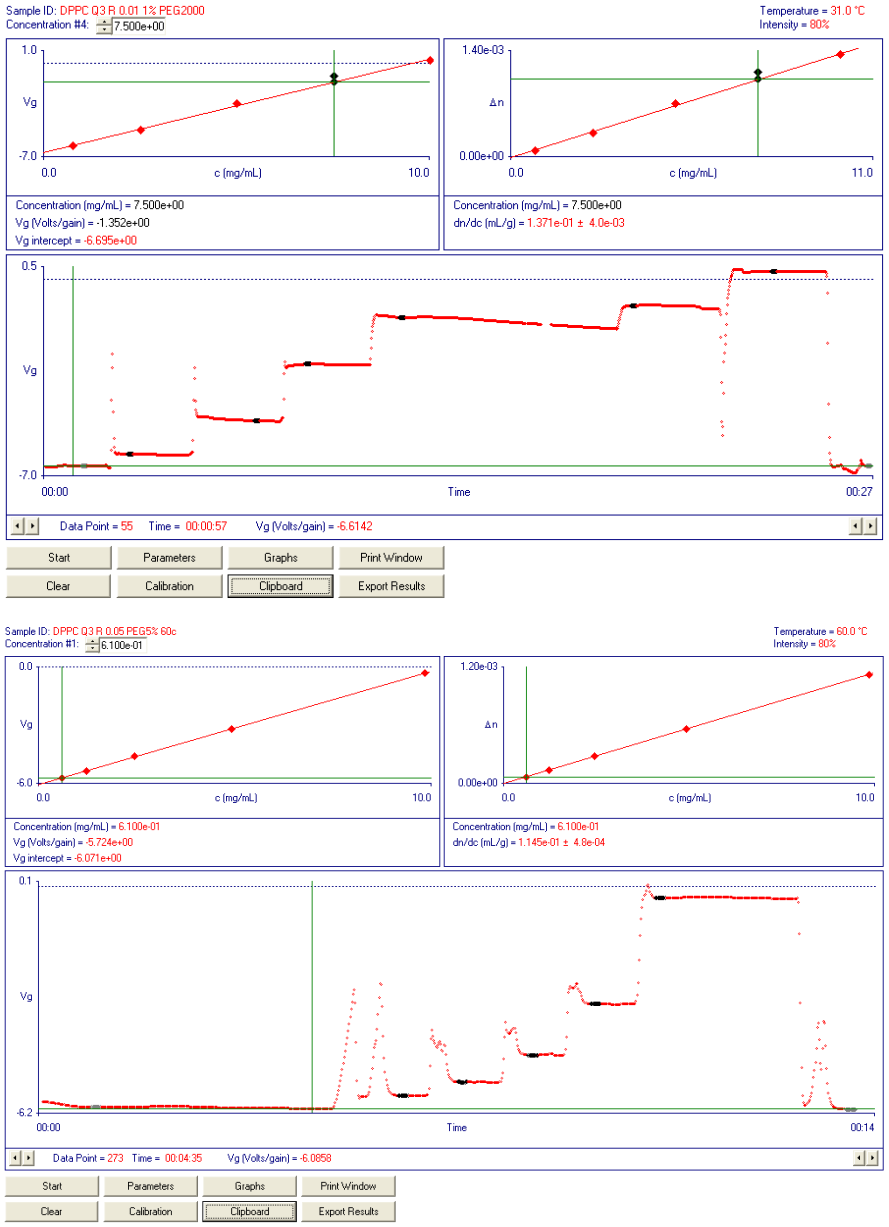


**Figure 4.3.10.** *dn/dc* measurements of the *Q*-ratio=3 R=0.05 DPPC/DHPC/DPPG with 5 mol% DSPE-PEG2000 at 31 and 60 °C.

Since the majority of the components in bicelles are DPPC, the systems with different DPPG and DSPE-PEG ratios are considered to have the similar *dn/dc* values as the measured one at each temperature range. It has been reported that, in the process of DPPC vesicles being heated up through the $T_m$ of DPPC, the solution *dn/dc* has a sudden drop, which is related to bilayer volume swelling and bilayer density and thickness reducing at the phase transition.[23] The *dn/dc* decreasing with temperature increasing has been observed in a more linear trend in the negatively charged DMPG dispersion system.[24] If the lipid assemblies remain their size and shape with heating up, the scattered light intensity of the solution should follow the change of *dn/dc* at the different temperatures as the relationship appears in the Rayleigh scattering approximation (Eqn. 4.3.2).

The ratio of $(dn/dc)^2$ of the DPPC/DHPC/DPPG/DSPE-PEG2000 bicelles at 31 and 60 °C is about 1.44, which means the scattered intensity ratio $I_{31°C}/I_{60°C}$ should also be 1.44 for the same system without solute molecular weight changing. In Figure 4.3.9, the 3 and 5 mol% DSPE-PEG2000 have the scattered intensities before/after heating up ratios are 320/230=1.4 and 130/96=1.35, which are quite close to the $(dn/dc)^2$ of the bicelles at 31/ 60 °C. The correlations of intensity and $(dn/dc)^2$ ratios indicate the molecular weight of 3 and 5 mol% PEG2000-DSPE systems didn't change as temperature increasing from 25 to 60 °C. The increase of the scattered intensities of the NON-PEG and 0.5% DSPE-PEG 2000 bicelles at 60 °C are presumably caused by the larger molecular weight of solute particles forming through disc coalescence. In the bicelles with 1 mol% DSPE-PEG2000, the scattered light intensity decreased right after reaching

60 °C, then slowly increased. The reason behind could be the slow annealing of discs at the high temperature.

In the combination of DLS, TEM and SAXS results we can conclude that the disc-to-vesicle transition in the DPPC/DHPC/DPPG bicellar mixture without any PEGylated lipids can happen immediately with the temperature jump from 25 to 60 °C above the $T_m$ of DPPC. The additional DSPE-PEG in the bicellar mixture can slow down the disc coalescence at high temperature thus to achieve high thermal stability.

### 4.3.4 The PEGylation v.s. Charge Function in Bicelle Systems

The zwitterionic DPPC/DHPC bicellar discs are not stable and becoming MLVs in dilute condition.[25] DPPG has been added and proved to stabilize the DPPC/DHPC disc structure at $C_{lp}$ = 1 mg/mL.[14] Both the DPPG and the DSPE in DSPE-PEG are negatively charged in headgroup. To differentiate the DSPE-PEG from DPPG on contributions of stabilizing the bicellar discs in the low concentration, a series studies of the *Q-ratio* =3 $C_{lp}$=5 mg/mL DPPC/DHPC with 5 mol% DSPE-PEG2000 without DPPG have been conducted and compared with the bicelles with DPPG. The SAXS patterns of the PEGylated bicelles in the presence and absence of DPPG at 25 °C have been found quite similar and can overlap each other. [Figure 3=4.3.11(a)] The TEM micrograph of the NO-DPPG bicelle shows the planar and rim part of discs. [Figure 3=4.3.11(b)] The SAXS and TEM of DPPC/DHPC/DSPE-PEG2000 results provide the firm support for the 5 mol% DSPE-PEG2000 discs can maintain their size and shape stability in the dilute condition

and don't need extra negatively charged long-chain lipids. Whether the other PEG ratios and chain lengths bicelles can also have uniform discs is still needed to test.

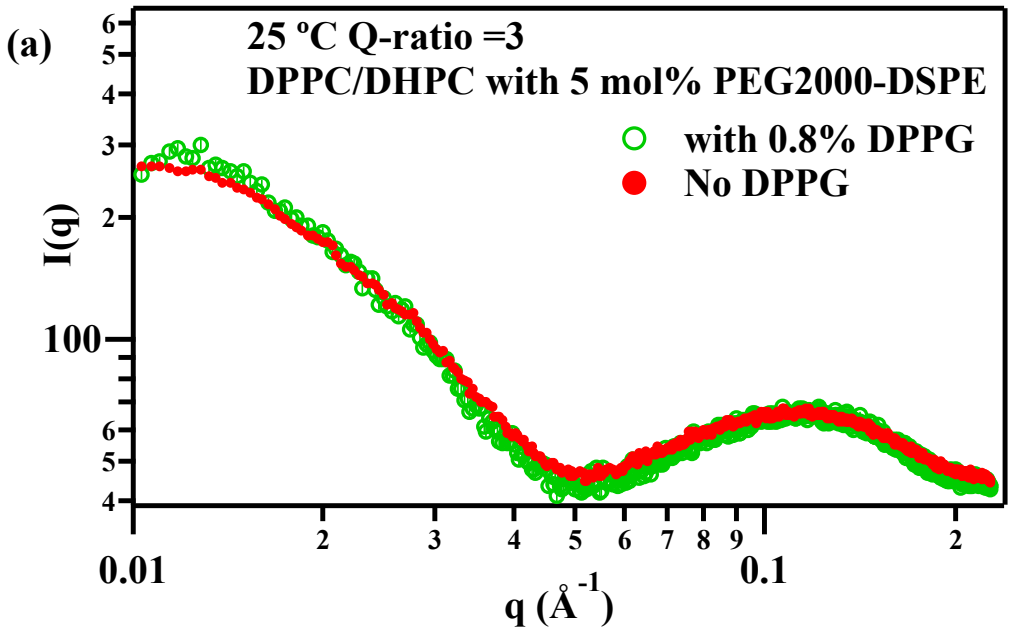


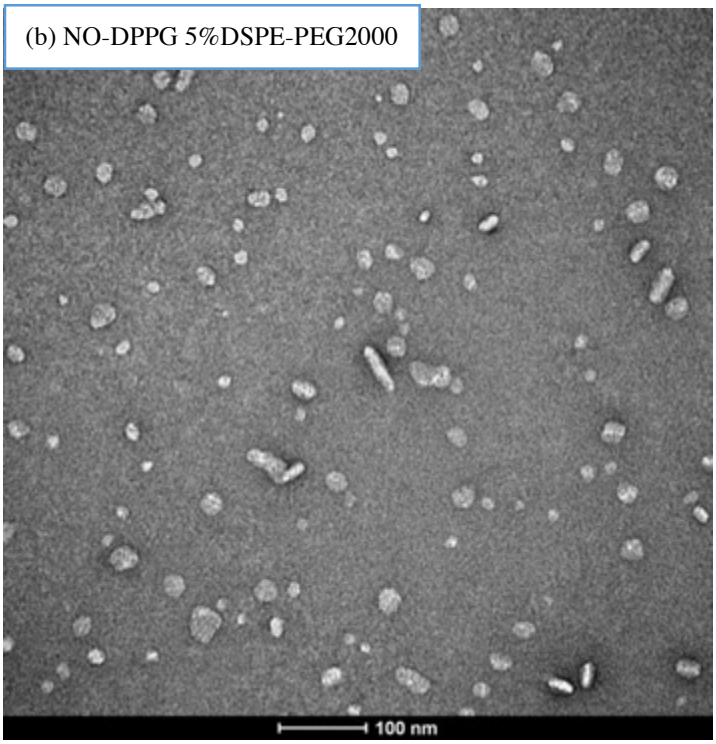

**Figure 4.3.11** (a) SAXS profiles of *Q-ratio* = 3 $C_{lp}$ = 5 mg/mL T=25 °C DPPC/DHPC with 5 mol% DSPE-PEG2000 bicellar mixture with 0.8 mol% DPPG (open circles) and in the absence of DPPG (dots). (b)TEM picture of the *Q-ratio* = 3 $C_{lp}$ = 5 mg/mL T=25 °C DPPC/DHPC with 5 mol% DSPE-PEG2000 bicellar mixture without 0.8 mol% DPPG

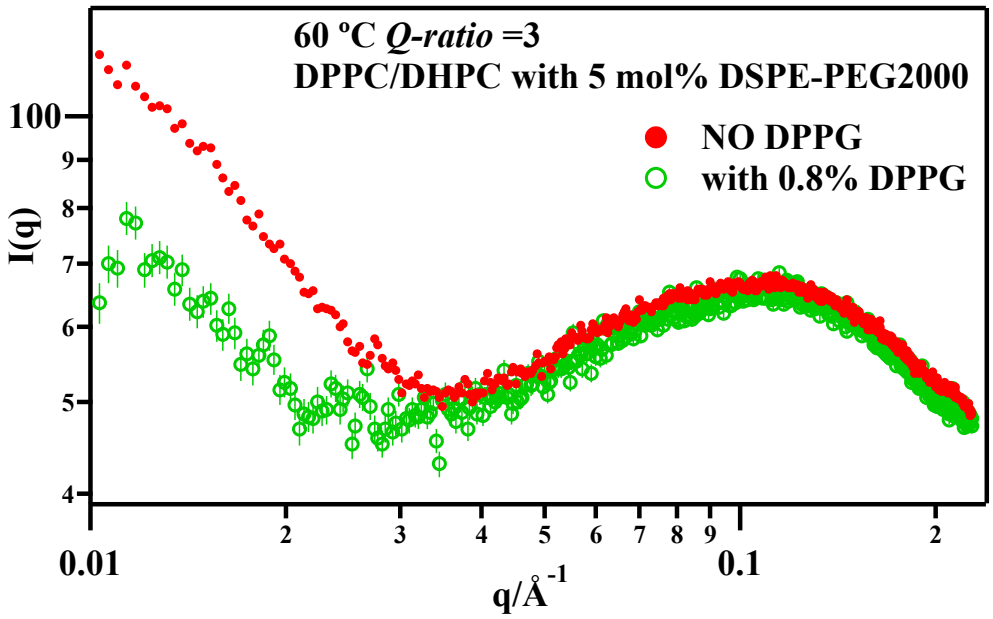


**Figure 4.3.12** SAXS profiles of *Q-ratio* = 3 $C_{lp}$ = 5 mg/mL T=60 °C DPPC/DHPC with 5 mol% DSPE-PEG2000 bicellar mixture with 0.8 mol% DPPG (open circles) and in the absence of DPPG (dots).

The PEGylated bicelles in the presence and absence of DPPG have been heated up from 25 to 60 °C. (Figure 4.3.12) The 60 °C SAXS patterns of the PEGylated bicelles in the absence of DPPG has a relative higher intensity in the *q*-range 0.01 to 0.03 $Å^{-1}$ than the one with 0.8 mol% of DPPG. The broad bilayer peaks of both samples are almost the same in the *q*-range 0.04 to 0.24 $Å^{-1}$. The difference of the low-*q* intensities between the bicelles in the presence and absence of DPPG is possibly caused by the larger aggregations forming in the DPPC/DHPC/DSPE-PEG2000 system but not in the system with DPPG.

As mentioned in 4.3.1, the repulsion between bicellar discs generated by DSPE-PEG are the electrostatic repulsive force from DSPE headgroups and the steric force from PEG corona. At the

high temperature, the PEG chain lost the bonded water resulting a great reduction in the steric force.[26] Thus the reason for the high-T SAXS I($q$) for bicelles in the presence of DPPG is lower intensity than for the bicelles in the absence of DPPG is that the electrostatic repulsion inhibited the discs coalescence into larger aggregations. Even being reduced at high-T, the steric repulsion may still exist on the particles. Further experiments of the bicelle systems in salt solution may show the steric effect where the charges should be screened out.

To obtain the surface charge amount on discs, the zeta potential measurements of different bicelle systems have been conducted (Table 4.3.4). The $R$ = 0.05 sample (2) has five times more negatively charged DPPG than the $R$ = 0.01 sample (1). The zeta potentials of these two samples are not five times in difference. Presumably, the surface charge amount is related to the size of particles in (2) is smaller than in (1) and the charge distribution is around disc-shaped surface instead of spherical surface. The sample of $Q$-ratio=3 $R$=0.05 5 mol% DSPE-PEG2000 DPPC/DHPC/DPPG shows a lower zeta potential than the $R$=0.05 100 mg/ml DPPC/DHPC/DPPG in the absence of DSPE-PEG. Presumably, the decrease of zeta potential with 5 mol% DSPE-PEG2000 is a result of the friction increase from PEG chain on the particles surface.[27]

**Table 4.3.4** Zeta potential results of different bicellar systems

| samples | Average Zeta Potential/mV |
|---|---|
| (1) $Q$-ratio=3 $R$=0.01 100 mg/ml DPPC/DHPC/DPPG | -13.4±1.1 |
| (2) $Q$-ratio=3 $R$=0.05 100 mg/ml DPPC/DHPC/DPPG | -28.9±0.9 |
| (3) $Q$-ratio=3 $R$=0.05 25 mg/ml 5 mol% DSPE-PEG2000 DPPC/DHPC/DPPG | -20.6±3.5 |

### 4.3.5 Excess DSPE-PEG in Bicelles

Excess DSPE-PEG components can deplete the bicellar discs formation and the related phase transitions. 10 mol% DSPE-PEG750 have been incorporated in the *Q-ratio* = 3 *R* = 0.01 DPPC/DHPC/DPPG aqueous solution. Some elongated structures mixed with spherical shapes are spotted in the TEM Figure 4.3.13.

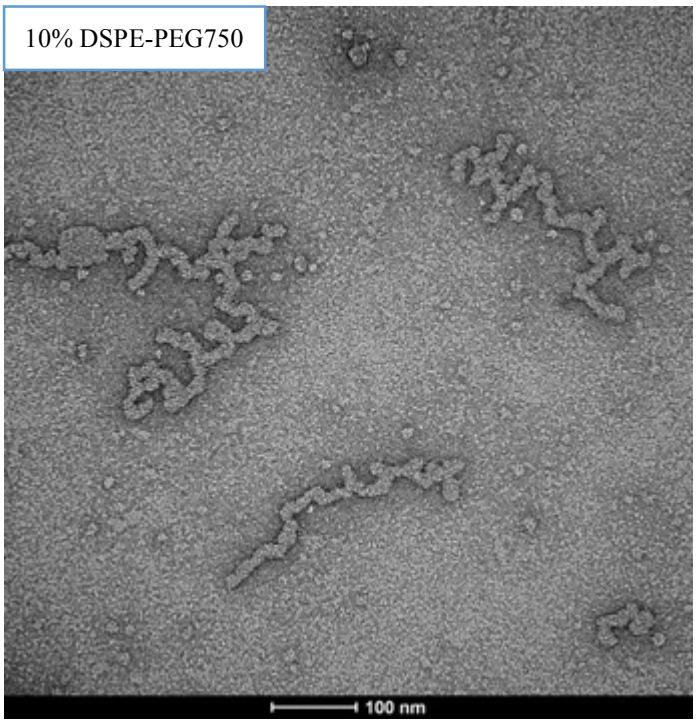


**Figure 4.3.13** Negative staining TEM of *Q-ratio* = 3 *R* = 0.01 DPPC/DHPC/DPPG with 10 mol% DSPE-PEG750 at T = 25 °C.

The small spherical shapes can be seen and considered as the planar part of discs or the spherical micelles. The larger structures look like the "ribbon" or "worm-like" micelles as their widths are comparable to the diameter of small discs/micelles. One origin of the ribbon formation is the highly surface charge from DSPE. The total charge ratio of the system [DPPG]+[DSPE-PEG750]/[TOTAL LIPIDS] is about 10%. However, the disc-forming system

*Q-ratio* = 3 *R* = 0.05 DPPC/DHPC/DPPG with 5 mol% DSPE-PEG2000 also has a 10% charge ratio (Chapter 3).[14] So the highly charge shouldn't be the reason for ribbon formation. Another possibility is the high-density PEG750 corona on the assembly surface promoted the ribbon structure. Similar DPPC/DSPE-PEG2000 and EPC/DSPE-PEG5000 "worm-like" micelles have been reported in literature, which was explained by long-chain lipids forming bilayer and DSPE-PEG minimizing the high curvature energy.[2, 28]

The "ribbon" micelles have also been proposed as an intermediate state during disc-to-vesicle and disc-to-lamella transitions.[29, 30] Pluronics are a type of block copolymer containing the hydrophilic PEG blocks and the hydrophobic polypropylene glycol (PPG) blocks. It's been reported that the ribbon structure appeared in 250 mg/mL DMPC/DHPC bicelles with 0.4 mol% Pluronic 68 PEG-PPG-PEG triblock copolymer.[31] The role of the Pluronic may be underestimated in the ribbon formation. Similar as DSPE-PEG, the Pluronic 68 should have the hydrophobic parts inserting the bilayer and the PEG hydrophilic ends floating in the water.

## 4.4 Discussion

### 4.4.1 The Effect of DSPE-PEG on the Bicellar Discs Formation

The findings in the Results shows DSPE-PEG can reduce the bicellar discs radii and influence the thermal stability. Based on the DSPE-PEG configuration and property, the driving force of the disc size reduction can be from (1) the charged DSPE (2) PEG corona (3) the high curvature packing property of the DSPE-PEG.

Firstly, negatively charged long-chain lipids such as DMPG and DPPC have been proved to reduce the disc size.[32] In the high concentration bicelles, the structure factors representing strong inter-particle interactions have been found in the high DSPE-PEG ratio samples.[Figure 4.3.1(a)] In the dilute 5 mg/mL condition, the disc radii had a significant reduction from 20 nm to 10 nm induced by only 0.5 mol% more DSPE-PEG750 or DSPE-PEG2000 in the *Q-ratio* = 3 *R* = 0.01 DPPC/DHPC/DPPG bicelles (SAXS fitting results in Table 4.3.1 and Table 4.3.2 ). In the higher charge ratio *Q-ratio* = 3 *R* = 0.02 DPPC/DHPC/DPPG system without any DSPE-PEG, 13-15 nm radius discs have been observed. Furthermore, there's almost no difference in the SAXS patterns of the bicelles in the absence and presence of 0.8 mol% DPPG [Figure 4.3.11(a)] the *Q-ratio* = 3 $C_{lp}$ = 5 mg/mL *T*=25 °C DPPC/DHPC/5 mol% DSPE-PEG2000 bicelles]. So, the charge from DSPE-PEG is not the determining factor for the size of bicellar discs and aggregations.

Secondly, the hydration force from PEG can be explained through the PEG molecular configuration, which are the "mushroom" Gaussian random coil at a low density and the condensed "brush" at a high density. The limit of the mushroom to brush configuration transition is that the PEG chains are starting to interact with each other. For PEG 750, 2000 and 5000 on the bilayer surface, the mushroom to brush transition ratios are 4.5 mol%, 1.4 mol% and 0.5 mol%.[33] Thus the large aggregations happened in the 0.5 mol% DSPE-PEG 5000 bicelles may be induced by the PEG "brush" [Figure 4.3.6 (a)]. However, it's still hard to explain that the 1 mol% DSPE-PEG 5000 DPPC/DHPC/DPPG can still form discs. We should turn to the classic packing method to find the key.

The packing parameters of PEGylated phospholipids are ~ 1/3 for the bulk PEG covalently bonded headgroups. Based on the critical packing parameter theory[15], the DSPE-PEG should form a highly curved rim as DHPC in the bicellar discs. In this case, the *Q-ratio* should be adjusted as

$$Q\text{-}ratio_{adj} = \{[DPPC]+[DPPG]\}/\{[DHPC]+[DSPE\text{-}PEG]\} \qquad \text{(Eqn. 4.4.1)}$$

The $Q\text{-}ratio_{adj}$ for the *Q-ratio* = 3 $R$ = 0.01 DPPC/DHPC/DPPG bicelles with 0.5 mol%, 1 mol% and 5 mol% DSPE-PEG are adjusted to 2.92, 2.84 and 2.3 respectively. Even though the ideal bicelle size and *Q-ratio* relationship cannot work for the charged discs, the disc size reduction by DSPE-PEG can still be rationalized by more rim forming materials adding in the mixture.

The hypothesis of the PEGylated bicellar discs formation is that: in the ratio of 0.5% DSPE-PEG, the bicellar discs have a random PEG distribution on their surfaces – both the rim and the surface region. For DSPE-PEG750 and 2000, the PEG chains are in the "mushroom" regime and not interacting with each other. For the DSPE-PEG5000, it reaches the "brush" regime. The lateral pressure among the PEG chains on the bilayer surface may loosen off the compact discs and the force at the rim part cannot compete thus coalesces happen to minimize the free energy from the exposed hydrophobic parts. In a little higher ratio -1 mol% PEGylated lipids in bicelles, more DSPE-PEG5000 may come to the rim part of the discs and compete with the lateral pressure from the planar part, thus stabilize the morphology and size of discs. The size similarity of the discs with 0.5 mol%, 1 mol% and 5 mol% DSPE-PEG750 and DSPE-PEG2000 at $C_{lp}$ = 5 mg/mL is also assumed as a result of most of the DSPE-PEG locating on the disc rim by their

packing properties. In the ratio of 10 mol% DSPE-PEG750, the lateral tension of the bilayer rim may be too high to confine in the small discs, which lead to the formation of the ribbon-like micelles.

### 4.4.2 The Effect of DSPE-PEG on the Bicellar Thermal Stability

When the charged bicelle is heated up through the $T_m$ of the long-chain lipids, the disc-to-lamella transition is supposed to happen. The additional DSPE-PEG in the 100 mg/mL concentrated bicelles didn't interfere this process until 5 mol% DSPE-PEG5000. The exclude volume effect on the assemblies' surface is believed to inhibited the lamella formation. At low-$C_{lp}$, temperature-dependent disc-to-vesicle transition can happen in the NON-PEG bicelles. 0.5 mol% DSPE-PEG750 and 2000 in bicelles can disrupt the transition process and have larger irregular aggregations forming. More than 1 mol% DSPE-PEG significantly slowed down the vesicle formation and can stabilize the disc morphology up to hours at the high temperature. The thermal stability is assumed to be enhanced by the electrostatic force and steric force induced by DSPE-PEG. Within the same PEG ratio, the bicelles persisting more charge show the lower SAXS intensity than the less charged one in Figure 4.3.12. The SAXS intensity comparison is a shred of evidence for the thermal stability enhanced by electrostatic interactions. For the steric force, it's obvious that only 0.5-1 mol% DSPE-PEG can inhibit the vesicle formation. To fully differentiate the electrostatic force and steric force contribution to the bicelles' thermal stability, further tests in the PEG and non-PEG bicelles at high temperature will be helpful.

## 4.5 Conclusion

Uniform PEGylated bicellar nanodiscs can be obtained in the aqueous solutions of DPPC/DPPG/DHPC/DSPE-PEG2000 through one-step self-assembly method. The DSPE-PEG can serve as the rim stabilizer and the bilayer building block, which is the determine factor for the disc size. The disc size reduction and thermal stability improvement are assumed to be from the electrostatic repulsion and steric effect induced by the DSPE-PEG in the mixture. This study provides the DSPE-PEG ratio limits for the PEGylated bicellar discs formation. The knowledge paves the way for the future applications of the bicellar structures.

## 4.6 References


1. D. Lasic, R. Joannic, B. Keller, P. Frederik and L. Auvray, Advances in colloid and interface science **89**, 337-349 (2001).
2. M. Johnsson and K. Edwards, Biophysical Journal **85** (6), 3839-3847 (2003).
3. H. Lee and R. W. Pastor, The Journal of Physical Chemistry B **115** (24), 7830-7837 (2011).
4. H. Du, P. Chandaroy and S. W. Hui, Biochimica et Biophysica Acta (BBA)-Biomembranes **1326** (2), 236-248 (1997).
5. C. D. Walkey, J. B. Olsen, H. Guo, A. Emili and W. C. Chan, Journal of the American Chemical Society **134** (4), 2139-2147 (2012).
6. P. Kingshott and H. J. Griesser, Current Opinion in Solid State and Materials Science **4** (4), 403-412 (1999).
7. V. P. Torchilin, Pharmaceutical research **24** (1), 1-16 (2007).
8. O. Garbuzenko, Y. Barenholz and A. Priev, Chemistry and physics of lipids **135** (2), 117-129 (2005).
9. R. Gref, M. Lück, P. Quellec, M. Marchand, E. Dellacherie, S. Harnisch, T. Blunk and R. Müller, Colloids and Surfaces B: Biointerfaces **18** (3), 301-313 (2000).
10. K. Hristova, A. Kenworthy and T. J. McIntosh, Macromolecules **28** (23), 7693-7699 (1995).
11. M.-D. Duong-Thi, M. Bergström, K. Edwards, J. Eriksson, S. Ohlson, J. T. Y. Ying, J. Torres and V. A. Hernández, Analyst **141** (3), 981-988 (2016).
12. M. M. Zetterberg, K. Reijmar, M. Pränting, Å. Engström, D. I. Andersson and K. Edwards, Journal of Controlled Release **156** (3), 323-328 (2011).
13. W. Zhang, J. Sun, Y. Liu, M. Tao, X. Ai, X. Su, C. Cai, Y. Tang, Z. Feng, X. Yan, G. Chen and Z. He, Molecular Pharmaceutics **11** (10), 3279-3290 (2014).
14. Y. Liu, M. Li, Y. Yang, Y. Xia and M.-P. Nieh, Biochimica et Biophysica Acta (BBA) - Biomembranes **1838** (7), 1871-1880 (2014).
15. J. N. Israelachvili, *Intermolecular and surface forces: revised third edition*. (Academic press, 2011).
16. I. G. Denisov, M. A. McLean, A. W. Shaw, Y. V. Grinkova and S. G. Sligar, The Journal of Physical Chemistry B **109** (32), 15580-15588 (2005).
17. K. A. Riske, L. Q. Amaral and M. T. Lamy-Freund, Biochimica et Biophysica Acta (BBA)-Biomembranes **1511** (2), 297-308 (2001).
18. J. F. Nagle and M. C. Wiener, Biochimica et Biophysica Acta (BBA) - Biomembranes **942** (1), 1-10 (1988).
19. S. Mahabir, W. Wan, J. Katsaras and M.-P. Nieh, Journal of Physical Chemistry B **114** (17), 5729-5735 (2010).
20. M.-P. Nieh, C. J. Glinka, S. Krueger, R. S. Prosser and J. Katsaras, Biophysical journal **82** (5), 2487-2498 (2002).
21. R. Soong and P. M. Macdonald, Biochimica et Biophysica Acta (BBA) - Biomembranes **1768** (7), 1805-1814 (2007).

22. S. Mahabir, D. Small, M. Li, W. Wan, N. Kučerka, K. Littrell, J. Katsaras and M.-P. Nieh, Biochimica et Biophysica Acta (BBA) - Biomembranes **1828** (3), 1025-1035 (2013).
23. P. N. Yi and R. C. MacDonald, Chemistry and Physics of Lipids **11** (2), 114-134 (1973).
24. K. A. Riske, M. J. Politi, W. F. Reed and M. T. LamyFreund, Chemistry and Physics of Lipids **89** (1), 31-44 (1997).
25. G. Rodríguez, G. Soria, E. Coll, L. Rubio, L. Barbosa-Barros, C. López-Iglesias, A. M. Planas, J. Estelrich, A. De la Maza and O. López, Biophysical journal **99** (2), 480-488 (2010).
26. J. Israelachvili, Proceedings of the National Academy of Sciences **94** (16), 8378-8379 (1997).
27. K. Arnold, O. Zschoernig, D. Barthel and W. Herold, Biochimica et Biophysica Acta (BBA)-Biomembranes **1022** (3), 303-310 (1990).
28. L. Arleth, B. Ashok, H. Onyuksel, P. Thiyagarajan, J. Jacob and R. P. Hjelm, Langmuir **21** (8), 3279-3290 (2005).
29. M.-P. Nieh, V. A. Raghunathan, C. J. Glinka, T. A. Harroun, G. Pabst and J. Katsaras, Langmuir **20** (19), 7893-7897 (2004).
30. J. Leng, S. U. Egelhaaf and M. E. Cates, Biophysical journal **85** (3), 1624-1646 (2003).
31. R. Soong, M.-P. Nieh, E. Nicholson, J. Katsaras and P. M. Macdonald, Langmuir **26** (4), 2630-2638 (2009).
32. A. Hu, T.-H. Fan, J. Katsaras, Y. Xia, M. Li and M.-P. Nieh, Soft Matter **10** (28), 5055-5060 (2014).
33. D. Marsh, R. Bartucci and L. Sportelli, Biochimica et Biophysica Acta (BBA)-Biomembranes **1615** (1), 33-59 (2003).

# Chapter 5

# Supramolecular Structures in the Mixture of Bicelles and Reverse Pluronic Polymers

## 5.1 Introduction

The Pluronic® block copolymers of Polyethylene Glycol (PEG) and Polypropylene Glycol (PPG) constitute various of surfactants and have widespread application in different areas, especially for biomedical applications.[1-3] The chemical structure of the PEG-PPG-PEG Pluronics is shown in Figure 5.1.1. With the PEG end subunits, Pluronics can be used as the cheaper substitute for the PEGylated lipids in therapeutic formulations and have the steric stabilization of the assembled structures as well.[4, 5] Particular interest has been put on investigations of the interactions of Pluronics with lipid assemblies, for understanding the function of Pluronics on cell membrane and the carriers' formulation.[6-8]

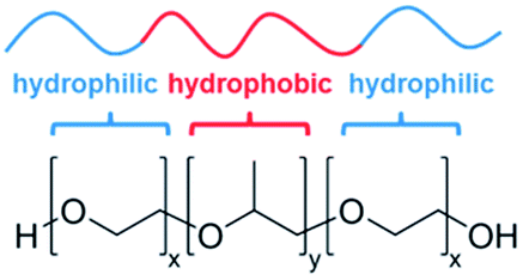


**Figure 5.1.1** PEG-PPG-PEG Pluronic triblock copolymer structure. x and y are the numbers of repeat unites.

Even though the reverse Pluronics in the configuration of PPG−PEG−PPG have not been explored as broad as Pluronics, they have been attracting particular attentions in the theoretical and applicable aspects in recent research studies.[9-14]

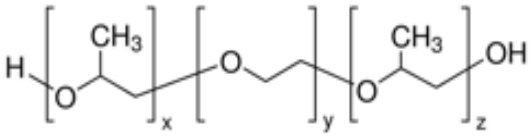


**Figure 5.1.2** PPG-PEG-PPG reverse Pluronic triblock copolymer structure. x, y, z are the numbers of repeat unites.

Very few studies focused on the Pluronics functions in the bicelle membrane model system.[15] The reverse Pluronics and bicelle mixture hasn't been explored. It is valuable to reveal the mystery realm of the fundamental science and applications of Pluronic and bicellar mixtures system, such as the interaction of Pluronic and cell membrane and advanced supramolecular structures.

In this chapter, I studied the mixture of reverse Pluronics and phospholipid bicelles. The assembled structures have been observed via small angle scattering and transmission electron microscopy techniques. Dynamic light scattering is the tool for the kinetics monitoring.

## 5.2 Materials and Methods

### 5.2.1 Materials and sample preparation

Zwitterionic DPPC and DHPC and negatively charged DPPG were purchased from Avanti Polar Lipids (Alabaster, AL) and used without further purification. Triblock copolymer $PPG_{14}$-

$PEG_{24}$-$PPG_{14}$ (Molecular Weight 2700) was purchased from Sigma-Aldrich. We will use the name P 17R4 for this polymer. Filtered D.I. Water was used as solvent for sample preparation. The compositions are listed below:

*Q-ratio* = [DPPC+DPPG] / DHPC =3

*R* = DPPG / [DPPC+DPPG] = 0.01

Lipids to P 17R4 molar ratio depends on the experimental setting.

The weighted lipid powder was first weighted and then dispersed in the filtered D.I. water (or $D_2O$ for SANS) to form stock solutions with an initial total lipid concentration ($C_{lp}$) of 10 wt%. After successive vortex and temperature cycling between 25 and 60 °C, the lipid stock solutions were homogenously dissolved in all cases (transparent at room temperature and below). P 17R4 was weighted and dissolved in D.I. water (or $D_2O$ for SANS) to the needed concentrations ($C_{polymer}$). After 12 hours stirring, the P 17R4 solutions were filtered through membrane with 200 nm pore before usage. The lipid stock solutions were then progressively diluted in P 17R4 solution at room temperature.

## 5.3 Results

### 5.3.1 P 17R4 Solution

To investigate the nature of the interaction of amphiphilic, nonionic PPG-PEG-PPG P 17R4 triblock copolymers with lipid nanodiscs, SANS, SAXS, DLS, and negative staining TEM characterization techniques were used in the condition of varying lipid concentration and P 17R4 concentration. In this chapter, $C_{lp}$ stands for lipid concentration

and $C_{polymer}$ is for P 17R4 concentration.

The polydispersity of the purchased P 17R4 is 1.1 from Gel Permeation Chromatography measurement, which means the P 17R4 unimers can be considered the same in molecular structure. The hydrodynamic radii($R_H$) of particles in P 17R4 solutions from 0.5 to 9 wt% were monitored by DLS. The $R_H$ distribution are showed in Figure 5.3.1. We observed that the major $R_H$ peaks were 1.5-1.6 nm for most of the solutions and some big aggregations appear with the $C_{polymer}$ increase. After 200 nm membrane filtration, all of the samples exhibited a single $R_H$ peak around 1.5 nm.

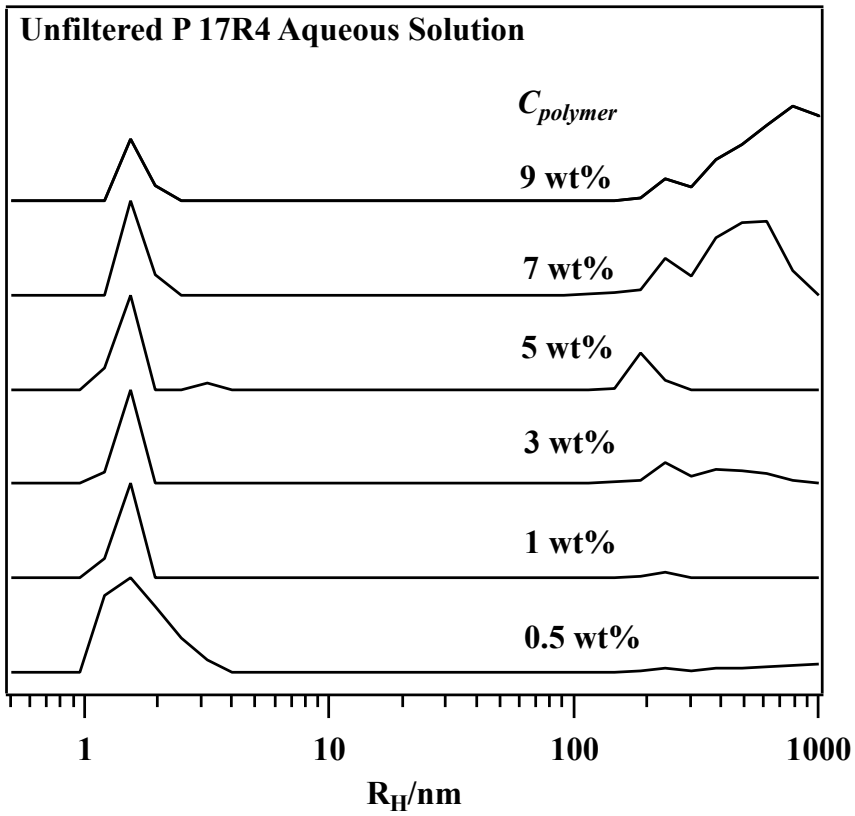


**Figure 5.3.1** Hydrodynamic radii distributions of P 17R4 solutions in different concentrations. The solutions were made in the method of direct dissolving weighted polymers in D.I. water without further dilution.

The radii of gyration ($R_g$) of the filtered P 17R4 solutions $C_{polymer}$ = 0.1 wt% and 0.5 wt% were measured through SANS. The solvent was $D_2O$ instead of $H_2O$ for SANS measurements. The SANS patterns and the Guinier-Porod fitting results are shown in Figure 5.3.2. The $R_g$ values are 1.3±0.1 nm for $C_{polymer}$ = 0.1 wt% and 1.4±0.1 nm for $C_{polymer}$ = 0.5 wt%. These results are consistent with the former reported 1.3 nm $R_g$ of 0.95 wt% P 17R4.[12] We can assume that the P 17R4 solutions lower than 0.95 wt% mainly have individual unimers in aqueous solutions.

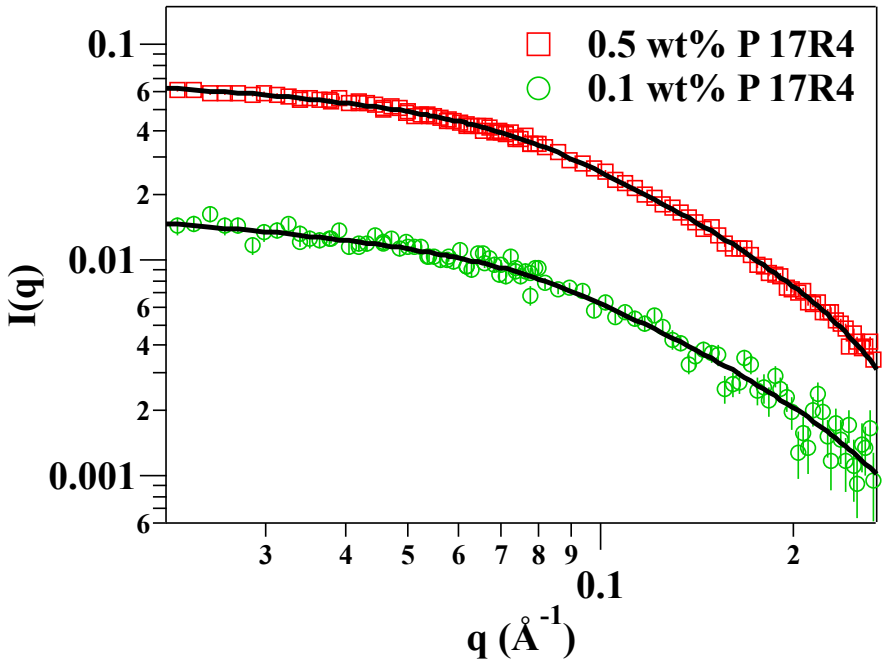


**Figure 5.3.2** SANS data for P 17R4 solutions at 25 °C with concentrations $C_{polymer}$ = 0.1 wt% (open circle) and 0.5 wt% (open square) with Guinier-Porod fitting curves appeared as black curves on each data.

### 5.3.2 $R$ = 0.01 $C_{lp}$ = 0.5 wt% Bicelles in P 17R4 Solution

The $C_{lp}$ = 10 wt% *Q-ratio* = 3 $R$ = 0.01 DPPC/DHPC/DPPG lipid aqueous dispersions were diluted into $C_{lp}$ = 0.5 wt% at room temperature. The used solvents are $D_2O$, $C_{polymer}$ = 0.1 wt%($D_2O$) and $C_{polymer}$ = 0.5 wt% ($D_2O$) P 17R4 solutions respectively. The dilutions were conducted at the same day from the same $C_{lp}$ = 10 wt% stock solution.

The $R_H$ of the particles in $C_{lp}$ = 0.5 wt% in $C_{polymer}$ = 0.1 wt% and in $C_{polymer}$ = 0.5 wt% P 17R4 at different days after dilution were monitored through DLS and showed in Figure 5.3.3. Both of the systems have the $R_H$ growth from 8-10 nm to about 30-50 nm within 11 days. However, DLS cannot give the morphological of the solute particles. The SANS and TEM tools have been used to get the morphology and size of the lipids and P 17R4 assembled particles in the aqueous solutions.

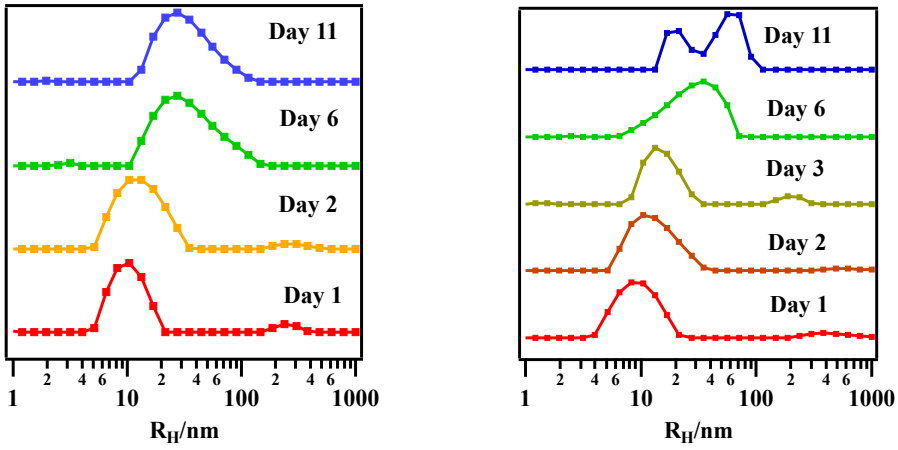


**Figure 5.3.3** Hydrodynamic radii ($R_H$) from DLS of *Q-ratio* = 3 $R$ = 0.01 $C_{lp}$ = 0.5 wt% DPPC/DHPC/DPPG bicelles in P 17R4 solutions at 25 °C (a) $C_{polymer}$ = 0.1 wt% (b) 0.5 wt% at different days after dilution from $C_{lp}$ = 10 wt% stock solution.

Figure 5.3.4(a) shows the SANS measurements and fitting results of the three *Q-ratio* = 3 $R$ = 0.01 DPPC/DHPC/DPPG solutions 11 days after dilution. The measurement

temperature was at 25 °C. The curves from bottom to top are the $C_{lp}$=0.5 wt% in $D_2O$, in $C_{polymer}$ = 0.1 wt% and $C_{polymer}$ = 0.5 wt% respectively. The factors of 10 and 100 have been applied to the curves for visual clarity. Figure 5.3.2 (b), (c) and (d) have the relevant TEM pictures of the three different samples at the same day of SANS measurements.

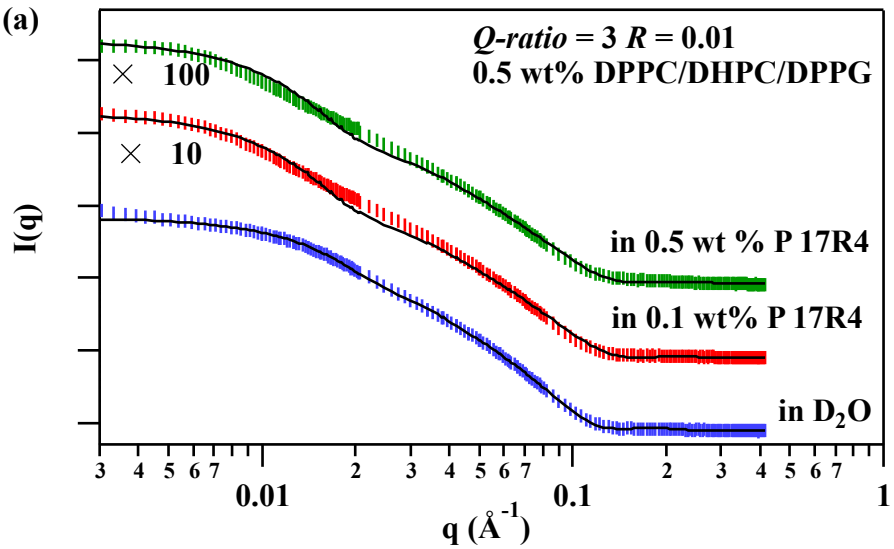


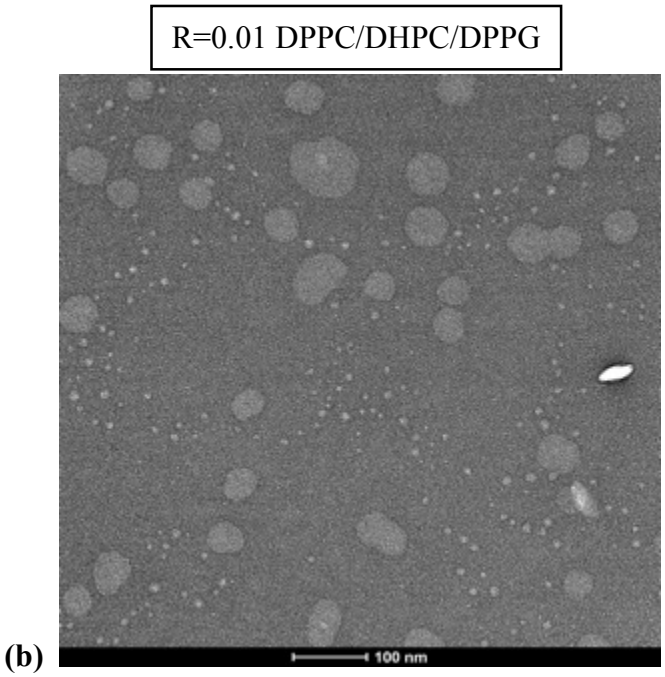

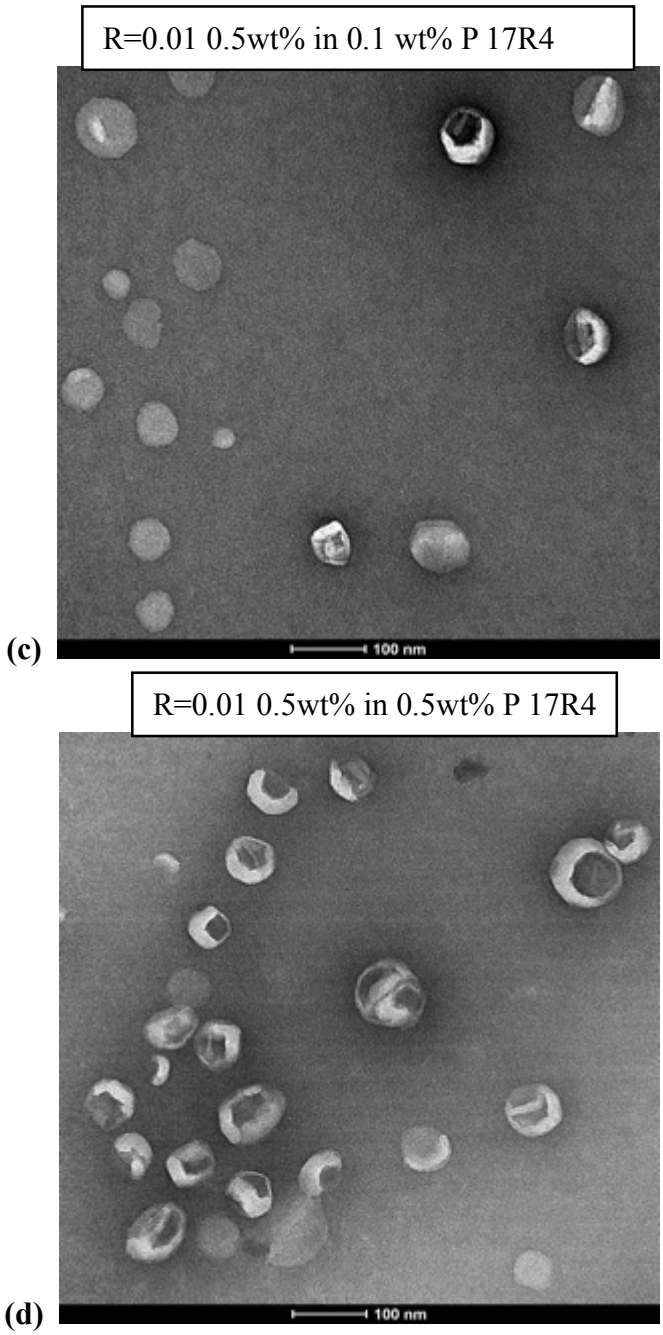


**Figure 5.3.4** (a) SANS profiles of *Q-ratio* = 3 *R* = 0.01 $C_{lp}$ = 0.5 wt% DPPC/DHPC/DPPG $D_2O$ solutions at 25 °C in $D_2O$ (the bottom curve), in 0.1 wt% P 17R4 solution (the middle curve) and in 0.5 wt% P 17R4 solution (the top curve). A factor of 10 and 100 were applied to the SANS data with 0.1 wt% and 0.5 wt% P 17R4 solutions for a clear view. Negative staining TEM pictures of (b) 0.5 wt% bicelles diluted to 0.001wt%; (c) 0.5 wt% bicelles in 0.1wt% P 17R4 solution diluted to 0.001wt% lipid concentration; (d) 0.5 wt% bicelles in 0.5 wt% discs diluted to 0.001wt% lipid concentration.

In TEM pictures, the surface and rim of discs can be spotted in the *Q-ratio* = 3, *R* = 0.01 bicelles. In the TEM picture of the lipids and P 17R4 mixtures, the vesicular structures can be clearly seen. A certain ratio of large discs may also exist with these vesicles. Based on the TEM results and SANS curve behaviors, the polydisperse radius discs(PR-Disc) has been chosen to fit the $C_{lp}$ = 0.5wt% bicelles in $D_2O$ SANS curve and the polydispersed radius vesicle (PR-Vesicle) model has been selected to fit the $C_{lp}$ = 0.5wt% bicelles in $C_{polymer}$ = 0.1 wt% and 0.5 wt% P 17R4 solutions. The fitted SANS results are shown in Table 5.3.1. The bicellar disc is 15.4 nm in radius and 4.8 nm in thickness, the dimensions are consistent with the similar bicellar systems in chapter 3 and 4. For the vesicles in the bicellar mixture with $C_{polymer}$ = 0.1wt% and 0.5 wt% P 17R4 solutions, similar set of parameters can be used for both SANS curves, even though the sample with 0.1 wt% P 17R4 exhibits a little higher intensity than the one with 0.5 wt% at the very low-*q* range (0.003-0.005 $Å^{-1}$). A reasonable explanation of the fitting similarity is that 0.1 wt% P 17R4 is enough to induce the disc-to-vesicle transition in the *Q-ratio* = 3 *R* = 0.01 $C_{lp}$ = 0.5 wt% DPPC/DHPC/DPPG bicellar discs. The excess 0.4 wt% P 17R4 may stay as unimers in the solution.

**Table 5.3.1** SANS fitting results of the *Q* = 3 *R* = 0.01 $C_{lp}$ = 0.5 wt% DPPC/DHPC/DPPG

| *PR-Disc* | in $D_2O$ | *PR-Vesicle* | in $C_{polymer}$ = 0.1 wt% | in $C_{polymer}$ = 0.5 wt% |
|---|---|---|---|---|
| Radius (Å) | 153.6±3 | Core radius (Å) | 100±5 | 100±5 |
| Polydispersity | 0.2 | Polydispersity | 0.4 | 0.4 |
| Thickness (Å) | 48.2±2 | Shell thickness (Å) | 40.0±3 | 40.8±2 |
| Volume ($Å^3$) | $3.5\times10^6$ | Volume ($Å^3$) | $8.6\times10^6$ | $8.6\times10^6$ |

| **Table 5.3.2** Molar Concentrations and Ratios of the Lipids/P 17R4 mixed solutions | | |
|---|---|---|
| Samples in wt% | $C_{lp}$ = 0.5 wt%;<br>$C_{polymer}$ =0.1 wt% | $C_{lp}$ = 0.5 wt%;<br>$C_{polymer}$ =0.5 wt% |
| Sample in molar | $C_{lp}$ = 7.53 mM;<br>$C_{polymer}$ = 1.85 mM | $C_{lp}$ = 7.53 mM;<br>$C_{polymer}$ = 0.37 mM |
| Molar ratio | Lipid/P 17R4 = 20.35 | Lipid/P 17R4 = 4.07 |
| Assumption: 4000 lipids in one disc | Disc / P 17R4 = 1 / 200 | Disc / P 17R4 = 1 / 1000 |

A quantities analysis may be helpful to clarify the situation. The weight concentrations were converted to molar concentrations of the lipids/P 17R4 solutions (Table 5.3.2). According to the calculation, there should be about 200 P 17R4 unimers surrounding one disc in the $C_{lp}$ = 0.5 wt% and $C_{polymer}$ = 0.1 wt% solution and five times more in the $C_{lp}$ = 0.5 wt% and $C_{polymer}$ = 0.5 wt% solution. However, the number may be affected by the filtration in sample preparation.

At 40 days after the initial dilution, the stability of the solutions has been checked through SAXS. The SAXS profiles were collected at 25 °C on the SANS-characterized systems (a) $C_{lp}$ = 0.5 wt% with $C_{polymer}$ = 0.1 % and (b) $C_{lp}$ = 0.5 wt% with $C_{polymer}$ = 0.5 %. (Figure 5.3.5) The scattering pattern of the $C_{lp}$ = 0.5 wt% with $C_{polymer}$ = 0.1 % sample presents a peak ~ $q$ = 0.02 Å$^{-1}$, indicative of the form factor of unilamellar vesicles. The other broad peak from $q$ = 0.05 to 0.22 Å$^{-1}$ is mainly from the phosphate-phosphate distance in the phospholipid bilayer region. The $C_{lp}$ = 0.5 wt% with $C_{polymer}$ = 0.5 % SAXS curve in Figure 5.3.5 (b) shows the similar behavior as the one in (a). The Polydisperse

Core-Shell Vesicle (PCSV) model was used to fit both SAXS curves. The fitted results are shown in Table 5.3.3.

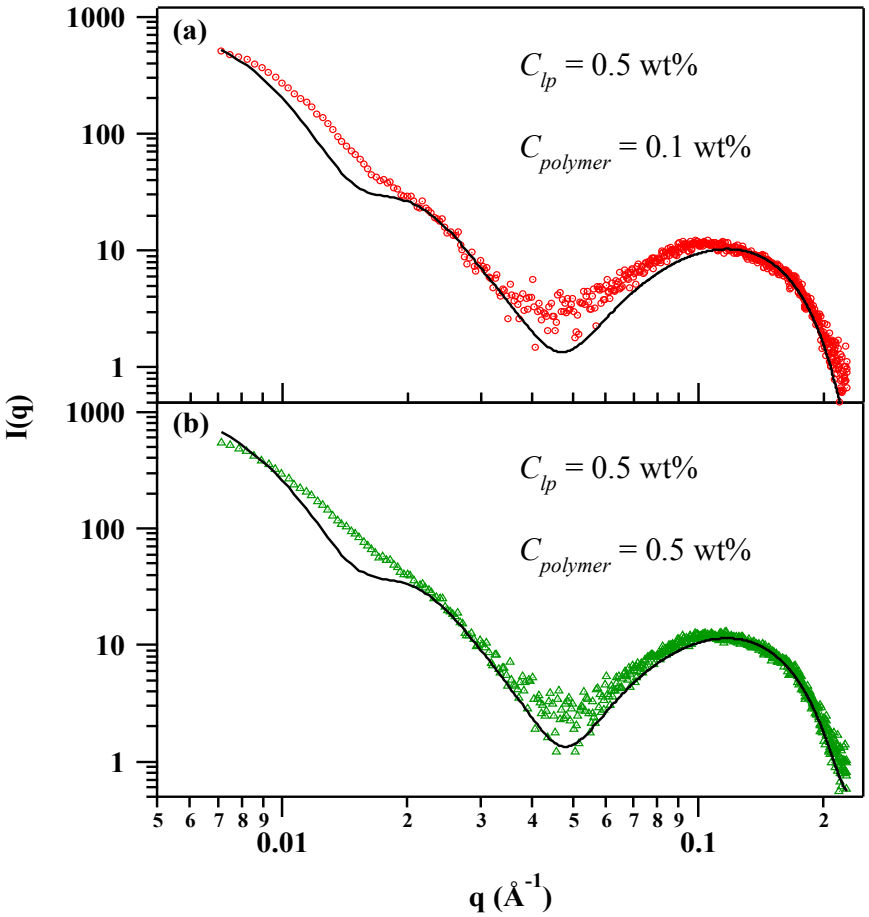


**Figure 5.3.5** SAXS profiles and Poly-Core-Shell-Vesicle fittings of bicelles at 40 days after dilution. *Q-ratio* = 3 *R* = 0.01 $C_{lp}$ = 0.5 wt% DPPC/DHPC/DPPG at 25 °C (a) in 0.1 wt% P 17R4 solution (b) in 0.5 wt% P 17R4 solution.

**Table 5.3.3** SAXS fitting results of the 40 days after dilution $Q$ = 3 $R$ = 0.01 $C_{lp}$ = 0.5 wt% DPPC/DHPC/DPPG in $D_2O$, $C_{polymer}$ = 0.1 wt% and 0.5 wt% P 17R4 solutions.

| Samples | $C_{lp}$ = 0.5 wt%; $C_{polymer}$ =0.1 wt% | $C_{lp}$ = 0.5 wt%; $C_{polymer}$ =0.5 wt% |
|---|---|---|
| Core Radius (Å) | 150 | 150 |
| Core Radius Polydispersity (0,1) | 0.3 | 0.3 |
| Inner Hydrophilic layer thickness (Å) | 9.5 ± 2 | 10.0 ± 2 |
| Hydrophobic layer thickness (Å) | 29.9 ± 4 | 29.4 ± 4 |
| Outer Hydrophilic layer thickness (Å) | 10.3 ± 3 | 10.9 ± 3 |

Compare the fitting data of the 40-day SAXS to the ones of 10-day SANS, we found the vesicles in both systems seemed to have a 5 nm increase in radii. However, the 5-nm difference is still in the polydisperse error range and may not reflect the real size increase. The thicknesses of the vesicles stayed the same around 5 nm and were considered as bilayer structures. It's worthy to mention that the 40 days DLS intensities of each lipid/P 17R4 mixed solution stayed the same as their intensities at 10 days after dilution. It may be an indication that the formed vesicles can keep the structural stability within 40 days after dilution.

### 5.3.3 $R = 0.01$ $C_{lp} = 0.1$ wt% Bicelles in P 17R4 Solution

To observe the effect of lipid concentration and polymer concentration on the polymer linkage between bicelles, DLS was used to monitor the systems with the lower lipid concentration and P 17R4 polymer concentration. The studied systems are: $C_{lp}$ = 0.1% in $C_{polymer}$ = 0.05%; $C_{lp}$ = 0.1% in $C_{polymer}$ = 0.05%; and the $C_{lp}$ = 0.1% in water. The $R_H$ changing after dilution from $C_{lp}$ = 10wt% are shown in Table 5.3.4.

The $R$ = 0.01 discs at low-$C_{lp}$ have a certain ratio of larger aggregations in the solution, which induced the second population of $R_H$. The population distribution of both $R_H$ has been put next to the peak values. At the beginning of the 1$^{st}$ day after dilution, the polymer mixed bicellar solution has already had a larger $R_H$ (12-14 nm) than the bare discs in water(9nm). The second $R_H$ populations of the three samples are comparably similar. In 7 days after dilution, both of the mixed solution had about 8 nm $R_H$ increase while the bare

discs only have 2 nm increase in $R_H$. From 7 to 45 then 66 days, the $R_H$ growth differences among the three samples are not obvious.

**Table 5.3.4** $R_H$ changing over days of the $Q$ = 3 $R$ = 0.01 $C_{lp}$ = 0.1 wt% DPPC/DHPC/DPPG in water, $C_{polymer}$ = 0.05 wt% and 0.25wt% wt% P 17R4 solutions.

| DAYS After dilution | $C_{lp}$ = 0.1% $C_{polymer}$ = 0.05% | | $C_{lp}$ = 0.1% $C_{polymer}$ = 0.25% | | $C_{lp}$ = 0.1% in water | |
|---|---|---|---|---|---|---|
| | $R_H$ peak 1 | $R_H$ peak 2 | $R_H$ peak 1 | $R_H$ peak 2 | $R_H$ peak 1 | $R_H$ peak 2 |
| 1 | 12.1(76%) | 362(24%) | 14(82%) | 302(18%) | 9.4(64%) | 450(36%) |
| 2 | 14.5(87%) | 200(13%) | 18(83%) | 754(17%) | 10.4(70%) | 436(30%) |
| 5 | 16.8(84%) | 144(15%) | 21.6(89%) | 631(11%) | 10.8(75%) | 245(25%) |
| 7 | 20.2(88%) | 636(12%) | 21.9(88%) | 570(12%) | 11.7(70%) | 502(30%) |
| 45 | 22(89%) | 536(11%) | 27(96%) | 1199(4%) | 12.8(82%) | 204(18%) |
| 66 | 25(92%) | 1294(8%) | 27.2(94%) | 347(4%) | 14(79%) | 522(21%) |

TEM micrograph of the $C_{lp}$ = 0.1 wt% and $C_{polymer}$ =0.05 wt% mixture on the 45-day is shown in Figure 5.3.6. There is no vesicle on the TEM captures, however, big aggregations can be clearly seen. The hydrophobic effect from P 17R4 is less in the diluted solution and cannot compete with the elastic energy on bicelles' surface. Nevertheless, the linkage between discs can still happen. The large aggregations contain discs close to each other from the edge part. Few "stacking" morphologies have been found in the sample. It may be caused by the linkage on the discs' surface.


**Figure 5.3.6** Negative staining TEM pictures of 0.1 wt% bicelles in 0.05% P 17R4 then diluted to 0.001wt%.

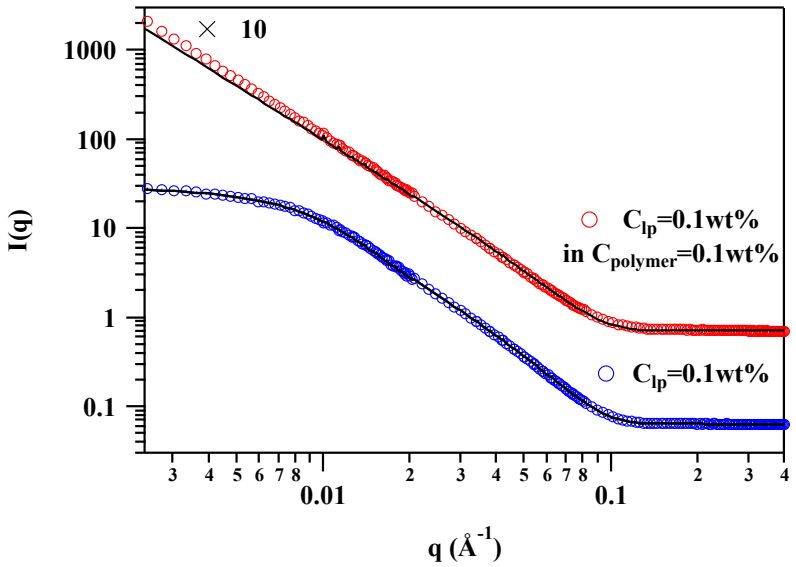


**Figure 5.3.7** SANS profiles of *Q-ratio* = 3 $R$ = 0.01 $C_{lp}$ = 0.1 wt% DPPC/DHPC/DPPG $D_2O$ solutions at 25 °C in $D_2O$ (the bottom curve) and in $C_{lp}$ = 0.1 wt% P 17R4 solution. A factor of 10 was applied to the SANS data with 0.1 wt% P 17R4 solutions for a clear view.

| **Table 5.3.5** SANS fitting results of the $Q$ = 3 $R$ = 0.01 $C_{lp}$ = 0.1 wt% DPPC/DHPC/DPPG | | |
|---|---|---|
| *PR-Disc* | in $D_2O$ | in $C_{polymer}$ = 0.1 wt% |
| Radius (Å) | 202 | >1000 |
| Polydispersity | 0.2 | -- |
| Thickness (Å) | 48.2±2 | 46.7±3 |

SANS have also been used to observe the morphology in the low-$C_{lp}$ low-$C_{polymer}$ solution. The disc form factor and uniform size can still be fitted in the low-$C_{lp}$ $D_2O$ solution. In the low-$C_{lp}$ low-$C_{polymer}$ mixture, the lack of low-q plateau is an indication for the larger aggregation. Even with different low-$C_{polymer}$ , this SANS data is consistent with the TEM and DLS results.

## 5.4 Discussion

Both the bicelle and P 17R4 are high complex self-assembly systems. It's been reported that the P 17R4 solutions had cluster networks and became cloudy at a high concentration $C_{polymer}$ > 9 wt%, which can be eliminated through filtration.[9] The clusters were considered as aggregations but not micelles. Even though we found there were large aggregations existing in the P 17R4 aqueous solutions below 9 wt%, the 200 nm membrane filtration should get rid of the big clusters and only leave unimers in the used P 17R4 solutions. The nanodiscs in bicelle system grow slowly in radius due to DHPC extraction from the rim upon dilution.[16]

From the Result section, we also found the mixing of bicelles in P 17R4 solutions caused the formation of vesicles in the mixed solutions of $C_{lp}$ = 0.5wt% and $C_{polymer}$ = 0.1wt%

and 0.5wt%. As the bicelles were found as nanodiscs before mixing with polymers, the vesicle formation could be treated as a disc-to-vesicle transition induced by P 17R4. Presumably, the PPG ends in each unimer can insert in the hydrophobic core of the lipid bilayer through hydrophobic effect and the PEG part stay between the discs in water by hydration interactions. Thus, under the hydrophobic and hydration effects, the P 17R4 unimers worked as linkers between the bicellar nanodiscs. Then the formed flexible bilayer folded up to minimize the surface tension. However, irregular morphological aggregates form in the lower lipid and polymer concentration instead of vesicle. Since the clear disc edge can still be seen in TEM, there may be a lack of linker polymers in solution.

The P 17R4 linkage behavior is similar to the "bridging effect" of reverse tri-block copolymers which happens in a high concentration and lead to gel networks formation.[17, 18] How did the "linkage" effect happen in such a low polymer concentration? We observed that the linkage of discs seemed mostly happened on the rim part of discs. In the bicelle system, free short-chain DHPC in solution keep exchanging with the rim DHPC in discs.[19] The exchange process could facilitate the PPG part go into the discs' rim part thus and promote the linkage. Furthermore, it may be also due to the melting phase of DHPC is easier to accommodate PPG ends than the crystalline DPPC/DPPG bilayers. A hypothesized cartoon of "linkage" is shown in Figure 5.3.8.

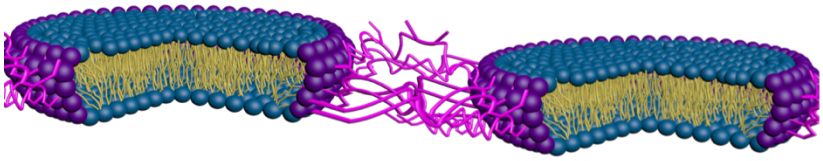

**Figure 5.3.8** 3-D hypothesized structure: “linkage” between bicellar discs by P 17R4

## 5.5 Conclusion

The PPG−PEG−PPG architecture of reverse Pluronic polymer enables it as the linker between lipid bicellar discs. This linkage provides a novel self-assembly method for producing small vesicles with non-toxic materials - phospholipids and Pluronic polymers. Future simulation works will be needed to decipher the Pluronic linkage mechanism.

## 5.6 References


1. D. Zhao, J. Feng, Q. Huo, N. Melosh, G. H. Fredrickson, B. F. Chmelka and G. D. Stucky, science **279** (5350), 548-552 (1998).
2. C. Wu, T. Liu, B. Chu, D. K. Schneider and V. Graziano, Macromolecules **30** (16), 4574-4583 (1997).
3. A. V. Kabanov, E. V. Batrakova and V. Y. Alakhov, Journal of controlled release **82** (2), 189-212 (2002).
4. D. E. Owens Iii and N. A. Peppas, International Journal of Pharmaceutics **307** (1), 93-102 (2006).
5. A. Pitto-Barry and N. P. Barry, Polymer Chemistry **5** (10), 3291-3297 (2014).
6. S. A. Maskarinec and K. Y. C. Lee, Langmuir **19** (5), 1809-1815 (2003).
7. M. A. Firestone, A. C. Wolf and S. Seifert, Biomacromolecules **4** (6), 1539-1549 (2003).
8. T. Demina, I. Grozdova, O. Krylova, A. Zhirnov, V. Istratov, H. Frey, H. Kautz and N. Melik-Nubarov, Biochemistry **44** (10), 4042-4054 (2005).
9. Z. Zhou and B. Chu, Macromolecules **27** (8), 2025-2033 (1994).
10. A. Huff, K. Patton, H. Odhner, D. T. Jacobs, B. C. Clover and S. C. Greer, Langmuir **27** (5), 1707-1712 (2011).
11. B. Naskar, S. Ghosh and S. P. Moulik, Langmuir **28** (18), 7134-7146 (2012).
12. B. C. Kumi, B. Hammouda and S. C. Greer, Journal of colloid and interface science **434**, 201-207 (2014).
13. S. Guiraud, D. Alimi‐Guez, L. van Wittenberghe, D. Scherman and A. Kichler, Macromolecular bioscience **11** (5), 590-594 (2011).
14. Q. Wang, L. Li and S. Jiang, Langmuir **21** (20), 9068-9075 (2005).
15. R. Soong, M. P. Nieh, E. Nicholson, J. Katsaras and P. M. MacDonald, Langmuir **26** (4), 2630-2638 (2010).
16. A. Hu, T.-H. Fan, J. Katsaras, Y. Xia, M. Li and M.-P. Nieh, Soft Matter **10** (28), 5055-5060 (2014).
17. M. Nguyen-Misra and W. L. Mattice, Macromolecules **28** (5), 1444-1457 (1995).
18. A. Cambón, E. Figueroa-Ochoa, M. Blanco, S. Barbosa, J. F. A. Soltero, P. Taboada and V. Mosquera, RSC Advances **4** (105), 60484-60496 (2014).
19. Y. Xia, M. Li, K. Charubin, Y. Liu, F. A. Heberle, J. Katsaras, B. Jing, Y. Zhu and M.-P. Nieh, Langmuir **31** (47), 12920-12928 (2015).

# Chapter 6 Summary and Future Work

## 6.1 Summary

Lipid bicelles are the most versatile model membrane system presently available. The application of bicelles beyond modeling membrane is in the booming age and has a great need to be developed. Chapter 1 briefly introduced the overview of bicelle structural studies and research objectives in this thesis. The major goal of this thesis is to develop the novel PEGylated discoidal and vesicular structures based on bicelle platforms and understand the self-assembly mechanisms. The knowledge could be applied in biomedical and other aspects. Chapter 2 introduced the major characterization techniques and principles for obtaining the structural information in bicelles.

In chapter 3, the structural variation of bicellar mixtures has been investigated under physiological relevant conditions. Bicellar nanodiscs and nano-vesicles have been produced with great features such as uniform size, easy preparation procedure, and highly stable in the dilute and salt conditions. One of the contributions to get these nanostructures is from the PEGylation of the bicelles. Chapter 4 focused on the PEGylation effects on the bicellar structures and thermal stability.

In chapter 5, the bicellar discs “linkage” has been achieved by the reverse Pluronics with PPG-PEG-PPG structure. Another disc-to-vesicle transition platform has been found, with the advantages of low-toxic materials and no high-temperature elevation. Both the features are useful for the scale-up production of phospholipid vesicles.

Overall, this thesis provides understanding of the bicellar self-assembled platforms and valuable insights to the rational design of bio-inspired materials. The works provided a base for the bicelles' potential applications in other fields after the initial popularity as model membrane since 1980s.

### 6.2 Future Aspects

Future studies should be focus on the applications of the discovered bicellar nanoparticles. The hydrophobic fluorescent dye can be encapsulated in bicellar discs and vesicles allowing *in vitro* cell study. The cellular toxicity of this NPs should be evaluated prior to in vivo study. The hydrophobic molecular encapsulation efficiency and the long-term stability should also be tested for the bicelles in biomedical usage. Furthermore, the optimal density and thickness PEG corona on the surface of bicellar nanoparticles can be tested by the length of *in vivo* blood circulation time.

The magic of "linkage" between bicellar discs by reverse Pluronics will be a very fascinating topic to be deciphered. The interactions can be analyzed from the hydrophobic and hydration effects, electrostatic repulsions and van der Waal attractions. Thus, by varying the lengths of the hydrophobic and hydrophilic subunits in the reverse Pluronics and the surface charge amount in bicellar discs should affect the linkage kinetics and structures. Moreover, superstructures such as "disc stacking" may be

obtained through the “linkage” behavior, which can provide a variety of available strategies for incorporation of additional functionalities into a stack structure.

It’s expected that the studies in this thesis can provide the basis for the rejuvenation of the old-fashion model membrane “bicelles” in different fields of applications and fundamental studies.